ABSTRACT

DESIGN, FABRICATION AND TESTING OF A FIBER OPTIC STRESS/STRAIN SENSOR FOR SOFT STRETCHABLE MATERIALS USING POLARIZATION IMAGING TECHNIQUE

by
Jianjun Zheng

The polarization imaging technique has been used to obtain high quality surface images of turbid media. This technique can be slightly modified and used for noninvasive sensing of strain and stress in soft stretchable materials, such as latex and human tissues. Previously this sensing method was developed with free space bulk optics. In this study, a fiber optic based system is developed to investigate the potential application of this technology on the strain/stress as well as surface roughness measurements of stretchable materials. In this system, polarizers are simply attached to the fiber ends to form a polarizing three-fiber probe. Furthermore, no collimating lens is employed thereby increasing the cost effectiveness and simplicity of the probe fabrication.

Two types of surface conditions are considered: 1) flat rough surface, 2) curved rough surface. The sinusoidal surface roughness model is employed for both kinds of surfaces for theoretical analysis and simulations. A theory is developed based on prior works to determine the behavior of the normalized reflectivity for different surface roughness parameters when the surface is under the applied strain. A variety of fiber probes with different configurations are fabricated and employed to measure the normalized reflectivity in the experiments. Polyvinyl samples with rough surfaces are continuously stretched to yield the necessary strains. The experimental results are discussed and compared with corresponding analytical predictions. Both experimental

and simulation results suggest that for flat surface conditions, the fiber optic system can replace the bulk optic system and yet maintain good performance of the later. It is further shown that the performance of the fiber optic system on flat surface conditions is insensitive to the configuration of the fiber probe. However, for curved surface conditions, the performance of the fiber optic system shows a complicated dependence on the sensing circumstances, indicating that a collimating fiber lens in front of the incident fiber would be necessary to make the system to work properly under most surface conditions.

DESIGN, FABRICATION AND TESTING OF A FIBER OPTIC STRESS/STRAIN SENSOR FOR SOFT STRETCHABLE MATERIALS USING POLARIZATION IMAGING TECHNIQUE

by
Jianjun Zheng

A Dissertation
Submitted to the Faculty of
New Jersey Institute of Technology and
Rutgers, The State University of New Jersey-Newark
in Partial Fulfillment of the Requirements for the Degree of
Doctor of Philosophy in Applied Physics

Federated Physics Department

August 2007

APPROVAL PAGE

DESIGN, FABRICATION AND TESTING OF A FIBER OPTIC STRESS/STRAIN SENSOR FOR SOFT STRETCHABLE MATERIALS USING POLARIZATION IMAGING TECHNIQUE

Jianjun Zheng

5/21/07

Dr. John F. Federici, Dissertation Advisor — Date
Professor of Physics, NJIT

5/16/07

Dr. Robert B. Barat, Committee Member — Date
Professor of Chemical Engineering, NJIT

5/16/07

Dr. Nuggehalli M. Ravindra, Committee Member — Date
Professor of Physics, NJIT

5/16/07

Dr. Gordon A. Thomas, Committee Member — Date
Professor of Physics and Biomedical Engineering, NJIT

5/16/07

Dr. Trevor A. Tyson, Committee Member — Date
Professor of Physics, NJIT

5/16/07

Dr. Hee Chuan Lim, Committee Member — Date
Research Professor of Physics, NJIT

BIOGRAPHICAL SKETCH

Author: Jianjun Zheng

Degree: Doctor of Philosophy

Date: August, 2007

Education:

- Doctor of Philosophy in Applied Physics,
  New Jersey Institute of Technology, Newark, NJ, 2007
- Master of Science in Electrical Engineering,
  Tufts University, Medford, MA, 2000
- Bachelor of Science in Applied Physics,
  Wuhan University, Wuhan, P. R. China, 1994

Major: Applied Physics

Publications:

Y. Lu, J. Zheng, Y. Lu, and N. Ming, "Frequency tuning of optical parametric generator in periodically poled optical superlattice LiNbO3 by EO effect," *Appl. Phys. Let.*. **74**, 123, 1999.

Y. Lu, J. Zheng, M. C. Golomb, F. L. Wang, H. Jiang, J. Zhao, "In-plane electro-optical anisotropy of (1-x)PMN-xPT thin films grown on (100)-cut LaAlO3," *Appl. Phys. Lett.* **74**, 3764, 1999.

J. Zheng, Y. Lu, X. Chen, M. C. Golomb, and J. Zhao, "Photoluminescence in erbium-doped PMN-PT thin films," *Appl. Phys. Lett.* **75**, 3470, 1999.

F. Wang, K. K. Li, V. Fuflyigin, M.Tabasky, P. Pondillo, J. Zheng, H. Jiang, "Optical phase modulators and Spatial Light Modulators based on Thin Ferroelectric Interferometers (TFIs)," SPIE's *Symposium on Integrated Optoelectronics* Jan 23-28, 2000, San Jose, CA.

K. Guo, H. Ou, T. Grycewicz, A. Joshi, X. Wang, G. A. Thomas, H. Wang, R. Greene, D. Misra, Z. Liu, J. Zheng, X. Wang, B. Li, Z. Xiao, N. A. Ciampa, J. Opyrchal, H. Opyrchal, and K. K. Chin, "1D InGaAs Lock-in FPA," Proceedings of SPIE, **5406**, pp.64-72, *Infrared Technology and Applications* XXX , 2004.

J. Zheng, K. K. Chin, J. Madey, E. Sczarmes, "Simulations of the Newark FIR FEL Operation," Proceedings of *26th International Free Electron Laser Conference & 11th FEL Users Workshop*, 550, 2004. *http://cern.ch/AccelConf/f04/papers/TUPOS59/TUPOS59.PDF*

J. Zheng, H. C. Lim, and J. F. Federici, "Fiber optic stress/strain sensor for soft materials using polarized light reflection technique," (To be submitted to *Appl. Opt.*).

J. Zheng, H. C. Lim, and J. F. Federici, "A Fiber optic sensor design for the measurement of the Young's modulus of blood vessel tissues," (To be submitted to *Appl. Opt.*).

A hydrogen atom is as complicated as a human body

ACKNOWLEDGMENT

I would like to thank my advisor Dr. John F. Federici who volunteered to work as my advisor two and half years ago and brought my research back to the right track, which leads to the completion of this dissertation. Every discussion with Dr. Federici was inspiring and encouraged me to pursuit deeper understanding about the research challenges I encountered. Particularly, I appreciate his time and efforts that went into the very intensive reviews of this dissertation.

I would also like to thank Dr. Hee Chuan Lim, a committee member, a friend and mentor of mine. Dr. Lim was always kind and generous to help me in finding the necessary equipment, setting up the experiments, and shooting troubles. Particularly, Dr. Lim shared with me many soft-wares and programs developed during his own doctoral program.

I also wish to acknowledge the support from Dr. Nuggehalli M. Ravindra, a committee member, who gave me constructive advices and paid close attention to my progress toward the completion of my study in NJIT. Special thanks go to the rest of committee members, Dr. Gordon A. Thomas, Dr. Trevor A. Tyson and Dr. Robert B. Barat who took time and efforts to serve the committee, and gave valuable suggestions and kind criticisms in the proposal of this dissertation.

Finally, I give my thanks to my family, my former university professors and friends who encouraged and supported me when I was not clear what a doctoral degree could do to my life.

TABLE OF CONTENTS

Chapter	Page
1 INTROUCTION	1
1.1 Background	1
1.2 Important Application Findings	2
1.2.1 Skin Stretch Measurement and Stress Estimation	2
1.2.2 Endoscopy of Body Cavity and Blood Vessel tissues	3
1.3 Tissue Optical Properties, Specular and Diffusive Reflections	6
1.3.1 Tissue Optical Properties	7
1.3.2 Specular and Diffusive Reflections	9
1.4 Light Reflectance Technique for Measuring Tissue Stretch	11
1.4.1 The Principles of the Stress/Strain Sensor for Soft Tissue	11
1.4.2 Experiment on Bulk Optic System	12
2 THEORY AND MODELING	16
2.1 Surface Roughness Modeling	16
2.2 Free Space Bulk Optics Analysis	17
2.2.1 Review of Prior Analysis	17
2.2.2 First Order Approximation	21
2.2.3 Numerical Test of the Approximation	24
2.2.4 Linearization of the Result	27
2.2.5 Discussion and Summary	28
2.3 Analysis on Fiber Optics Configuration	29
2.3.1 Small Divergence and Acceptance Angle Configuration	30

TABLE OF CONTENTS
(Continued)

Chapter	Page
2.3.2 Divergent Beam Far Field Configuration	31
2.3.3 Divergent Beam Near Field Configuration	33
2.4 Analysis on Curved Surfaces	38
2.5 Numerical Simulations by Ray Tracing	39
2.6 Young's Modulus Extraction From the Reflectivity Measurement	42
3 EXPERIMENTS	43
3.1 Bulk Optic Experiment on Latex and Polyvinyl Materials	43
3.2 Experiments on Fiber Optic Components	49
3.2.1 Fabrication of the Polarizing Fiber Probe	49
3.2.2 Experiments on Flat Surface with Fiber Optic Components	56
3.2.3 Fiber Optic Components with Curved Surfaces	57
4 DATA ANALYSIS AND SYSTEM OPTIMIZATION	60
4.1 Flat Surface Experimental and Simulation Results	60
4.1.1 Experimental Data	61
4.1.2 Data Summation	64
4.1.3 Simulation Comparison	66
4.1.4 Discussion	68
4.1.5 Summary	69
4.2 Curved Surface Results	70
4.2.1 Description on Several Experimental Parameters	70
4.2.2 Material Elasticity Investigation	71

TABLE OF CONTENTS
(Continued)

Chapter **Page**

4.2.3 Experimental Results..... 73

4.2.4 Discussion..... 79

4.2.5 Summary..... 82

4.3 Optimization of the Fiber Probe Configuration..... 83

5 DISCUSSION..... 84

5.1 Validity of the Surface Roughness Modeling..... 84

5.2 Performance Compared With Bulk Optics System..... 85

5.3 Blood Vessel Elasticity Measurement Application..... 88

5.4 Improvement on the Design of the Fiber Probe..... 92

6 CONCLUSION AND SUGGESTIONS..... 95

6.1 Conclusion..... 95

6.1.1 Flat Surface Summary..... 96

6.1.2 Curved Surface Summary..... 97

6.2 Future Research Suggestions..... 98

REFERENCES..... 99

LIST OF TABLES

Table		Page
2.1	Percentage Difference of Surface Path Length between Rigorous Values and Approximated Values	24
2.2	Slope and Linear Range of Strain Determinations	28
3.1	Fiber Probe Configurations	55
4.1	Slope and Linear Correlation Coefficient Extracted for Probe 2	64
4.2	Slopes and Linear Correlation Coefficients for All Probes at Different Probing Distances	64
4.3	Numerical Result of the Slope and Linear Correlation Coefficient of Probe 2 for Different Probing Distances	66
4.4	Comparison between Slopes Obtained from Simulations and Experiments	67
5.1	Comparison between Surface Diameter and Fiber Probe Configuration	91

LIST OF FIGURES

Figure		Page
1.1	A typical endoscope employing flexible illumination and observation optics.....	4
1.2	Images obtained from different polarization components and their resolution comparing. (a) image obtained from the parallel polarization component of the reflected light; (b) image obtained from the perpendicular polarization component; (c)image obtained by subtracting the perpendicular component from the parallel component.	11
1.3	Experimental schematic in prior works: Argon laser laser light is reflected from the guinea pig skin sample. P1 and P2 are polarizing filters for the incident and the reflected light, respectively.	13
1.4	Solid curves are for four guinea pig skin samples, the dashed curve represents the average of the four plots and is shitted to the lower region of the figure for clarity.	14
1.5	Normalized reflectivity for polyvinyl chloride sample with initial length of 45mm and maximum stretch of 19mm. Solid line shows the linear fit of the data.	14
2.1	Surface roughness global and local views, the global and local definition of angles of incidence and reflection, orientation of the detector to the flat rough surface.	17
2.2	The reflected light is confined within an angle range $\Delta\Phi=2Ag$ set by the surface parameters A and g for small roughness cases.....	19
2.3	Initial surface roughness $A_0 g_0$=0.5, linearity between the normalized reflectivity and strain is valid for strain less than 3%.....	25
2.4	With initial roughness $A_0 g_0$=1, the linearity is well maintained until the strain excesses 10%, but the slope of the linearity decreases compared with the previous case where $A_0 g_0$= 0.5.....	26
2.5	Normalized reflectivity for surface initial roughness $A_0 g_0$=2, 3, 4, 5 as marked in the plot. As the roughness increases, the linear range of the relationship between the normalized reflectivity and the strain increases, but the slope of the linearity decreases.....	27

LIST OF FIGURES
(Continued)

Figure		Page
2.6	Three operation regimes are shown. For most applications stretches are within 15%, and linearity is expected to hold during the stretch for rough surface cases.....	29
2.7	Fiber incident and detection schematic. R is the fiber to surface distance, D is the fiber core diameter, θ_0 is the incident divergence angle, $\Delta\Phi$ is the light spread angle after reflection.....	30
2.8	Far field configuration. The central light rays that form the stripe in the center of the spot on the sample contribute most to the detected power, while the contribution from peripheral rays can be neglected.....	32
2.9	Near field configuration. The illumination spot on the sample is divided into two regions: The paraxial region I and the periphery region II.....	34
2.10	Cylindrical surface with sinusoidal roughness model. ρ is the radius of the cylinder, and the stretch is applied along the transverse direction. The incident fiber and the receiving fiber are kept parallel and both are in the normal direction of the surface.....	39
2.11	Ray tracing program flow chart.....	41
3.1	Schematic experiemental setup with bulk optic components. In the xperiements, the polarization orientation of the incident light is perpendiculer to the direction of the stretch and parallel to the sample surface (or simply called TE incident mode). The incident angle is about 57 degrees, corresponding to the Brewster angle[6] of the material.....	44
3.2	Reflectivity as a function of the strain ($\frac{\Delta L}{L_0}$) for the polyvinyl sample.....	45
3.3	Normalized reflectivity vs. stretch (a) and stress vs. stretch (b) for the 50mm and 78mm long samples (error bar: (a) ±5%; (b) 0.2mv).....	47
3.4	Stress as a function of strain (A), Normalized reflectivity as a function of strain (B). The slopes of the plots for the two samples are close.....	48
3.5	Positioning of the fiber probe for oblique incidence. Once the fiber probe has been fabricated, the probe to sample distance in an application must be fixed, hence lacks flexibility of positioning.....	50

LIST OF FIGURES
(Continued)

Figure		Page
3.6	Two-fiber configuration of the polarizing fiber probe.....	50
3.7	Three-fiber configuration of the fiber probe.....	51
3.8	Fiber array is sandwiched between two glass slides.....	53
3.9	Polarizing filters with orthogonal polarization orientations are glued to the robe ends. The central fiber is the incident fiber, and together with the parallel receiving fiber is covered by the same polarizing plate.....	54
3.10	A fully fabricated sensor with fiber pigtails. The dimension of the probe head is about 2×3×10mm.....	55
3.11	Experimental setup for flat rough surfaces.....	56
3.12	Curved surface cases: (a) schematic of application, (b) experimental setup...	58
4.1	Reflectivity measured using Probe 2 at 1mm probe to sample distance.....	61
4.2	At 2mm probe to sample distance, results obtained with Probe 2.....	62
4.3	Reflectivity measured at probing distance 3mm with Probe 2.....	63
4.4	Slope and linear correlation coefficient extracted from the linear fitting between the normalized reflectivity and strain as a function of the probing distance.....	65
4.5	Simulation result of Probe 2 at 3mm probe-to-sample distance with maximum strain of 15%.....	67
4.6	Simulation and experimental slopes vs. Probe # for different probing distances.....	68
4.7	Surface swells after air pressure is applied, R is the radius of the sphere, D is the aperture of the opening, and h is the height of the partial sphere measured from the base of the mounting.....	70
4.8	Elasticity of the sample material, the linear relation between the strain S and surface tension T (N/m) or PR is maintained for strain less than 15%.....	72

LIST OF FIGURES
(Continued)

Figure		Page
4.9	Normalized reflectivity vs. strain measured with Probe 2 (200/220μm fiber) at 1mm probing distance. Read line is the linear regression line for the experiment data. The over all data fitting shows a slope of 2.67. With in the linear range, the linear fitting gives a slope about 3.4.....	74
4.10	Result obtained with Probe 2 at 2mm probing distance, red line is the linear fit of the measured curve, the shorter line with slope 2.29 is the linear fit for strain less than 15%.....	75
4.11	The behavior of normalized reflectivity under strain for 3mm, 4mm, and 5mm probing distance with Probe 2. The normalized reflectivity first decrease as the surface expands, after the surface strain exceeds about 7%, the normalized reflectivity starts to increase.....	76
4.12	For small probing distance, the curved surface can be treated as flat one with good approximation; for larger probing distance, the approximation is not valid.....	77
4.13	Curvature radius vs. strain and its derivative, -dR/dS is the absolute value of the curvature radius changing rate with respect to the strain. It is obvious that with small strain at the beginning of the surface expansion, the rate at which the radius changes is the largest.....	78
4.14	The behavior of the normalized reflectivity under strain with Probe 3 (485/500μm fibers) at 1mm~5mm probing distances.....	79
4.15	Simulation result with fixed 30mm radius cylinder surface using probe 2 at 3mm probing distance.....	81
4.16	When the probing distance (1mm) is comparable to the curvature radius (1mm) of the surface, for Probe 2 there is no evidence showing that linear relationship between the normalized reflectivity and the strain maintains for a cylindrical surface.....	81
5.1	A fiber optic result obtained with Probe 2 at 3mm probing distance compared with result obtained from bulk optic system.....	86
5.2	Fiber optic probing of the blood vessel wall for the estimation of elasticity of the vessel tissue. A miniaturized pressure sensor can be attached to the fiber probe.....	90

LIST OF FIGURES
(Continued)

Figure		Page
5.3	End view and top view of the proposed configuration of the fiber probe. A GRIN lens is sandwiched between the incident fiber end and the polarizing plate.....	92
5.4	The configuration of the single-fiber probe using PM fibers.....	93

CHAPTER 1

INTRODUCTION

1.1 Background

In recent decades, biomedical engineering using optical methods has drawn remarkable interest. The academic area called biophotonics is rapidly developing due to the increased diagnostic and therapeutic applications powered by the laser and photonic technologies. Research on medical instruments developed from fiber optic technologies is very active and shows considerable potential. Biomedical imaging methods from the X-ray, Magnetic Resonance Imaging (MRI), Computed Tomography (CT) to endoscopy have constantly evolved. They have been some of the well known imaging technologies. Recently, R. R. Alfano et al. have used a polarized light illumination and detection method, known as polarization imaging, to obtain the surface image as well as structures beneath the surface of a turbid medium[1]. Several other research groups are studying fiber optic confocal reflectance microscopy[2–5]. J. F. Federici's group at New Jersey Institute of Technology (NJIT) has demonstrated that a stretch/stress sensor for a soft tissue could be developed from a modification of two–dimensional polarization imaging technique[6,7]. So far to our knowledge no other research group has combined the fiber optic technology and the polarization imaging technique to develop the sensor for measuring the stress/strain and the elasticity of soft stretchable materials, such as plastic, polyvinyl chloride, human skin, blood vessel tissues, and cavity walls inside human bodies. In this dissertation, a prototype of a fiber optic based noninvasive stress/strain sensor for soft

stretchable materials using polarization imaging technique is proposed and laboratory developed.

1.2 Important Application Findings

Two categories of potential applications of the sensor are envisioned in biomedical instrumentation areas: skin stretch measurement and stress estimation, and endoscopy of body cavity and blood vessel tissues.

1.2.1 Skin Stretch Measurement and Stress Estimation

Light reflection techniques have been used to study the properties of human skin non-invasively. The optical properties of the skin are determined by its physical structure and chemical composition. Research employing the light reflection and transmission methods is mainly directed to the studies of the biochemistry and biophysical phenomena in human tissues[8]. Recently, the importance of the real-time measurement of the stretching of skin and the estimation of stress/strain in skin for diagnostic and therapeutic applications in plastic surgery has been recognized[9–12]. The noninvasive nature of the light reflection method in measuring the excessive tensile stresses in the skin is attractive. Real time monitoring of the tensile stresses and their distribution at the vicinity of the wound is desired. It has been well understood that the mechanical stresses in the skin interact with the patterns of cell proliferation and cell migration during the suturing of the wounds, and the blood flow underneath the skin is also affected by the stress distribution of the skin[13–16]. High tension across the recovering area of the wound could produce a stretched hyper tropic scar, thus the scale of the achievements of the plastic surgery could be reduced[6,7,10]. In extreme cases where the consequence of the excessive tension is too

severe, it could lead to a complete failure of the plastic treatment. Therefore, it is worthwhile to determine deformations and to predict stresses for a given pattern of wound suturing[6,7], such that medical interventions may be applied based on this information.

So far, biomechanical models employing finite element analysis have been used to assess the stress distribution in the skin. Based on analysis, preferred suturing patterns and wound geometries can be determined[17]. The proposed polarization imaging method uses changes in the diffusive reflection properties of skin due to mechanical deformations to determine the tissue stresses non-invasively. A fiber optics delivery-detection system would allow the surgeons to determine the amount of strain of the skin in real time using common endoscopic probes. And the fiber optic system is more reliable than a bulk-optic system, because no alignment of discrete optical components is needed, and it is not sensitive to the disturbance of the environments, thus a turn-key operation is expected.

1.2.2 Endoscopy of Body Cavity and Blood Vessel Tissues

Due to the usage of the screening programs to detect precancerous lesions, the incidences and mortality rate of many tumors have been reduced[18]. The current method for the detection of suspicious cancerous tissues inside human body requires the removal and *in vitro* analysis of tissue sections[19]. Fiber optic endoscopy (Figure 1.1) to obtain the information about the cellular and nuclear morphologic features of these sections non-invasively, *in vivo* and in real time has the potential of decreasing the screening time and costs. This technology can be improved by grafting the polarization imaging features to the conventional imaging system. *In vitro* studies have shown that the confocal reflectance microscopy can provide the morphological information non-invasively and in

real time[19,20]. *In vivo* confocal reflectance microscopy has been applied to the organs including the eyes, the skin, and the lip[21-23] due to easy accessibility. Many sites of interest such as organ cavities, blood vessels, and gland tracks require miniaturized fiber optic features. Configurations of fiber based endoscopies for confocal imaging have been made by several research groups[24-27]. *In vivo* imaging using confocal reflectance endoscopy suffers from the low signal and contrast levels; the fluorescence confocal endoscopy requires fluorescent dyes which must be nontoxic and capable of penetrating deep into the tissue[19]. These systems are bulky, complicated and expensive to build. The fiber optic system takes the advantages of polarization imaging technique and miniaturized fiber based optics. Improved signal and contrast levels have been demonstrated for the imaging of a surface and the structures beneath the surface of a scattering medium in the retroreflection geometry[1]

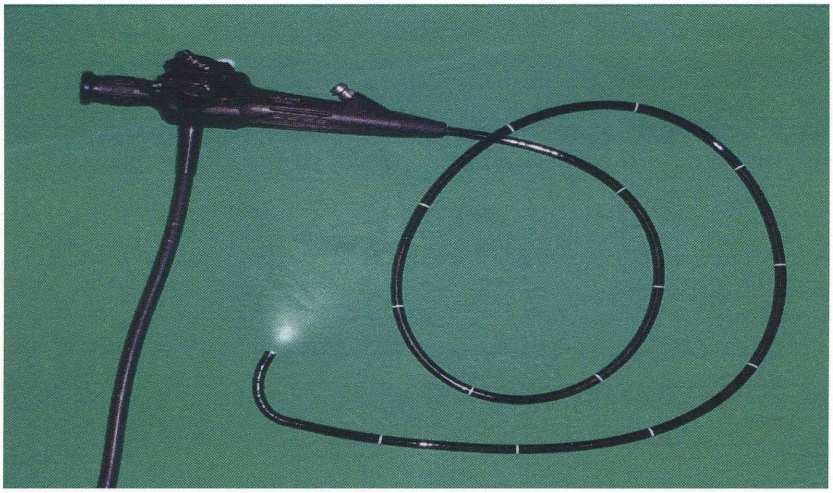

Figure 1.1 A typical endoscope employing flexible illumination and observation optics. (Source: http://en.wikipedia.org/wiki/Endoscopy#Components)

Cardiovascular disease is another category of health problem threatening people of all ages. Hypertension and blood vessel tumors (aneurysms) are widely diagnosed

among common people. Moreover, the research on the pathological development of these diseases is still very active. *In vivo*, real time visualization of the diseased parts of the vessel (such as deformation of the internal wall surface of the artery due to building up of fatty materials or the growth of tumors) employing a fiber optic polarization imaging system and technique has the potential to provide better understanding of the initiative and development of these diseases. Therapeutic treatments could be delivered via the same system.

Aneurysms are the abnormal local enlargements of the arteries. Cerebral aneurysms and abdominal aortic aneurysms are two major types of aneurysms that threaten human lives significantly. The mortality rate of 80% to 90% is estimated for the ruptures of these aneurysms, and the rupture of abdominal aortic aneurysm alone is ranked the 13th of death causes in the United States[8,29,30]. Study has been undertaken to investigate the relationship between the strength of the walls of cerebral aneurysms and the growth/rupture of the aneurysms[31]. Research on the common vessels, abdominal aortic aneurysms, and their wall biomechanical properties has drawn close attention in past decades[32-36]. The *in vitro* measurements of the mechanical properties of the normal vessel tissues and the aneurysm walls have been done mainly by applying external loads on the excised tissues[30-32]. *In vivo* noninvasive measurement methods are limited to two major techniques: ultrasound and computed tomography[37-39]. Tissue doppler imaging (TDI) of carotid plaque wall motion using a Philips HDI5000 scanner and L 12-5 probe was reported several years ago[40]. Although these *in vivo* techniques can provide basic means of access to the sites of interest, the accuracy of the measurements is not satisfying, and the operation of these systems is complicated, requiring advanced analysis skills.

Feferici's research group in NJIT has successfully shown that the polarization imaging technique can be modified to estimate the skin stress/stretch or to measure the elasticity of the soft tissues[6,7]. This polarizing optic technique combined with fiber optic features has the potential to obtain higher accuracy on the measurements of the body cavity and blood vessel mechanical properties *in vivo* and non-invasively. Applying the fiber optic polarized light reflection technique to the blood vessels provides an alternative method to study the mechanical properties of the aneurysms as well as the normal vessel tissues. This technique would use the difference between the systolic and the diastolic blood pressure as the mechanical load on the vessel walls, while the reflectivity change from the vessel walls due to the surface roughness change (caused by pressure change) is detected by the fiber system. Theoretical analysis would link the reflectivity change to the strain/stress in the vessel tissues. Hence, the mechanical properties such as Young's modulus of the vessel wall tissue can be extracted. In the clinics, it is important to monitor the elasticity of the aneurysm wall of the patient in a real time, low cost, and convenient way. The fiber system is flexible, easy to operate, and can be readily attached to the catheters in routine clinical treatments. The non-invasive nature of this technique presents significant application potential in the cardiovascular disease research.

1.3 Tissue Optical Properties, Specular and Diffusive Reflections

In this dissertation, human tissues (skin or blood vessels) are assumed to be the target materials in the application, hence are treated as the examples of the highly scattering, soft stretchable materials, although the application of the fiber optic sensor is not limited to these tissue materials. Since the optical properties of the turbid medium (highly

scattering material) determine the methods of improvement in the imaging techniques, it is necessary to understand the basic tissue optics before the discussion of the application.

The interaction between laser radiation and tissue depends on many parameters including the laser wavelength, power, radiation duration, energy dose, and the characteristics of tissue under study. The optical properties, such as index of refraction, absorption, and other coefficients depend upon the condition of the tissue, thus are not constants. Temperature, dehydration or hydration, nutrients concentration, physical or mechanical condition can dynamically alter the reflection, absorption and scattering properties of the tissue[7,8]. By nature, body tissue is a complex medium, light reflection from the tissue is diffusive and technically complicated[6]. The mathematical formulations of the light behavior in the tissue starting from Maxwell equations yield limited useful information[41,42]. The empirical approach employing basic optic principles can produce solutions that reasonably describe the optical effects at the surface and inside of the tissue under laser radiation[42,43].

1.3.1 Tissue Optical Properties

It is worthwhile to point out that the propagation of photons in the tissue can be approximately described by two parameters, namely the absorption coefficient μ_a and the scattering coefficient μ_s. The absorption in tissue originates from the presence of natural chromophores, including the hemepigment of hemoglobin, myoglobin and bilirubin, the cytochrome pigment, and added chromophores introduced by dyes during photodynamic therapy. The scattering in tissues is caused by discontinuities in refractive index on the microscopic level, such as the aqueous-lipid membrane interfaces surrounding the cell[41]. These parameters are wavelength sensitive.

In the commonly used spectrum region from about 600nm to 1300nm, the value of μ_a ranges from 0.01 to 1mm^{-1}, and μ_s varies from 10 to 100mm^{-1}. The total attenuation coefficient μ_t is the sum of μ_a and μ_s, and the mean free path ($=1/\mu_t$) is the average distance traveled by a photon before a scattering or absorption event occurs. It is straight forward to derive that the mean free path is from 10μm to 100μm approximately given the values of μ_a and μ_s above. Most interactions are scattering rather than absorption events, and the scattering is highly forward-directed so that a photon can penetrate the tissue deeply despite the multiple scattering events. Anisotropy coefficient g is introduced to characterize the directivity of the scattering by averaging $<\cos\theta>$ over the entire solid angle of scattering, where θ is scattering angle of an individual event. In the spectral range from 300nm to 1300nm, the g value is typically between 0.8 and 0.95[42-47]. From the similarity principle[44, 48], g and μ_s can be combined to form the reduced scattering coefficient $\mu_s'=(1-g)\mu_s$, which is also know as the transport scattering coefficient or transport cross section. In most applications μ_s' gives enough information without knowing g and μ_s values.

So far, μ_a and μ_s' values are major parameters in the treatment of propagation of laser light in tissues. Based on diffusion theory, $\delta=1/\mu_{eff}$ is the effective penetration depth, where $\mu_{eff}=(3\mu_a(\mu_a+\mu_s))^{-1/2}$ is the corresponding effective attenuation coefficient[42]. Between the wavelength of 600nm and 1300nm, the g value is almost wavelength independent and μ_s falls slowly as the wavelength increases[46]. The absorption coefficient μ_a varies remarkably in the visible spectral range[42]. It is also observed that the blood content and oxygenation status, and the concentration of other pigments alter the value of μ_a. The penetration depth δ increases rapidly from 600nm to 700nm due to decreasing

hemoglobin absorption, and is almost constant above 700nm. At about 960nm there is a small dip due to the absorption of water[49,50]. At a wavelength of 630nm, the index of refraction has been measured to be in the range of 1.38-1.41, and varies with the tissue water content.

1.3.2 Specular and Diffusive Reflections

After the brief review of the tissue optical properties, this section discusses the light reflectance from the skin. It is well known that the refractive index mismatch at an interface of two materials gives rise to Fresnel reflection, which is $R_{sp}=(1-n)^2/(1+n)^2$ for normal incidence. For the skin refractive index n=1.38, $R_{sp}=0.025$. For oblique incidences, the general Fresnel equations can be used:

$$R_s = \left|\frac{\cos\theta - n\cos\phi}{\cos\theta + n\cos\phi}\right|^2 = \left|\frac{\cos\theta - \sqrt{n^2 - \sin^2\theta}}{\cos\theta + \sqrt{n^2 - \sin^2\theta}}\right|^2$$

$$R_p = \left|\frac{\cos\phi - n\cos\theta}{\cos\phi + n\cos\theta}\right|^2 = \left|\frac{-n^2\cos\theta + \sqrt{n^2 - \sin^2\theta}}{n^2\cos\theta + \sqrt{n^2 - \sin^2\theta}}\right|^2$$

where θ and ϕ are the incident and refraction angles, respectively.

The photons that are specularly reflected from the air-skin interface provide the information about the skin refractive index and surface roughness. Studies show that surface roughness generally reduces the specular reflectance from the surface[51,52]. A part of photons that are transmitted through the interface may be scattered and absorbed by the skin tissue as discussed in previous sections. After multiple scattering events, a portion of the transmitted photons reemerge through the air-skin interface as diffusively reflected light. The intensity and the angular distribution of diffusive reflection are determined by the transmission and the scattering properties of the skin tissue, as well as

by the polarization state of the incident light[53,54]. Another part of transmitted photons are also specularly reflected by interfaces caused by the skin internal structures[6,56-58]. Photons that are specularly reflected from the interfaces between layers of skin tissue and the air-skin boundary preserve their polarization states and are called ballistic photons.

The photons being scattered in the skin tissue change their polarization states, such that after a sufficient number of scattering events these photons totally lose their initial polarization states, consequently, they can be treated as random or unpolarized after they reemerge through the air-skin interface, this portion of photons are called diffusive photons in comparing with the ballistic photons.

Thus the ballistic photons carry the structural information for both air-skin interfaces and internal layers of the skin, while the diffusive photons contribute to background noise if only the surface morphology and inner regular structures are of interest. Since the diffusively reflected photons are unpolarized, the two orthogonal polarization components of the diffusive light are equal to each other[6,7]. In the imaging experiments with a polarized laser beam as illuminating source, higher resolution images can obtained by subtracting the power of orthogonal component (with respect to the incident polarization direction) from that of the parallel component measured via the polarization imaging optics. Figure 1.2 (c) shows the improvement of picture resolution of a human palm obtained from this imaging technique[1].

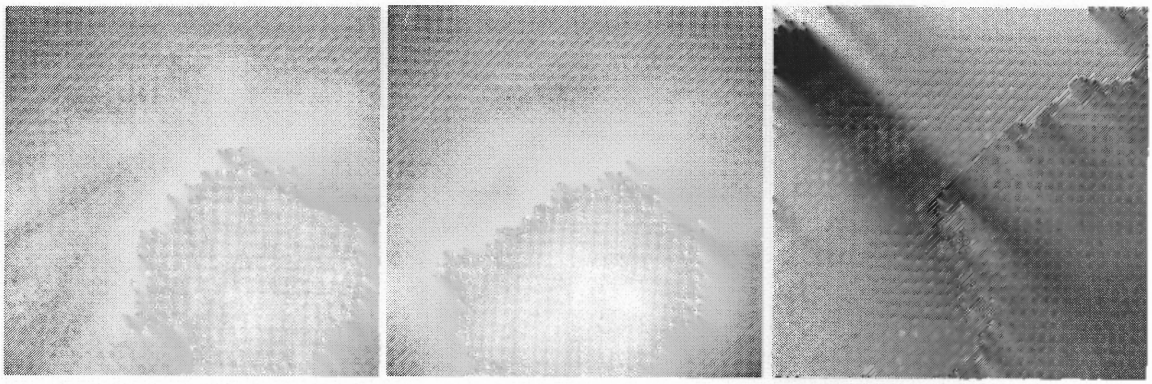

(a) (b) (c)

Figure 1.2 Images obtained from different polarization components and their resolution comparing. (a) a human palm image obtained from the parallel polarization component of the reflected light; (b) image obtained from the perpendicular polarization component; (c)image obtained by subtracting the perpendicular component from the parallel component.
(Source: R. R. Alfano et al.)

1.4 Light Reflectance Techniques for Measuring Tissue Stretch

With the help of the pulse-compressed 1064mn laser pulses from the Na:YAG laser, research has shown that the temporal profiles of the parallel and perpendicular polarization components of a polarized light pulse back scattered from a soft tissue are different[1]. The images of the palm of a human hand under 850nm linearly polarized laser illumination have been investigated. It has been demonstrated that much higher resolution of the palm image can be formed after subtraction of the perpendicular polarization image component from the parallel polarization image component.

1.4.1 The Principles of the Stress/strain Sensor for Soft Tissue

The NJIT's research group has introduced a new technique based on a modification of the polarization imaging method to measure skin stretch by using the small changes that take place in the diffusive and specular reflectivity of the skin due to stresses. When linearly polarized light is incident on the tissue sample, the ballistic photons reflected back from

the sample maintain the polarization status, and constitute the parallel polarization component of the reflected light; while the diffusive photons lose their initial polarization status, thus parallel and perpendicular polarization states are equally present in the diffusively reflected light. The measured parallel component of the reflected light also contains half of the diffusively reflected power, which is represented by the measured power of the perpendicular component. Therefore, removal of that amount of power from the parallel component will yield the pure optical signal due to ballistic photons, which carry the information of surface morphology. Since the stress changes the structure of the tissue and its surface topography, the specular and diffusive reflectivity will change accordingly. Based on this knowledge and the modeling of surface topography, relationship between the stress/strain and reflectivity can be obtained[6,7,55].

1.4.2 Experiment on Bulk Optic System

In prior experiments[6,7](Figure 1.3), a linearly polarized argon-ion laser beam with wavelength λ=488nm and power<1mW was used. Four guinea pig skin samples were prepared and kept wet with saline solution during the experiments[6,7]. A large area Si photo detector was oriented in the specular reflection direction behind the light collecting lens. A mechanical chopper and a lock-in amplifier were employed. Intensities of the parallel and perpendicular polarization components of the reflected light were measured. The incident angle was set at 57°. The light collection lens has a focal length of 35mm, with solid angle of collection about 2.5×10^{-2} sr and the spot size of the incident beam is about 2mm. The maximum stretch for the samples was about 17%. A Labview program was used to collect the data.

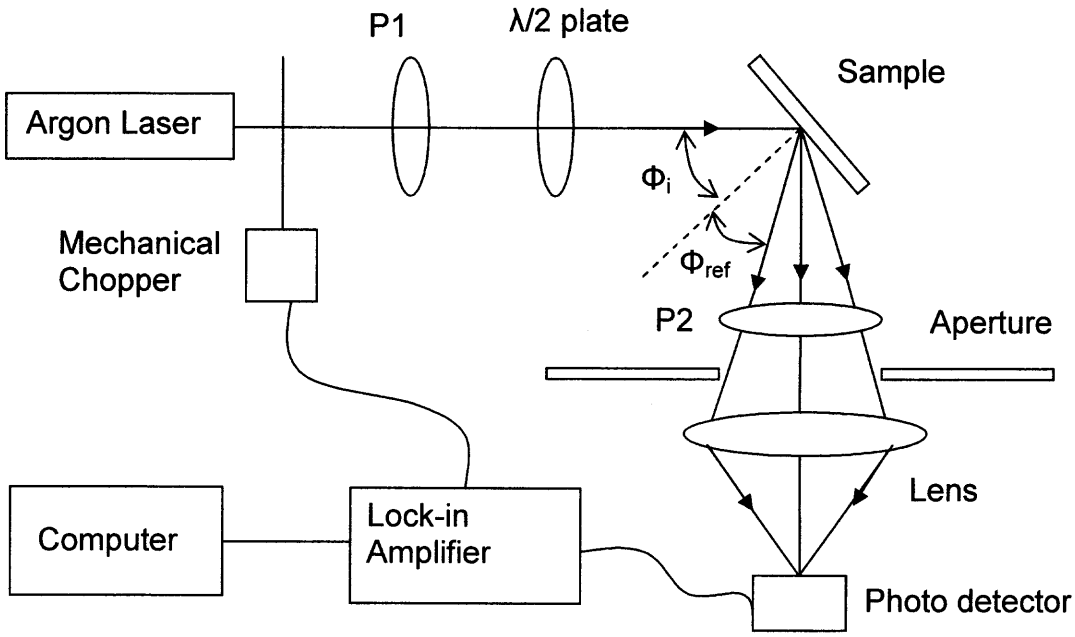

Figure 1.3 Experimental schematic in prior works: Argon laser laser light is reflected from the guinea pig skin sample. P1 and P2 are polarizing filters for the incident and the reflected light, respectively.
(Source: J. F. Federici et al.)

For the four skin samples (result shown in Figure 1.4)[6,7], normalized reflectivity (parallel polarizing component minus perpendicular polarizing component of the reflected light, then normalize to its initial value without stretch) increases almost linearly with the increasing applied stretch. The average data of the four samples yields the curve plot (dashed curve), which is closer to a straight line.

For latex materials with maximum stretch of 8.4%, reflectivities for both the parallel and perpendicular polarizations increase linearly with the stretch. But for stretches larger than 3%, the slope of the reflectivity becomes flatter (saturation occurs). The normalized reflectivity shows the same behavior. For the polyvinyl chloride sample (Figure 1.5)[6], no saturation of the normalized reflectivity is observed, and the normalized reflectivity vs. strain (stretch) plot is also close to a straight line.

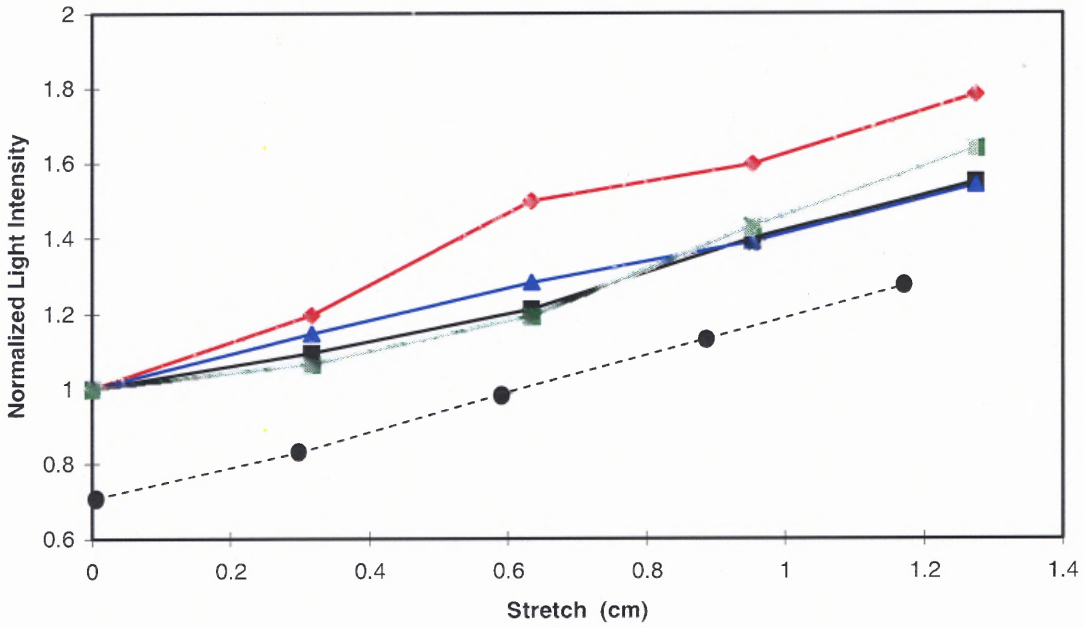

Figure 1.4 Solid curves are for four guinea pig skin samples, the dashed curve represents the average of the four plots and is shitted to the lower region of the figure for clarity. (Source: J. F. Federici et al.)

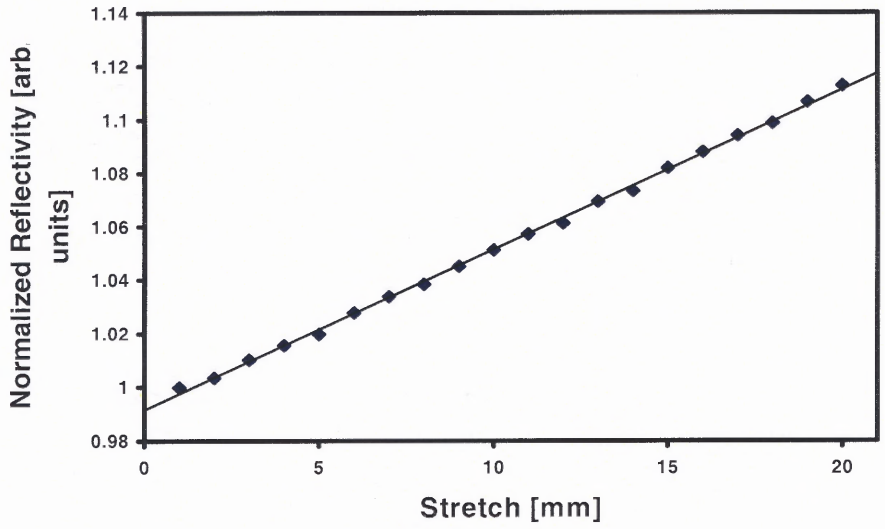

Figure 1.5 Normalized reflectivity for polyvinyl chloride sample with initial length of 45mm and maximum stretch of 19mm. Solid line shows the linear fit of the data. (Source: J. F. Federic et al.)

In this dissertation, preliminary work was carried out first to confirm and reproduced these results with the bulk optic system, then the system was transferred to fiber optic configurations. A variety of fiber configurations were investigated through a series of experiments. Theoretical analysis and numerical simulations were developed to explain and compare with the experimental data. A major goal of this work is to demonstrate whether a simple fiber optic system can replace the bulk optics system reported in prior works.

CHAPTER 2

THEORY AND MODELING

2.1 Surface Roughness Modeling

A simple 2-D sinusoidal model for the roughness of an interface was proposed in prior works[6, 8]: z=Asin(gx). With the very-rough-surface limit Ag>>1 and the basic ray optics approximation, it was demonstrated that the interface roughness, which decreases with increasing strain, explained the experimental results: (a) the observed increase in the specularly reflected light intensity, and (b) the linear relation between tissue stretch and reflectivity when the applied strain is small. Here, the term roughness is characterized by *A* and *g,* and is evaluated by their product *Ag*.

Despite the simplicity, this model yields fruitful results. The success originates from the fact that while the periodic-roughness assumption is not strictly true, the physiology of the various skin layers and topology measurements of skin show quasi-periodic interfaces between different layers of skin. Therefore, a periodic-roughness rather than a random-roughness model appears to be appropriate[6,7,56-58]. This model was originally suggested for the roughness of skin and was used to explain how the surface patterns of the skin change as a result of tension load. Later, it was shown mathematically by Federici's research group that the linear relationship between the normalized reflectivity and the applied strain is also applicable to common stretchable rough surfaces such as plastic or latex[59]. In this chapter, the existing theory will be expanded to include the modeling of fiber optic system with flat surfaces, and further expand the analysis to cover the curved surface condition with approximations.

2.2 Free Space Bulk Optics Analysis

2.2.1 Review of Prior Analysis

The theory developed in prior works is first reviewed. In the following Figure 2.1, collimated light is incident to the rough surface with angle Φ_i, a photo detector is put in the specular reflection direction of the incident light, $\Delta\varphi$ is the half angle of detection (optical acceptance angle). The power detected is expressed as:

$$P(\Phi_i) = -\iint_S r(\theta_i) I_0 \hat{k} \cdot d\vec{S} \tag{2.1}$$

where Φ_i and θ_i are the global and local incident angles respectively, $r(\theta_i)$ is the power Fresnell reflection coefficient, $d\vec{S}$ is the elementary surface being illuminated, $\hat{k}$ is the unit vector in the direction of incidence, and I_0 is the uniform incident light intensity. Within a satisfactory approximation, $r(\theta_i)$ can be treated as a constant $r(\Phi_i)$.

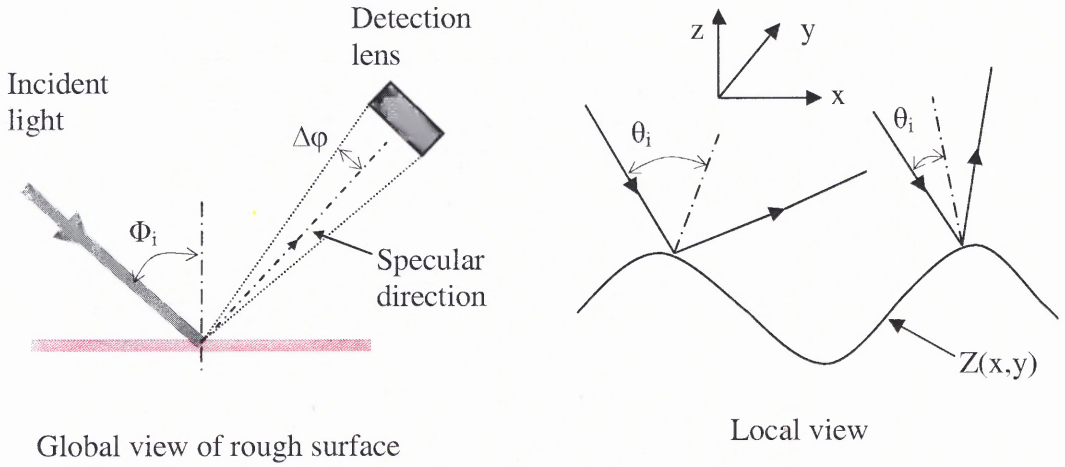

Figure 2.1 Surface roughness global and local views, the global and local definition of angles of incidence and reflection, orientation of the detector to the flat rough surface.

With sinusoidal surface roughness model *Z=Asin(gx)*, it is ready to evaluate the integral in Equation (2.1). The integral element surface $d\vec{S}$ and incident wave vector $\hat{k}$ can be replaced by the following expression in Cartesian coordinates:

$$d\vec{S} = (-\hat{x}\sqrt{\frac{A^2g^2\cos^2(gx)}{1+A^2g^2\cos^2(gx)}} + \hat{z}\sqrt{\frac{1}{1+A^2g^2\cos^2(gx)}})\sqrt{1+A^2g^2\cos^2(gx)}dxdy$$

$$\hat{k} = \hat{x}\sin\Phi_i - \hat{z}\cos\Phi_i$$

Substituting them into Equation (2.1) and simplifying, one obtains:

$$P(\Phi_i) = I_0 r(\Phi_i)\iint_S [Ag\sin\Phi_i\cos(gx) + \cos\Phi_i]dxdy$$

integrating in the y-direction yields:

$$P(\Phi_i) = L_y I_0 r(\Phi_i)\int_x [Ag\sin\Phi_i\cos(gx) + \cos\Phi_i]dx \qquad (2.2)$$

where L_y is the sample length illuminated by the laser beam in y-direction. The integration limit in the x direction will be determined later by $\Delta\varphi$.

Before evaluating the above integral, it is helpful to high-light several points, which will provide a basic picture of the relationship between the detected power and surface roughness, and hence the relationship between the normalized reflectivity and the stress applied on the soft tissue.

1. Assuming the cross section of the incident beam is very small, for small roughness sinusoidal surface and non-grazing incidence, the reflected light is confined within an angle range $\Delta\Phi$ set by the surface parameters A and g as illustrated in the following figure (Figure 2.2) and equations. For the sinusoidal surface model, one can easily obtain $\tan\frac{\Delta\Phi}{2} = Ag$. For cases that Ag is small enough, $\Delta\Phi = 2Ag$.
2. Since the stretching reduces the surface roughness, thus $\Delta\Phi$ will decrease and more light rays will be concentrated in the vicinity of the specular reflection direction. Therefore one observes increased power detection as the surface is strained.

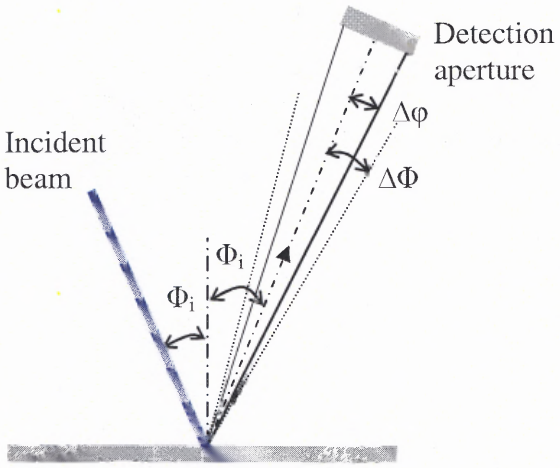

Figure 2.2 The reflected light is confined within an angle range $\Delta\Phi=2Ag$ set by the surface parameters A and g for small roughness cases.

3. If the initial surface roughness Ag is already a very small number, the angle $\Delta\Phi$ is so small that a detector will capture most of the reflected light, this corresponds to the effect of saturation at large scale of stretch.

In typical applications, the detection angle $\Delta\varphi$ is usually much smaller than the light spread angle $\Delta\Phi$. Light rays that strike the detector aperture originate from the reflection of light at the peak and bottom parts of the sinusoidal surface. Under this condition, the calculation of the detected power can be approximated by a simpler integration, and the integration range of x in Equation (2.2) above is determined by $\Delta\varphi$. Therefore, Equation (2.2) can be written as:

$$P(\Phi_i) = 2NL_y I_0 r(\Phi_i) \int_{x_1}^{x_2} [Ag \sin\Phi_i \cos(gx) + \cos\Phi_i] dx,$$

The two integrating limits are:

$$x_1 = \frac{\pi}{2g} - \frac{\Delta\varphi}{2g^2 A}, \text{ and } x_2 = \frac{\pi}{2g} + \frac{\Delta\varphi}{2g^2 A}$$

N is the number of periods of the sinusoidal surface under the illumination of the laser beam, that is $N = L_x \cdot \frac{g}{2\pi}$. The above integral can be readily evaluated,

$$P(\Phi_i) = L_y I_0 r(\Phi_i)\cos(\Phi_i) L_x \frac{\Delta\varphi}{\pi g A} \tag{2.3}$$

$$P(\Phi_i) = P_0 \frac{\Delta\varphi}{\pi A g} \tag{2.4}$$

where $P_0 = L_x L_y I_0 \cos(\Phi_i)\cdot r(\Phi_i)$ is simply the incident power times the reflection coefficient, which corresponds to the specular reflection power for the perfect smooth surface case.

Equation (2.4) reasonably explains the relationship between the detected power and surface roughness. However, this equation does not directly link the reflectivity change of the surface to the strain of the soft tissue. The surface mechanical properties will determine how the surface topology changes when the strain is applied to the sample. A simple model assumes that the surface path length is a constant during stretch, such that only A and g change accordingly. This model is accepted in discussing the property of skin under strain. Using this model, the prior work has shown that at very rough surface condition, the surface reflectivity is linearly proportional to the stretch:

$$P(\Phi_i) = P_0 \Delta\varphi \frac{4\Lambda M}{\pi^2 L}, \text{ or simply } P = k\Lambda \tag{2.5}$$

where $\Lambda = 2\pi/g$ is the spatial period of the sinusoidal surface, k is a constant. From Equation (2.5), k can be written as:

$$k = 4P_0 \Delta\varphi \frac{M}{\pi^2 L}$$

where M is the constant number of surface oscillations, L is the constant surface path length in x direction.

The normalized power is then:

$$\frac{P}{P_i} = \frac{g_0}{g}$$

It is clear that the normalized power (reflectivity) here is only related to the surface parameter g, but not related to the amplitude A. While this is a good approximation for very rough surfaces, it would cause considerable errors when dealing with surfaces with moderate roughness such as human skin (A~60μm, g~50 μm^{-1}). This dilemma arises because the calculation of the surface path length is over simplified in the very rough surface approach, in which the period path length of the ripples is just the zeroth order approximation (only amplitude is considered) instead of a higher order one. For some applications, various surface roughness conditions should be considered, and it is also desired to link the slope k of the linearity in the above relation to the surface parameters A and g in the sinusoidal model. To serve this purpose, the same model will be used, but a higher order approximation in evaluating the surface path length is necessary to be developed.

2.2.2 First Order Approximation

Let A_0, g_0 be the initial surface parameters before strain. Again it is assumed that the strain only changes A_0 and g_0, but does no change the surface path length. Let L_0 be the path length of one oscillation (not sample length or special period). Let A and g be the parameters of the surface when it has strain S, which is defined as the ratio of the extended length to its initial length. The following relations hold:

$$g = \frac{g_0}{1+S} \tag{2.6}$$

$$L_0 = \int_0^{2\pi/g_0} \sqrt{1 + A_0^2 g_0^2 \cos^2(g_0 x)}\, dx \tag{2.7.1}$$

$$L_0 = \int_0^{2\pi/g} \sqrt{1 + A^2 g^2 \cos^2(gx)}\, dx \tag{2.7.2}$$

The elliptical integrals in Equation (2.7.1) and Equation (2.7.2) are evaluated. From the geometry, this kind of integral can be evaluated by the triangle approximation (first order). Simply the integrals are expressed as:

$$L_0 = 4\sqrt{A_0^2 + \frac{\pi^2}{4g_0^2}} = 4\sqrt{A^2 + \frac{\pi^2}{4g^2}} \tag{2.7.3}$$

Substituting Equation (2.6) into above equation, one obtains:

$$\sqrt{A_0^2 + \frac{\pi^2}{4g_0^2}} = \sqrt{A^2 + \frac{\pi^2 (1+S)^2}{4g_0^2}}$$

solve for A,

$$A = \sqrt{A_0^2 - \frac{\pi^2}{4g_0^2}(S^2 + 2S)} \tag{2.8}$$

Equation (2.6) and (2.8) describe the behaviors of surface parameters A and g under the strain of the surface, when the first order of approximation is applied.

Recall Equation (2.4), the ratio (normalized reflectivity) of the detected power P with strain S to the initial power P_i without strain can be obtained:

$$R_{Normalized}(S) = \frac{P}{P_i} = \frac{1+S}{\sqrt{1 - \frac{\pi^2 (S^2 + 2S)}{4A_0^2 g_0^2}}} \tag{2.9}$$

One should notice that in Equation (2.9), the value of $\frac{\pi^2(S^2+2S)}{4A_0^2g_0^2}$ must be less than 1. Obviously this restriction is generated by the condition that the surface path length does not change with strain. Referring to Equation (2.8), the strain can increase until the amplitude A=0. For this condition, $A_0^2g_0^2=\frac{\pi^2}{4}(S^2+2S)$. As the strain S increases, the surface becomes more and more "unstretchable". For already very small A and g values, there is no much strain available, thus S is restricted to a very small number, before the A=0 flat smooth surface condition occurs. One also notices that as S increases, the value of $\frac{\pi^2(S^2+2S)}{4A_0^2g_0^2}$ will approach 1 resulting in the singularity of the ratio, which is not physical at first glance.

However, one should remind that Equation (2.9) is obtained under the approximation of small detection angle. During the stretch, the detector acceptance angle is a constant in the experiment. As the strain increases, the values of A and g decrease, eventually the light spread angle $\Delta\Phi = 2Ag < \Delta\varphi$, which causes the saturation of the detected power as already high lighted before in this Chapter. To summarize, Equation (2.9) applies to the conditions that the stretch is not approaching the limits set by the surface model and its roughness parameters.

Numerical calculation shows (Table 2.1) that the triangle approximation of Equation (2.7.3) in evaluating the path length of the sinusoidal curve is valid for a large range of surface roughness values. The validity of Equation (2.7.3) has been tested for both small and very large A_0g_0 values. In Table 2.1, the percentage difference of the approximation obtained through comparing with rigorous path length for Ag values

ranging from 0.1 to 100 are listed, and the maximum difference is only about 3.5%, which occurs when Ag value equals 3. Although higher order approximation may give more precise result, it appears not necessary to do so, since the first order approximation already yields enough accuracy. Moreover, it is very difficult to obtain an analytical and simple result like Equation (2.9) for higher order approximations.

Table 2.1 Percentage Difference of Surface Path Length between Rigorous Values and Approximated Values

Ag value	0.1	0.2	0.5	1	2	5	10	20	50	100
% difference	0.05	0.2	1	2.5	3.5	2	1	0.3	0.07	0.02

A direct approximation of Equation (2.9) is that in the limit of a very rough surface, where $A_0 g_0 >> 1$, the normalized reflectivity is simply:

$$\frac{P}{P_i} = 1 + S \tag{2.10}$$

Equation (2.10) can also be directly obtained from the zeroth order approximation by applying Equation (2.6). One can see that the first order approximation reduces smoothly to the zeroth order approximation in the very rough surface condition.

2.2.3 Numerical Test of the Approximation

In order to better understand how the surface reflectivity behaves under strain, the normalized reflectivity $\frac{P}{P_i}$ vs. strain S is plotted using Equation (2.9) for various surface roughness values. Starting with small roughness case, the plots are shown in the following figures (Figure 2.3 through Figure 2.5).

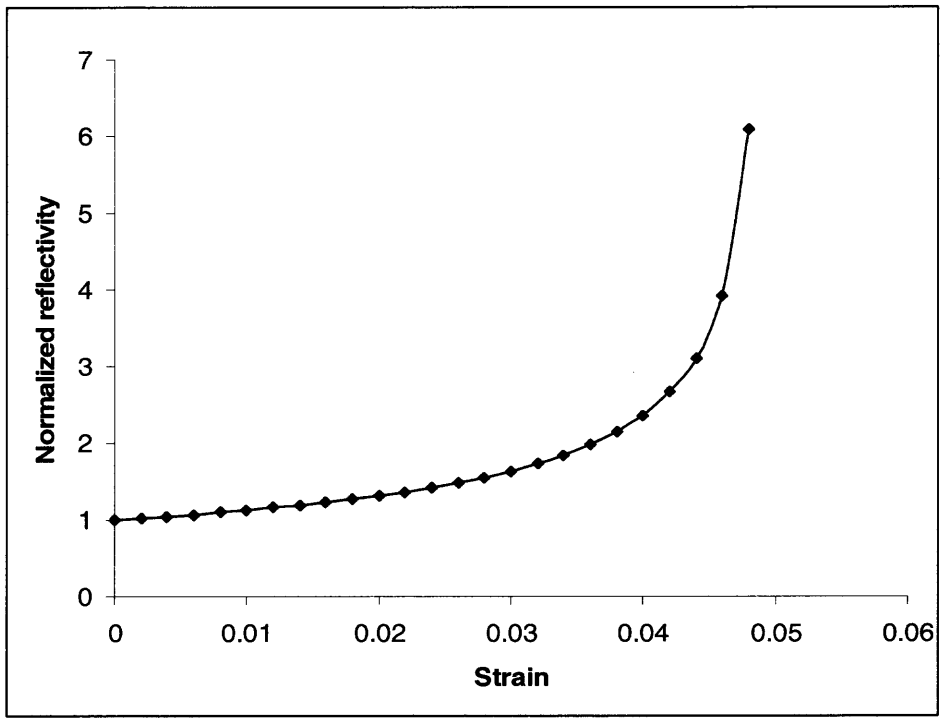

Figure 2.3 Initial surface roughness $A_0 g_0$=0.5, linearity between the normalized reflectivity and strain is valid for strain less than 3%.

Figure 2.3 shows the normalized reflectivity $\frac{P}{P_i}$ (y-axis) vs. strain ΔL/L (x-axis) for initial surface roughness $A_0 g_0$= 0.5. One should not be surprised that in Figure 2.3 singularity appears when the strain approaches a point somewhere between 0.04 and 0.05. It is also clear that the linearity still holds for strain less than 0.03, that is 3% of stretch, and the slope value is about 20.

Figure 2.4 shows when the surface initial roughness $A_0 g_0$=1, the linearity holds up to a strain value of 0.1 corresponding to 10% of stretch, and the slope of the linearity is about 5, which is greatly reduced compared with the previous plot in which $A_0 g_0 = 0.5$.

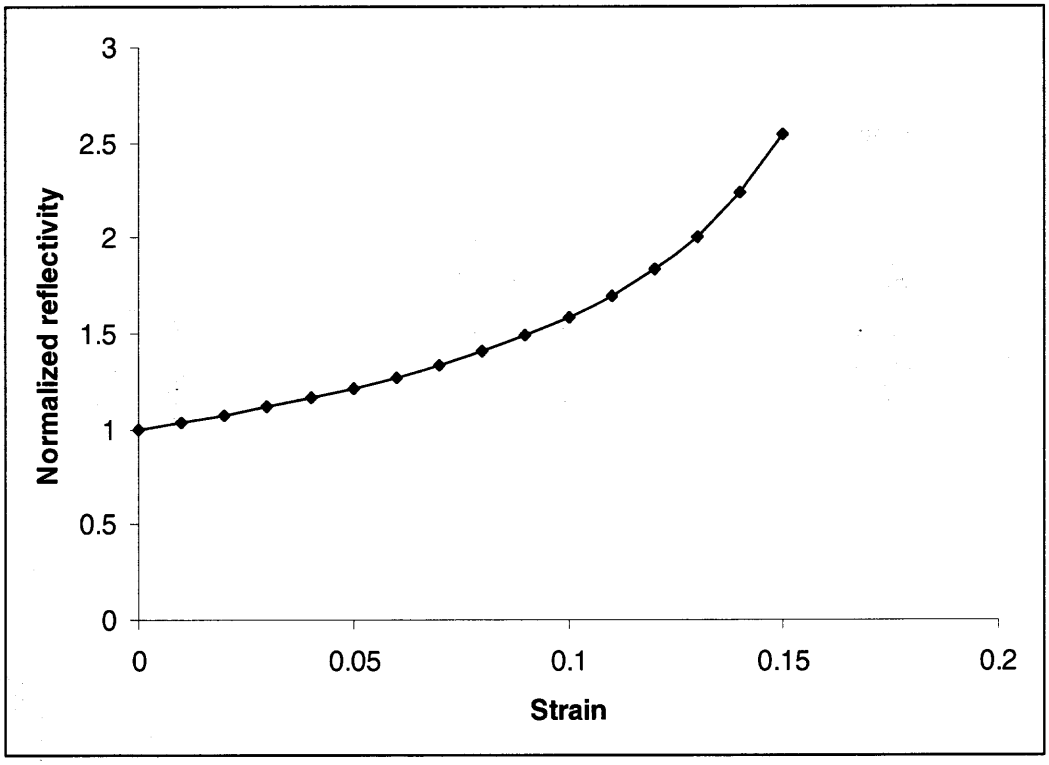

Figure 2.4 With initial roughness $A_0 g_0$=1, the linearity is well maintained until the strain excesses 10%, but the slope of the linearity decreases compared with the previous case where $A_0 g_0$= 0.5.

It is shown in Figure 2.5 that as surface roughness $A_0 g_0$ increases, the linearity range increases, and the slope decreases. For $A_0 g_0$=2, the linearity holds up to 15% of stretch, and the slope is about 2; for $A_0 g_0$=3, 4, 5, with stretch less than 20%, the linearity well holds, and the slopes are about 1.3, 1.25 and 1.2, respectively. Comparing with Equation (2.5), which predicts a constant slope for very large surface roughness, this approach can predict a wide range of slope values for moderate surface roughness and meanwhile provides a linear region. It is clear that as the surface roughness increases, the slope approaches a constant, and the linear range increases accordingly, which is in agreement with the result of prior work.

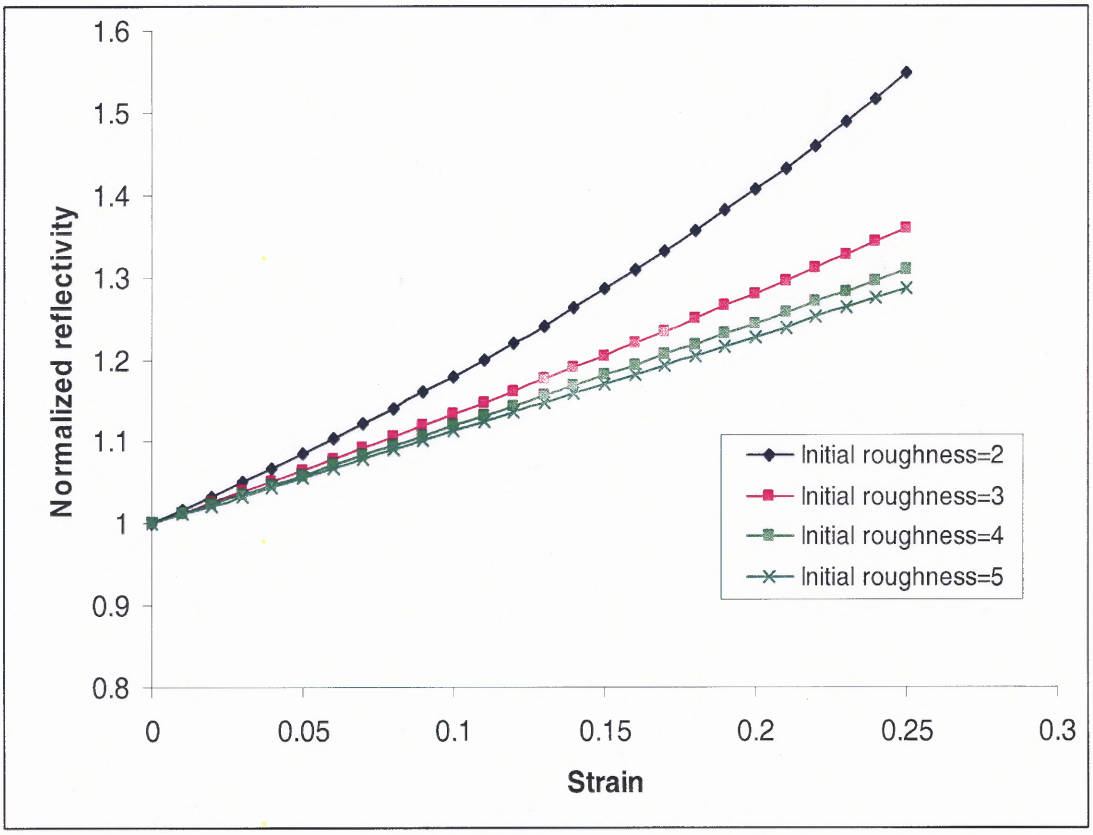

Figure 2.5 Normalized reflectivity for surface initial roughness $A_0 g_0$ =2, 3, 4, 5 as marked in the plot. As the roughness increases, the linear range of the relationship between the normalized reflectivity and the strain increases, however the slope of the linearity decreases.

2.2.4 Linearization of the Result

In most applications, where the strain is limited in the linear range, Equation (2.9) can be reduced to a linear expression about the strain. As shown above, the slope of the linearity and the linear range can be determined from the surface initial parameters through plotting of Equation (2.9) with mathematical tools. For application convenience, Equation (2.9) can be written as:

$$R_{Normalized} = \frac{P}{P_i} = 1 + kS \tag{2.11}$$

where k is the slope obtained through the numerical plot of Equation (2.9). The estimated linear range for strain S and the slope k for different initial roughness $A_0 g_0$ of the surface are listed in the following table (Table 2.2).

Table 2.2 Slope and Linear Range of Strain Determinations

$A_0 g_0$	0.5	1	2	3	4	5
k	20	5	2	1.3	1.25	1.2
S range	< 3%	< 10%	< 15%	< 25%	< 35%	< 50%

A direct result from the numerical plots and Table 2.2 is that the slope k must be no less than 1, and equals 1 only when Ag is essentially infinity, corresponding to very rough surfaces. It is easy to verify this result by differentiating Equation (2.9) and noticing that $S>0$.

$$k = \frac{dR_{Normalized}(S)}{dS} = \frac{[1-\frac{\pi^2(S^2+2S)}{4A_0^2 g_0^2}]^2 + \frac{\pi^2(1+S)^2}{4A_0^2 g_0^2}}{[1-\frac{\pi^2(S^2+2S)}{4A_0^2 g_0^2}]^{5/2}}$$

$$> \frac{1}{\sqrt{1-\frac{\pi^2(S^2+2S)}{4A_0^2 g_0^2}}} > 1$$

2.2.5 Discussion and Summary

As discussed before, when the value of $A_0 g_0$ decreases, the slope of the linearity increases if the relation $\Delta\Phi = 2Ag > \Delta\varphi$ still holds. However, when 2Ag is less than $\Delta\varphi$ due to the continuing strain, saturation occurs. Therefore, the above plots must be apodized to include the saturation effect at the approaching of the limit of stretch. It is

justifiable to conclude that the complete real plot of the normalized reflectivity vs. strain can be qualitatively drawn as in the following figure (Figure 2.6).

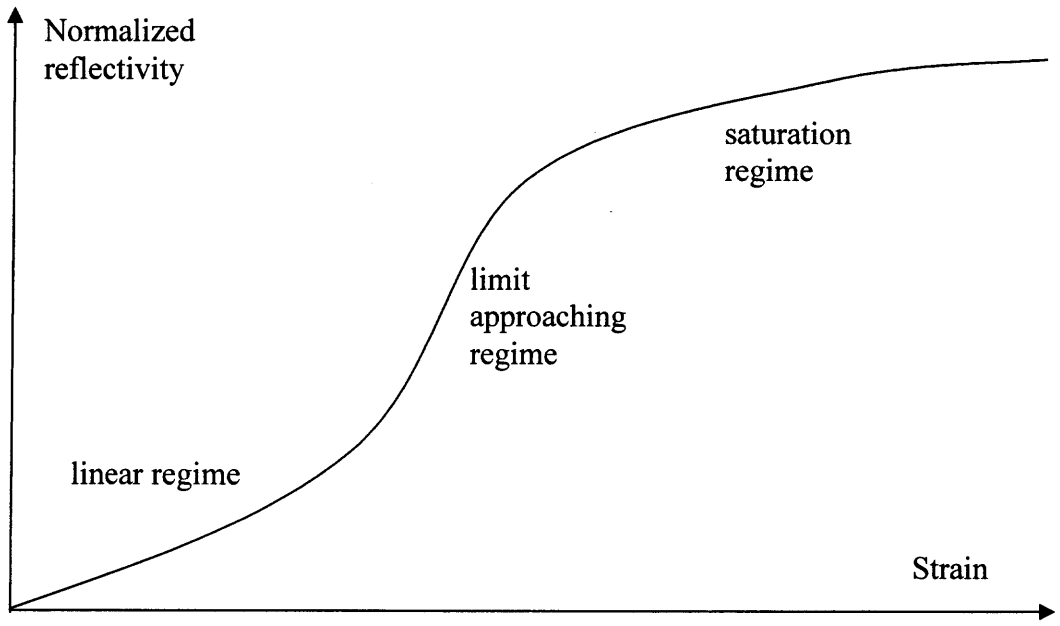

Figure 2.6 Three operation regimes are shown. For most applications stretches are within 15%, and linearity is expected to hold during the stretch for rough surface cases.

The above analysis is based on the free space bulk optics configuration, where the incident beam is highly collimated. In a fiber optics configuration, some assumptions and conditions required by the above approach may no longer be valid. However, this analysis provides basic understanding and a clear physical picture on how strain changes the reflectivity of rough surfaces. With a fiber optics configuration, under further approximation and with help of numerical analysis method, it is found that above result is still valid for various fiber configurations, even though the incident beam is not highly collimated.

2.3 Analysis on Fiber Optics Configuration

In the fiber optics schematic, the incident and collecting fibers are assumed to have the same specifications. The fiber orientations are fixed in the specular reflection direction. The distances between the end facets of the fibers and the sample are all equal. While this simplification may loose some generality of the treatment, it provides basic knowledge of the fiber system. From this model, it is still convenient to accommodate a more general treatment such that the incident fiber and receiving fiber have different specifications. The fiber facet to sample distance can vary as well. The fiber optics schematic is shown in Figure 2.7. It is convenient to treat the problem in three configuration categories according to the comparison between the numerical aperture (NA) of the incident fiber or the divergence of the incident light and the detection acceptance angle. In the discussion below, the NA is replace by θ_0 knowing that NA=$\sin\theta_0$ (No miniature collimating lens is used).

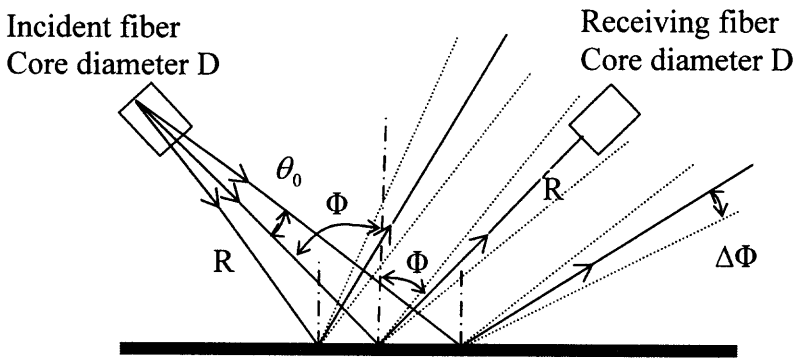

Figure 2.7 Fiber incident and detection schematic. R is the fiber to surface distance, D is the fiber core diameter, θ_0 is the incident divergence angle, $\Delta\Phi$ is the light spread angle after reflection.

2.3.1 Small Divergence and Acceptance Angles Probing

For this configuration, mathematically $\theta_0 << 1$, D/R <<1, the incident beam is narrow and can be treated as collimated beam to good approximation. Therefore the results reduce to the free space bulk optics case discussed previously. For telecommunication single mode fibers, the typical NA is about 0.1, D is around 10μm, and R is usually greater than 1mm in typical applications. Although the above conditions are obviously satisfied, this fiber configuration possesses short comings such as small acceptance angle of the receiving fiber which results in a small detected power. Thus this configuration has very limited use in most applications.

2.3.2 Divergent Beam Long Distance Probing

When θ_0 >>D/R, D/R<<1. At this condition, the incident beam is divergent, and the detection distance is much larger than the diameter of the receiving fiber. Thus, in this case the illumination area on the sample is much bigger than the physical aperture of the receiving fiber. It is difficult to calculate the power detected by the receiving fiber, since the integration of the optical power reflected from different directions and positions on the surface is extremely complicated.

However, an approximation can be made to simplify this problem. Considering that the central light rays that form the center stripe of the spot on the sample (Figure 2.8) contribute most to the detected power, one can neglect the contribution from peripheral rays, and the calculation of the detected power can be greatly simplified. Further because θ_0 (or NA) of the receiving fiber is much larger than the physical aperture acceptance angle (D/R) of the receiving fiber, reflected rays impeding on the facet of the fiber will all be collected. The NA of the fiber plays no role in determining which rays can be

eventually captured by the fiber and can propagate to the detector end through it. The optical acceptance angle is determined by the physical aperture of the receiving fiber for this case.

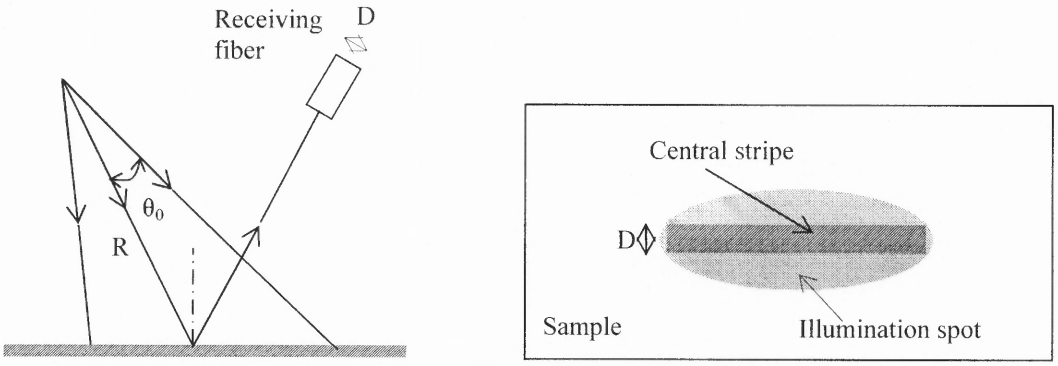

Figure 2.8 Far field configuration. The central light rays that form the stripe in the center of the spot on the sample contribute most to the detected power, while the contribution from peripheral rays can be neglected.

From Figure 2.8, one may set the width of the central stripe to be the diameter of the fiber core D, and the length of the stripe is approximately $2R\theta_0$. Assuming the incident optical power has a uniform distribution in all direction, and considering the projection effect, one can conclude that the ratio of the optical power in the stripe to the total power in the spot is simply:

$$\frac{2DR\theta_0}{\pi(R\theta_0)^2} = \frac{2D}{\pi R\theta_0}.$$

The effective incident power (collimated case equivalent power) can be written as $\frac{2D}{\pi R\theta_0} P_0$. Applying Equation (2.4), the detected power can be written as:

$$P = \frac{2D}{\pi R\theta_0} P_0 \frac{\Delta\varphi}{\pi Ag}$$

where P_0 is the reflection power for perfect smooth surface cases, and is still the same expression as in Section 2.2, except that L_xL_y is replaced by $\pi(R\theta_0)^2$. To a good approximation: $\Delta\varphi = \frac{D}{2R}$

Substitute into the previous equation yields:

$$P = P_0 \frac{D^2}{\pi^2 R^2 \theta_0 Ag} \tag{2.12}$$

One can find that the $(Ag)^{-1}$ relation still holds, hence Equation (2.9) also holds for this fiber optics configuration. It is rewritten here for clarity:

$$R_{Normalized}(S) = \frac{P}{P_i} = \frac{1+S}{\sqrt{1-\frac{\pi^2(S^2+2S)}{4A_0^2 g_0^2}}} \tag{2.9}$$

P_i is still the detected optical power before the strain is applied.

It should be pointed out that the above treatment employs very rough and bold approximations in calculating the optical power detected by the receiving fiber. However, since only the normalized power (reflectivity) is the final result of interest, most of the inaccurate assumptions of the calculation are eliminated by the process of normalization. Equation (2.9) is still valid, even though the treatment seems overly approximated. A more convincing and simple way to tackle this problem is numerical simulation through computers. This configuration applies to the application system in which the fibers are multimode, and the fiber to sample distance is much larger than the fiber diameter.

2.3.3 Divergent Beam Short Distance Probing

When θ_0 ~ D/R, and D is in the same order of R (but smaller than R for most application circumstances). As shown in Figure 2.9 below, the illumination spot on the sample consists of two regions I and II. Region I is formed by paraxial rays (with divergence angle less than θ_1) in the incident light cone. θ_1 is determined this way such that any ray ending in region I at the point represented by $\vec{r}$ will be diffusively reflected such that the receiving fiber is essentially oriented in the specular reflection direction for this ray. Consequently, the numerical aperture of the receiving fiber will not affect the collection of rays (all rays impeding the core area of fiber end surface will be captured by the receiving fiber). Region II is formed by peripheral rays in the incident light cone (with divergence angle larger than θ_1 and smaller than θ_0). In this region reflected light rays hitting the end surface of the fiber can be eventually collected by the fiber or simply escape the fiber later.

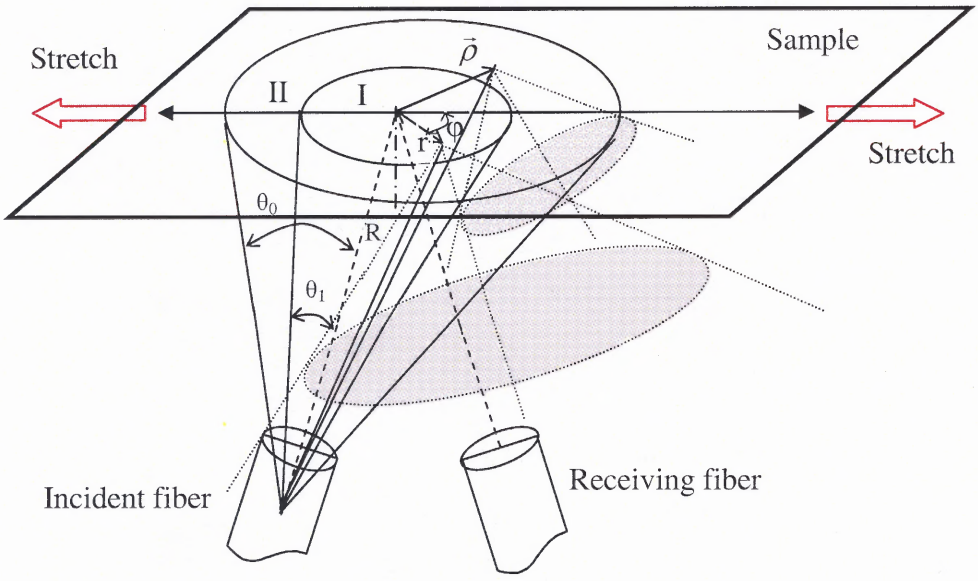

Figure 2.9 Near field configuration. The illumination spot on the sample is divided into two regions: The paraxial region I and the periphery region II.

The rigorous calculation of the collected optical power leading to an analytical solution for region II is extremely complicated even with approximations. By dividing the light spot into two regions, the complexity of the calculation, in which one has to determine if a ray is collected by the receiving fiber or not when it hits the fiber end surface, can be reduced. As shown in Figure 2.9, the total detected power for region I comes from the integration of the reflection of individual collimated beam elements with different incident angles. Again, with assumption that the optical intensity is uniform within the incident light cone with divergence angle θ_0 is employed. Let p_0 be the incident optical power per unit solid angle. According to Equation (2.3), the analytical solution of the detected power in region I can be expressed by the following integral:

$$P_1 = \int_0^{2\pi} \int_0^{\theta_1} p_0 \sin\theta \cos[f(\theta,\varphi,\Phi_i)] r[f(\theta,\varphi,\Phi_i)] \frac{\Delta\varphi}{\pi A g} d\theta d\varphi \qquad (2.13)$$

where $f(\theta,\varphi,\Phi_i)$ is the element light beam incident angle function. The form of this function is complicated due to its 3-dimension nature, but it has no significant effect on the calculation of normalized power, because integral P_1 is evaluated only for the inner light cone, which is essentially a collimated light beam. For good approximation, it can be written as $f(\theta,\varphi,\Phi_i) = \Phi_i$. Thus, for normal incidence, $\cos[f(\theta,\varphi,\Phi_i)] = 1$. $\Delta\varphi$ in Equation (2.13) is the receiving fiber acceptance angle. Rigorously, $\Delta\varphi$ must be a function of θ and φ. However, as discussed in this part before, this acceptance angle can be replace with an averaged angle by approximation, it is simply the smaller of the numerical aperture angle θ_0 and D/R. Since $\theta_0 \sim D/R$, by arbitrarily letting $\Delta\varphi = \theta_0$, and this will not affect the calculation of normalized power. θ_1 is still to be determined as discussed before.

With the help of above approximations, the right side of Equation (2.13) can be integrated, and the equation reduces to a much simpler form:

$$P_1 = 2p_0 \cos(\Phi_i) r(\Phi_i)(1-\cos\theta_1)\frac{\theta_0}{Ag} \tag{2.14}$$

Compared with region I, light rays striking in region II at point represented by $\vec{\rho}$ (Figure 2.9) are reflected to the end of the fiber strongly deviate from the specular reflection direction of the entire incident light cone. It is obvious that the reflection behavior at different positions in region II widely varies. The detected optical power associated with this region still can be written in a general analytical form represented by a complicated integration:

$$P_2 = \int_0^{2\pi}\int_{\theta_1}^{\theta_0} p_0 r[f(\theta,\varphi,\Phi_i)]\cos[f(\theta,\varphi,\Phi_i)]a(\theta,\varphi,\Phi_i)\frac{\Delta\varphi(\theta,\varphi,\Phi_i)}{\pi Ag}\sin\theta d\theta d\varphi \tag{2.15}$$

The reflection angle function $f(\theta,\varphi,\Phi_i)$ may not be simplified as Φ_i, and $\Delta\varphi(\theta,\varphi,\Phi_i)$ can not be approximated as a simple function of D/R or θ_0. Since the detection fiber is not paraxial for region II. In order to apply Equation (2.3), an effective paraxial coefficient $a(\theta,\varphi,\Phi_i)$ is introduced to reduce the complexity of Equation (2.15).

With above analysis, the total detected optical power is:

$$P = P_1 + P_2 \tag{2.16}$$

The evaluation of P_2 is formidable, however, since $f(\theta,\varphi,\Phi_i)$, $\Delta\varphi(\theta,\varphi,\Phi_i)$, and $a(\theta,\varphi,\Phi_i)$ are all independent of A and g, P_2 can be simply written as:

$$P_2 = p_0 c(\theta_1,\Phi_i)\frac{1}{\pi Ag} \tag{2.17}$$

The total power can be expressed as:

$$P = 2p_0 \cos(\Phi_i) r(\Phi_i)(1-\cos\theta_1)\frac{\theta_0}{Ag} + p_0 c(\theta_1, \Phi_i)\frac{1}{\pi Ag}$$

it can be further written as:

$$P = c'(\theta_1, \Phi_i)\frac{1}{Ag} \tag{2.18}$$

Where $c'(\theta_1, \Phi_i)$ absorbs all the coefficients of $(Ag)^{-1}$.

It is evident that if θ_1 in the coefficient $c'(\theta_1, \Phi_i)$ is independent of A or g, Equation (2.9) would hold for this case, and all the three cases discussed here would be reduced to the simple free space bulk optics case.

Now it is ready to discuss how to evaluate the value of angle θ_1. The key question is whether θ_1 depends on A or g. The following arguments show that θ_1 does depend on A and g if the surface roughness is very small, that is Ag<<θ_0 and D/R. Since, according to the high lighted points in Section 2.2 in this Chapter, the reflected light spread angle $\Delta\Phi$ is $2Ag$, in order for the reflected light of the left most rays (Figure 2.9) in the small cone to be collected by the receiving fiber, the cut off condition $2Ag + \Phi_i - \theta_1 = \Phi_i$ must hold, thus $\theta_1 = 2Ag$. This result makes the normalization of Equation (2.18) very complicated, and a simple analytical expression of $c'(\theta_1, \Phi_i)$ is essentially impossible to obtain considering the complexity of the functions $f(\theta, \varphi, \Phi_i)$, $\Delta\varphi(\theta, \varphi, \Phi_i)$, and $a(\theta, \varphi, \Phi_i)$. For larger Ag values, since the spread angle is larger, the cut off condition is not necessary, one expects much less dependency of θ_1 on Ag values, thus by approximation, Equation (2.18) can be simply normalized and yield the same result as the bulk optics case.

It is convenient to determine θ_1, $c'(\theta_1, \Phi_i)$ and the total optical power in Equation (2.16) through numerical simulations. Fortunately, in most applications the surface roughness Ag is much larger than the N.A. of the fibers, hence, the approximations discussed in previous paragraphs are reasonably adoptable. It is further shown later in the experiments, that the treatment discussed in this section yield acceptable accuracy.

The above analysis for the three fiber configurations is more qualitative than quantitative, since many approximations are made in the calculation. Although not rigorous, this analysis explores the complexity of the problem and provides the first approach on understanding of the issues in adapting polarization imaging technique to fiber optic implementation. Moreover, this theoretical formulation can serve as a control for both numerical simulations and experimental results. The following part of this Chapter will employ numerical methods to determine the dependence of the measured change in reflectivity with the strain in the sample.

2.4 Analysis on Curved Surfaces

The previous section discussed the fiber optics configurations for the flat rough surface applications. It is natural to extend that analysis to the curved surface cases with fiber optics configurations. In the modeling, a partial cylindrical surface with curvature C along the surface sinusoidal ripple direction ($\vec{g}$ direction) is selected for its simplicity; the stretch along the tangential direction of the cylindrical surface is assumed; and during the stretch, the surface curvature C is a constant. Two sensing applications are considered: convex surfaces (not shown) and concave surfaces (shown in Figure 2.10). For convex application, the fibers are located on the opposite side of the surface from the center of

curvature. ρ is the curvature radius. The amplitude of the roughness is exaggerated in the figure for clarity. The incident fiber and the receiving fiber are kept parallel and both are in the normal direction relative to the average surface in the treatment.

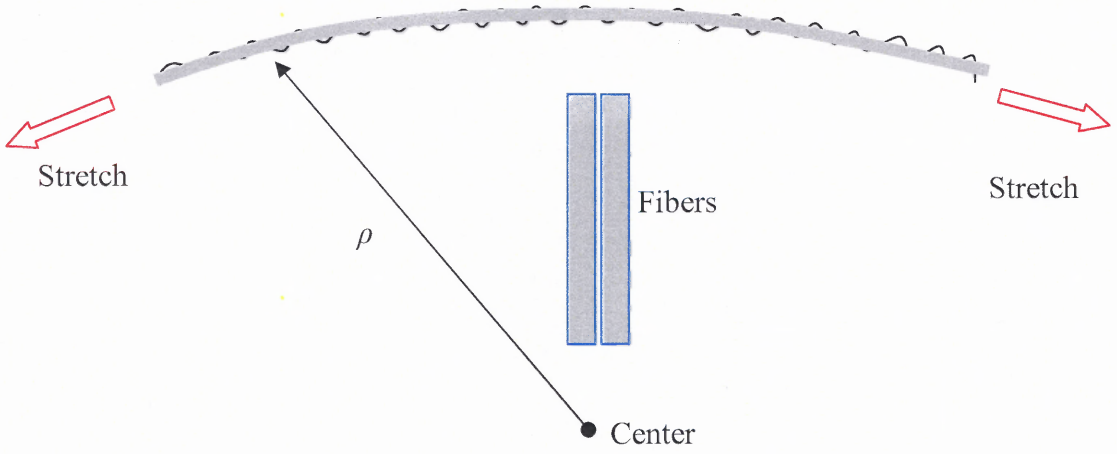

Figure 2.10 Cylindrical surface with sinusoidal roughness model. ρ is the radius of the cylinder, and the stretch is applied along the transverse direction. The incident fiber and the receiving fiber are kept parallel and both are in the normal direction relative to the surface.

It is obvious that if the radius ρ is much larger than the fiber diameter, this curved surface case will reduce to the flat surface condition, and the reflectivity behavior of the surface under stretch would be the same. As already seen from the flat surface applications, analytical solution for this case is even more difficult to obtain. A numerical method thus will be employed.

2.5 Numerical Simulations by Ray Tracing

In order to simulate the application and compare with the results from experiments, the simulation conditions are selected to be as close to the realistic implications as possible. In the simulations, all the fiber configurations of the detector head and the spacing

between the sample and the fiber end surfaces are exactly the same as in the experiments. However, the surface roughness parameters A and g can not be directly measured in the experiments. Empirical values of A and g extracted from the comparison with the analytical plots are employed in the simulation.

Simulation Assumptions

1. The incident fiber and receiving fiber are identical.
2. The incident light intensity is uniform (a Gaussian intensity distribution may be employed alternatively) and in TE incident mode.
3. Assume no interference or laser speckling.
4. The surface roughness is sinusoidal, and the stretching does not change the surface path length or modify the optical property of the local region of the surface.
5. The surface elements are treated as pure mirrors with identical reflectivity, thus the Snell's power reflection coefficient is the same for any ray and any local condition. This approximation dramatically reduces the computing tasks in the simulation.

Algorithms

With the help of *Mathematica* and its add-on component *Optica*, a ray tracing method is employed. The incident light from the fiber consists of thousands of individual light rays, and each ray is traced for its path through the entire optical system, at the remote end of the receiving fiber the number of rays is counted and recorded as detected optical power. The simulation flow chart is shown in the following diagram (Figure 2.11).

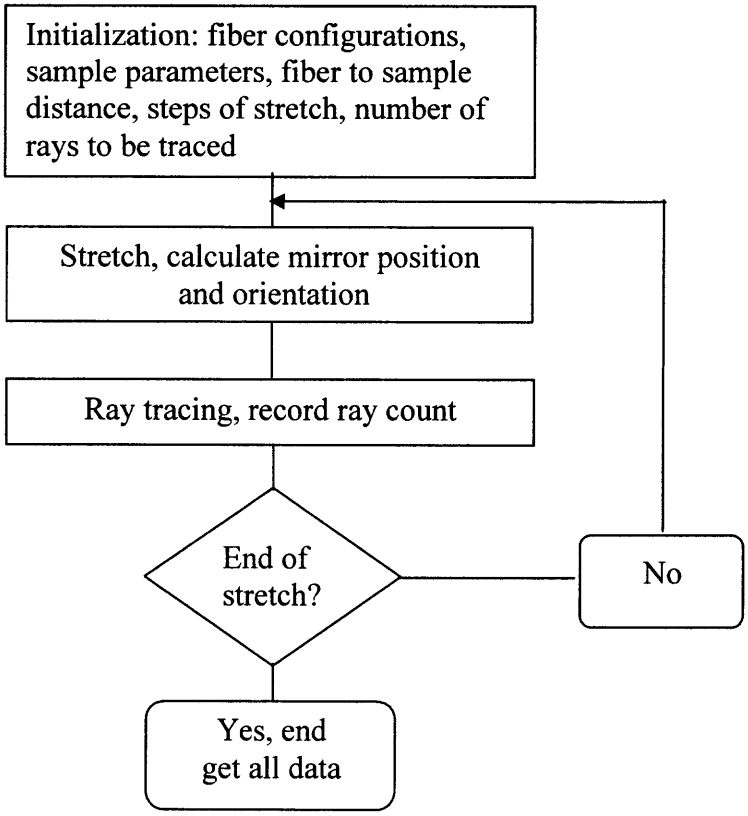

Figure 2.11 Ray tracing program flow chart.

Since the ray tracing occupies significant computing resources, the element mirrors which are obviously not in the position and orientation which causes a ray to impede the facet of the receiving fiber are eliminate in the optical system to save computing time.

The flat surface condition and the curved surface condition are simulated separately. These numerical results will be presented in Chapter 4, and will be compared with the experimental results as well as the analytical solutions discussed previously.

2.6 Young's Modulus Extraction from the Reflectivity Measurement

For strain S that falls in the linear range of the relationship with the stress σ, a simple equation (Hooke's law) can be applied for soft tissue materials:

$$\sigma = YS$$

where Y is the Young's modulus of the soft tissue along the strain direction. If further the strain S is also within the limit of the linear range of the relationship with normalized reflectivity, which is very likely, Equation (2.11) can be applied to link the normalized reflectivity to the applied stress and Young's modulus of the material:

$$R_{normalized} = 1 + \frac{k}{Y}\sigma \tag{2.19}$$

If in the experiment, σ can be measured as well as the normalized reflectivity, the linear plot between them would yield the extraction of the Young's modulus, provided the surface roughness condition is known already. Likewise, Equation (2.19) can be used to evaluate the stress in the material, if Young's modulus of that material is known.

CHAPTER 3

EXPERIMENTS

In this Chapter, the experimental methods and fiber probe preparations will be described in detail. Starting with the bulk optic experimental setup, the linearity between the normalized reflectivity and the stretch on the surface is examined. The structure of the fiber probe then discussed, and the fabrication and packaging of the fiber probe assembly is documented in detail. The flat and curved surface fiber optic experimental setups and methods are illustrated later. Labview programs were developed for data collection during the experiments.

3.1 Bulk Optic Experiment on Latex and Polyvinyl Materials

Several types and geometrical sizes of the latex glove materials are stretched and the corresponding reflectivity is measured. The experimental setup is shown in Figure 3. 1. Linearly polarized light from He-Ne laser (λ=632.8μm) is directed through the optics to the latex sample and diffusively reflected. The light collecting optics is positioned at the specular reflection direction with an linear polarizer in front. One end of the sample is mounted on the stress sensor, which is mounted on one of the step motor stages to measure the stress during the strain process. The half-wave plate is used to adjust the polarization of the incident light on the sample. Both of the parallel and perpendicular polarization powers of the reflected light are measured as a function of the strain in the sample. Phase sensitive detection techniques are employed with a mechanical chopper and a lock-in amplifier. The experiment is controlled by a Labview program. As has been

discussed in Chapter 1, the measured perpendicular component of the reflected power is subtracted from the measured parallel component to obtain the pure signal due to the surface reflection. This signal is then normalized to its initial value before applying strain.

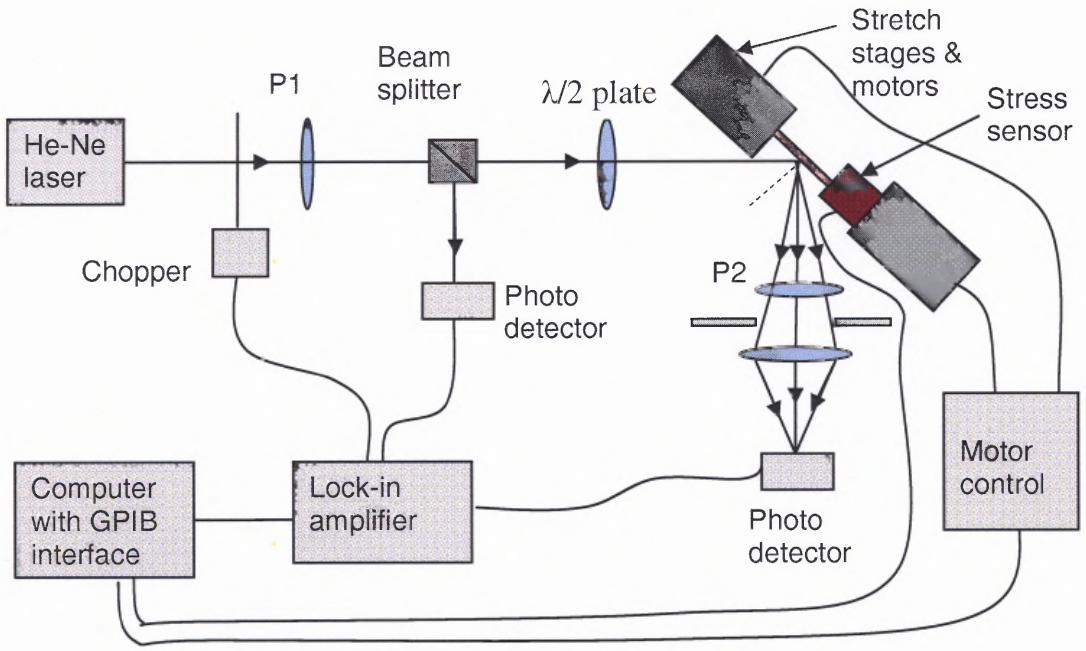

Figure 3.1 Schematic experiemental setup with bulk optic components. In the experiements, the polarization orientation of the incident light is perpendiculer to the direction of the stretch and parallel to the sample surface (or simply called TE incident mode). The incident angle is about 57 degrees, corresponding to the Brewster angle[6] of the material.

The normalized optical signal is also called normalized reflectivity in this report. The data measured on the latex materials shows that the normalized reflectivity increases linearly with the increasing stretch. The results from a 80mm long, 30mm wide polyvinyl sample demonstrated the linear relation between the normalized reflectivity and the stretch within about 25% ($\frac{\Delta L}{L_0}$) strain. No saturation is observed. The result is in agreement with the data obtained previously[6,7], and is shown in Figure 3.2. The linear fit

of the normalized reflectivity shows a correlation coefficient of 0.986 and reflectivity-strain slope of 1.23. The reflected optical power of the parallel component also increases with the strain, but the perpendicular component does not show an obvious trend to increase or decrease with the strain.

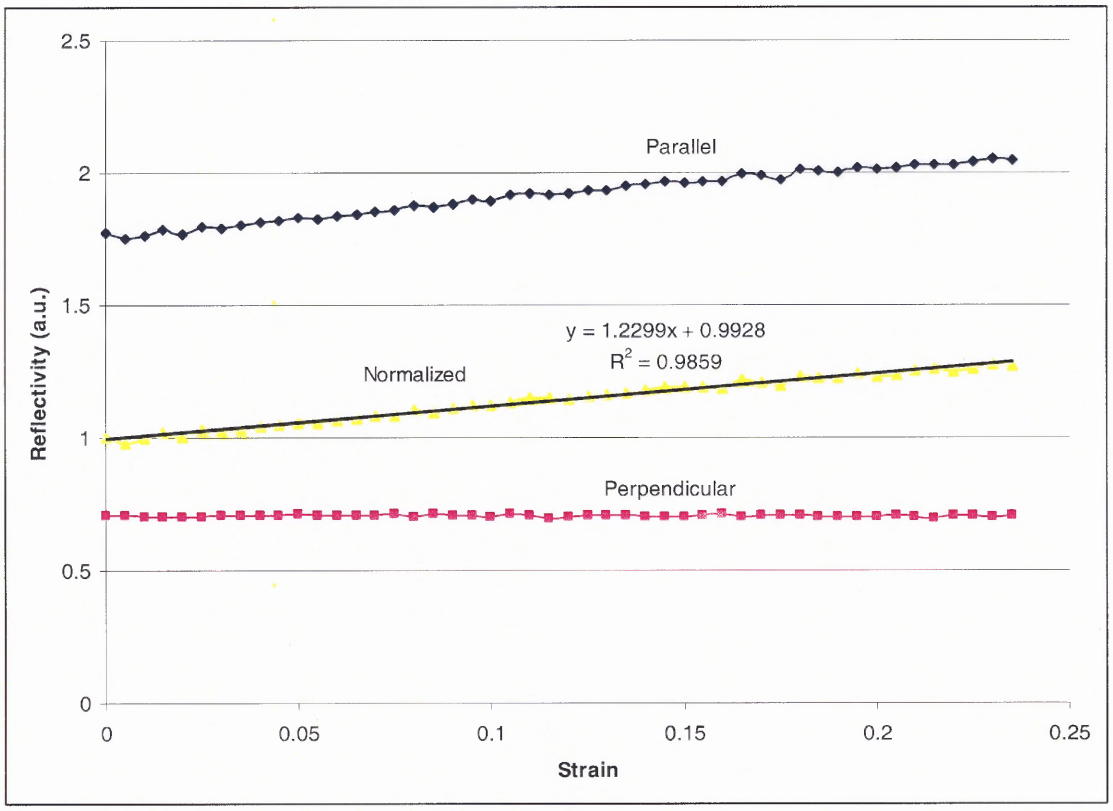

Figure 3.2 Reflectivity as a function of the strain ($\frac{\Delta L}{L_0}$) for the polyvinyl sample.

In order to affirm the validity of the test results and to investigate the elasticity of the material, two samples were made from the same polyvinyl material and cut to the same width yet with different lengths. These samples can be viewed as simple springs of different initial lengths. From the simple model of elasticity, the tension in the latex

samples for small stretches can be expressed as $F = \frac{YA}{L_0}\Delta L$, where Y is the Young's modulus, A and L_0 are the area of cross section and the sample initial length respectively, ΔL is the stretch length. Defining $k = \frac{YA}{L_0}$ as the spring constant, such that k represents the slope of the stress vs. stretch curve, one gets $F = k\Delta L$. Clearly, k is proportional to L_0^{-1}.

In the experiment, one sample was cut to be 78mm long; the other one was 50mm long. For the 78mm long sample, the slope of the reflectivity vs. stretch curve is about 2/3 ($\frac{1.5217}{2.2925}$ =0.66) of that of the 50mm long sample (Figure 3.3 (a)). This result is consistent with the theoretical expectation, since one expects the ratio of the added length to the original length determines the normalized reflectivity. In the experiments, the applied stress was also measured as a function of the stretch, and a nearly linear relation between the stress and the stretch was obtained for strain less than 30%, due to the high resilience of the latex material. From this simple model, the ratio of the slope of the stress vs. stretch plot of the 78mm long sample to that of the 50mm long sample should be $\frac{50}{78}$=0.641. Experimentally, for the 78mm long sample, the slope of the stress vs. stretch curve was $\frac{0.4267}{0.6376}$=0.669 of that of the 50mm long sample (see Figure 3.3 (b)). The stress vs. strain plots and the normalized reflectivity vs. strain plots for the two samples are shown in Figure 3.4, the traces of the regression lines are essentially overlapped for the two samples. These results agree with the model predicted value.

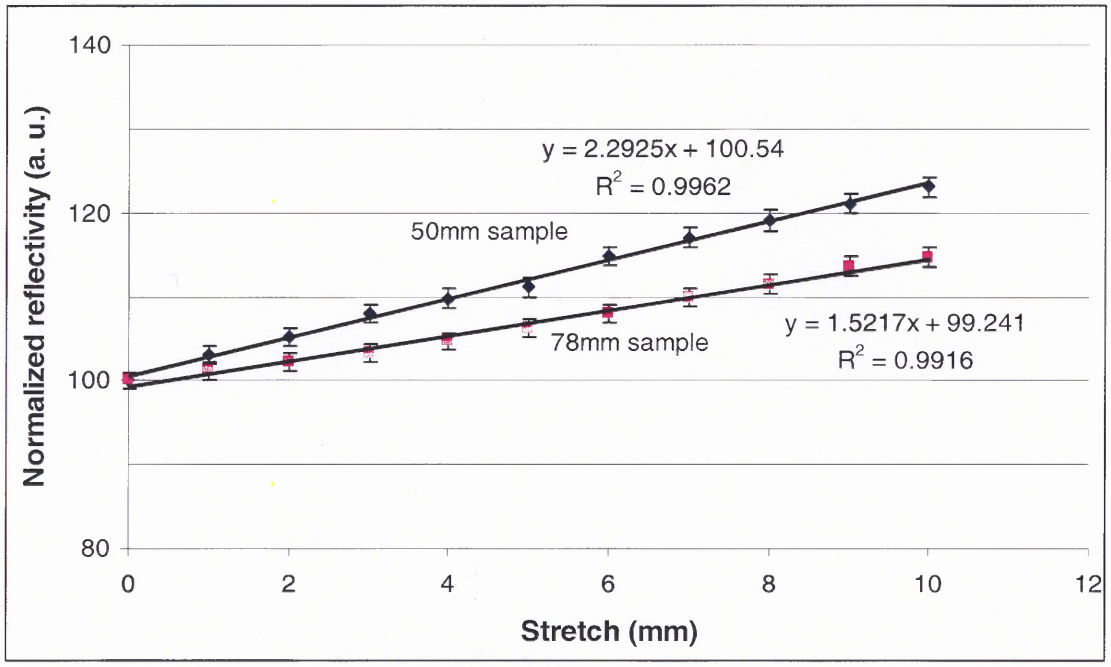

(a)

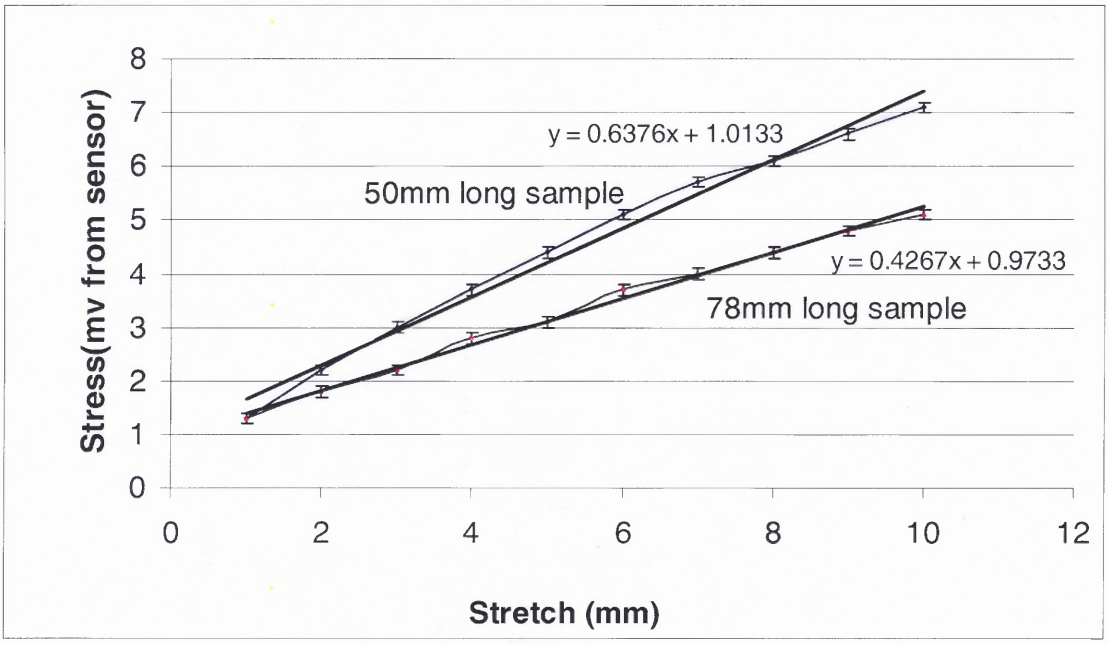

(b)

Figure 3.3 Normalized reflectivity vs. stretch (a) and stress vs. stretch (b) for the 50mm and 78mm long samples (error bar: (a) ±5%; (b) 0.2mv).

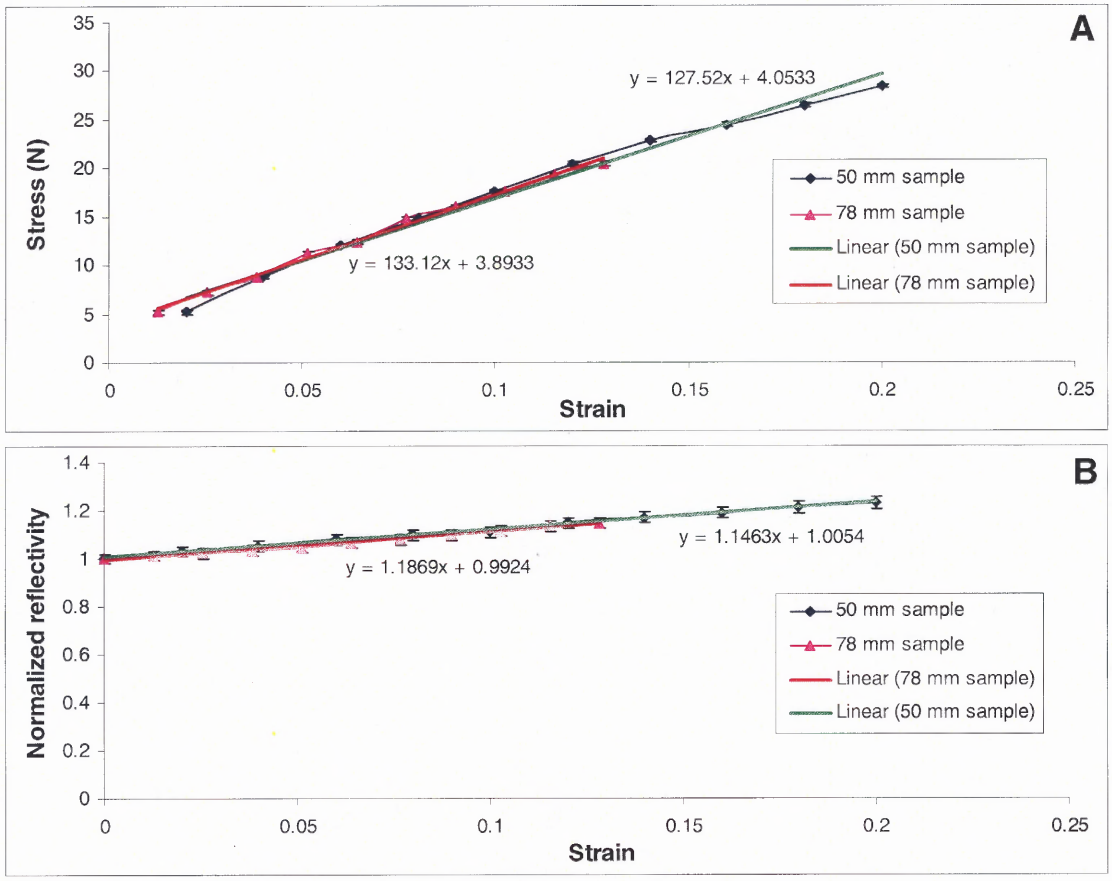

Figure 3.4 Stress as a function of strain (A), Normalized reflectivity as a function of strain (B). The slopes of the plots for the two samples are close.

Based on the results from the experiments on the bulk optics system, the fiber system will employ the same methodology, thus it is reasonable to conclude that this fiber system is conceptually feasible. The implementation of the system consists of two phases: 1) Fiber optic system working on flat soft surfaces such as stretchable plastic or latex materials, or where the curve radius of the surface is much bigger than the light spot size, and 2) Expand the system to work on the curved surfaces such as surface of an inflated balloon, piece of stretched plastic. This will serve as a model for small body cavities and inner surface of blood vessels, where the surface curvature can not be neglected.

3.2 Experiments on Fiber Optic Components

3.2.1 Design and Fabrication of the Polarizing Fiber Probe

Possible fiber probe configurations should include two major types: fiber bundles and discrete fibers. If imaging through the system is not desired, there would be no obvious advantage for fiber bundle configurations, since the function of a fiber bundle can always be achieved by a single fiber in this application except that a fiber bundle can provide more uniform illuminations. However, fiber bundles usually have larger sizes and the fabrication of the probe becomes more difficult. In this work, discrete fiber configuration will be selected due to its simplicity in the fabrication process of the fiber probes.

For the discrete fiber configurations, two different incidence cases were considered: normal incidence and oblique incidence. As discussed in the bulk optic configuration, the optimized incidence angle is roughly the Brewster angle of the sample, this configuration in fiber optic system has drawbacks in the applications. Because the receiving fiber has to be oriented in the specular reflection direction, once the fiber probe has been fabricated, the probe to sample distance in an application also becomes a fixed value (Figure 3.5), consequently, alignment issues in the sensor positioning become critical.

Although it is easy to attach a small glass slide in front of the probe to fix the probe to sample distance, the physical contact between the glass and the tissue sample would inevitably change the local surface morphology of the sample.

For above considerations, the normal incidence configuration was selected, which will not be subject to the strict positioning set by the probe-to-sample distance. Moreover, the fabrication of this type of probe is easier, since all the fiber facets lie in the same plain,

which facilitates the attachment of polarizing filters. Another great advantage is that the sample to probe distance for this type is flexible within the range of several millimeters, which is necessary in the experiments.

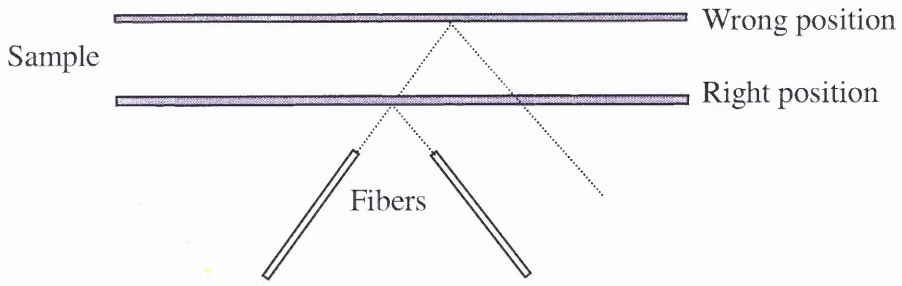

Figure 3.5 Positioning of the fiber probe for oblique incidence. Once the fiber probe has been fabricated, the probe to sample distance in an application must be fixed, hence lacks flexibility of positioning.

It is important to consider the question of which configuration is more suitable: a two-fiber configuration or a three-fiber configuration? In the two-fiber configuration, one fiber works as incident fiber and parallel receiving fiber simultaneously, the other fiber plays the role of perpendicular receiving fiber. The schematic of this configuration is illustrated in Figure 3.6.

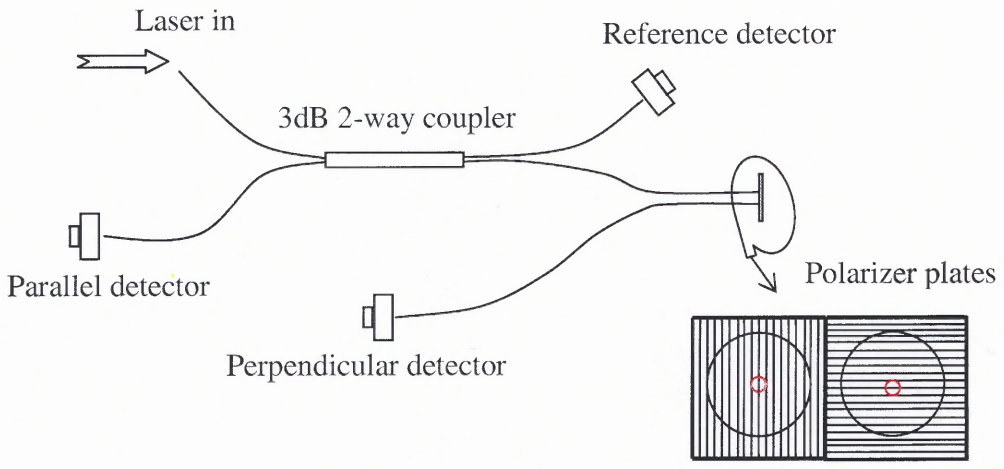

Figure 3.6 Two-fiber configuration of the polarizing fiber probe.

The advantage of this structure is that the receiving fiber is rigorously orientated in the specular reflection direction. However, the 3dB 2-way couplers are not always commercially available for different fiber specifications, and the in-house fabrication of the coupler is not readily feasible and cost effective. The three-fiber configuration (Figure 3.7) will be used in the entire experiment.

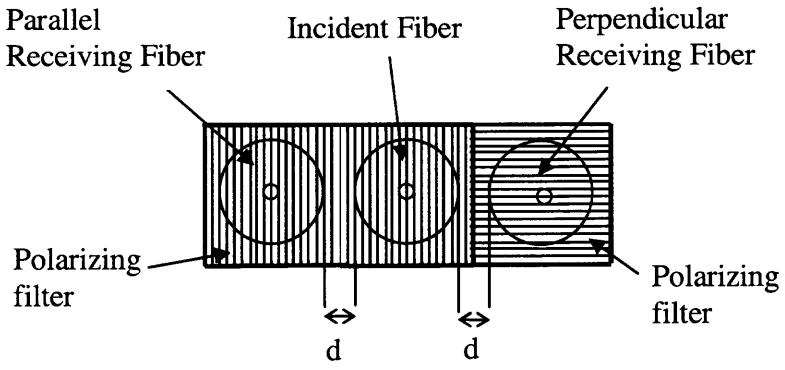

Figure 3.7 Three-fiber configuration of the fiber probe.

Comparing with the two-fiber configuration, this three-fiber structure eliminates the need for a fiber splitter, however, at the sacrifice of non rigorous specular detection. For small diameter fibers, the deviation from the specular reflection direction is negligible as long as the probe to sample distance is much longer than the fiber diameter, which is truly the case in most applications. In the following paragraph, the detailed fabrication process of the fiber probe is discussed.

Three fiber probes were fabricated using identical fibers in each probe as incident fiber and receiving fiber. For fabrication convenience, only one fiber probe was made with different fibers for incidence and detection. Although a smaller fiber diameter and NA is desirable for the incident fiber for better beam quality, and a larger diameter fiber is better for detection, the probe with identical fibers does not lose the generality of the

characteristics of a fiber optic configuration compared with the bulk optic system. However, this consideration is necessary when the system design is to be optimized.

Procedure of the Fiber Probe Fabrication:

First, two pieces of glass sides (1mm in thickness) are cut approximately 3 X 15mm and roughly polished for the edges. Then very shallow V-trenches are created in one top surface of one slide, the separation of the trenches determines the separation of the fibers in the array. Designated fibers are sandwiched in an array between the glass slides with each fiber sitting in the corresponding trench. UV curable epoxy is then filled in the empty spaces between the fibers and the glass slides. It is important to hold the assembly tightly and maintain the desired shape. With UV light applied, the epoxy can be cured in a very short time period, which ranges from seconds to minutes depending on the power of the UV light source. Sometimes, it is desired to wait several hours or a day to let the epoxy fully cure at room temperature. The assembly is a solid unit and ready for a fine polishing of the fiber ends. Thorlabs fiber polishing tool kits are used for this process.

After the polishing, the assembly is put under a microscope for inspections. The actual fiber separations are measured at this step, because it is common that the fiber separations deviate several microns from the designed distances due to the processing errors. It would be a great improvement, if the v-trenches are created by lithography on a silicon substrate, since the scaling is more accurate. The top cover sheet still can be glass, through which UV light can pass and reach the epoxy in the spaces between the fibers and the substrates. The fiber assembly of the probe is shown in Figure 3.8.

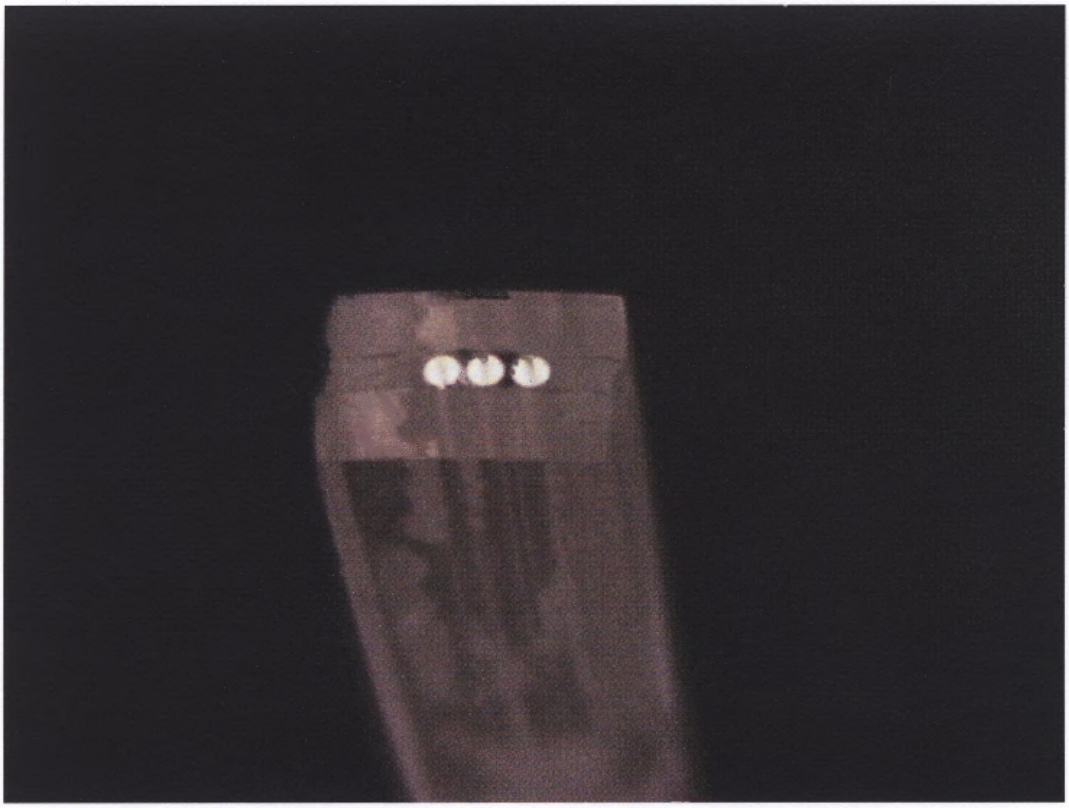

Figure 3.8 Fiber array is sandwiched between two glass slides.

Second, two polarizing filters are glued on the end of the fiber assembly. The two polarizers with orthogonal orientations are cut to about 1.2 X 1.5mm in size (exact size depends on the fiber diameter) with thickness of 0.7mm. The attachment of the polarizers to the end of the fiber array is performed under a microscope. With the help of a tiny tip, the position of the polarizer can be manipulated, such that the designated fiber ends are covered by the polarizer with the desired orientation. The Norland 68 UV adhesive is applied between the polarizer and the fiber facets and cured by a UV curing kit. The adhesive has an optical index which matches the index of the material of fibers, thus reducing the Fresnel reflections from the incident fiber facet. The detector head with polarizers attached is shown in the following Figure 3.9.

Figure 3.9 Polarizing filters with orthogonal polarization orientations are glued to the probe ends. The central fiber is the incident fiber, and together with the parallel receiving fiber is covered by the same polarizing plate.

The last step is the fabricated fiber probe is pigtailed with fiber connectors, which makes the launching of laser light into the fiber and the wiring of reflected optical signal easier. A fully packaged polarizing fiber probe is shown in the following figure (Figure 3.10), the fiber probe is a colorless rectangle, the incident fiber connector is blue, and the two connectors of receiving fibers are black. Note that in this system, no miniature fiber lenses are used. These dimensions of the probe are about 2mm (thickness) X 3mm (width) X 10mm (length), and these dimensions can be substantially reduced if the fiber diameter is small enough.

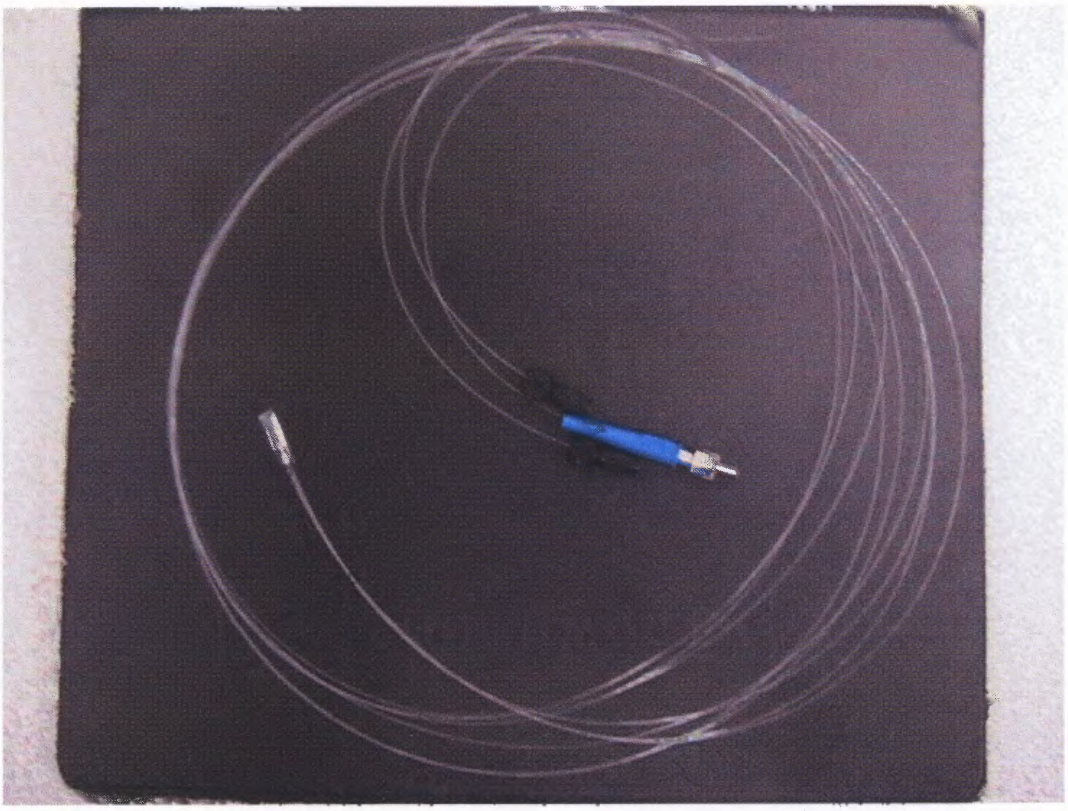

Figure 3.10 A fully fabricated sensor with fiber pigtails. The dimension of the probe head is about 2×3×10mm.

Four polarizing fiber probes with different fiber specifications were fabricated using the procedure discussed above. The specifications of the probes are shown in the following Table 3.1. The fiber diameter columns show core/cladding values. The separation value (left/right) is the gap between two adjacent fibers (see Figure 3.6).

Table 3.1 Fiber Probe Configurations

Probe #	Incident fiber diameter (core/cladding)	Receiving fiber diameter (core/cladding)	Incident fiber NA.	Receiving fiber NA.	Separation between fibers (left/right)
1	100/140μm	200/220μm	0.3	0.22	120/135μm
2	200/220μm	200/220μm	0.22	0.22	130/120μm
3	486/500μm	486/500μm	0.51	0.51	140/125μm
4	735/750μm	735/750μm	0.51	0.51	135/130μm

3.2.2 Experiments on Flat Surface with Fiber Optic Components

The schematic of the system is shown in Figure 3.11. The He-Ne laser beam with wavelength around 633nm is directed through a mechanical chopper and the beam splitter, and then coupled into the incident fiber of the probe via the fiber coupling optics, so that phase sensitive detection can be employed. Detector D1 measures the reference power. Detectors D2 and D3 measure the parallel component and perpendicular component power of the reflected light respectively. Note that no miniature fiber lenses are used at the ends of the light collecting fibers, because the fiber probe is very close to the sample surface (several millimeters) such that enough light can be directly coupled into the receiving fibers (multimode, large NA.). The fiber probe is oriented in the normal direction of the flat surface, and the flat sample is mounted on a computer controllable translation stage.

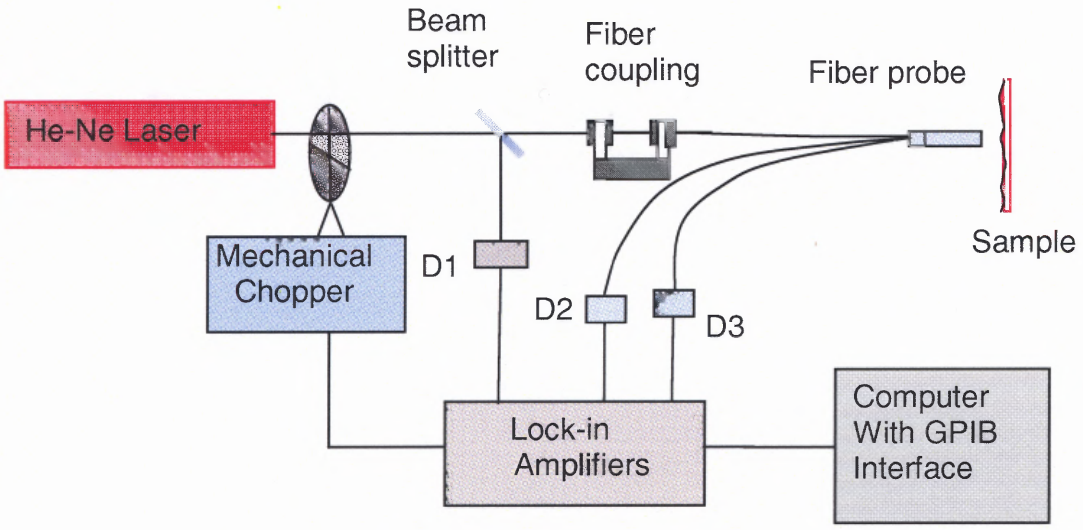

Figure 3.11 Experimental setup for flat rough surfaces.

All the fabricated fiber probes are employed in the experiment at different probe to sample distances. Since the receiving fibers are not strictly oriented in the specular

reflection direction, it is expected that the probe to sample distance is a factor that may affect the measured slope of the linearity between the normalized reflectivity and the strain. The experiment is controlled by a Labview program. Before the stretching of the sample, the background signals in the two fiber channels were measured by illuminating a void target, since the UV epoxy and the polarizing filters on the probe ends scatter or reflect a portion of the light from the incident fiber that might be partially coupled into the receiving fibers. Removal of these signals in each channel will yield pure reflected optical signals from the sample only.

3.2.3. Fiber Optic Components with Curved Surfaces

The fiber optic probe is expected to have applications in measuring the strain (stress) of the human tissue *in vivo*. An application example is schematically drawn in (a) of Figure 3.11. It has to be accommodated to the complex application environment, which requires it to work on curved surfaces. The experiment needs to determine the curvature range of the surface for which validity of the linear relation between the normalized reflectivity and the strain holds. The mathematic formulation in the previous Chapter anticipates that as long as the surface curvature radius is much larger than the probe to sample distance, the linear relationship between the normalized reflectivity and the strain holds. In the experiment, each configuration of fiber probe is used at different probe to sample distances.

The experiment setup for the curved surface can be designed as shown in (b) of Figure 3.12. The setup is under a microscope (not shown in the figure), so that relative positions of the cantilever to the probe and the curved surface can be monitored clearly. The fiber probe is mounted on a translation stage with positioning accuracy of 10μm, and

can translate back and forth toward the curved surface. The cantilever mounted on another translation stage is used to measure the position of the apex of the surface when the air pressure is applied and the surface expands outward, such that the fixed probe to sample distance can be maintained during the experiment. The air chamber has a circular opening with a diameter of 25.4mm, a naturally flat latex sheet, same as the samples used in flat surface experiments, is sealed on the circular opening.

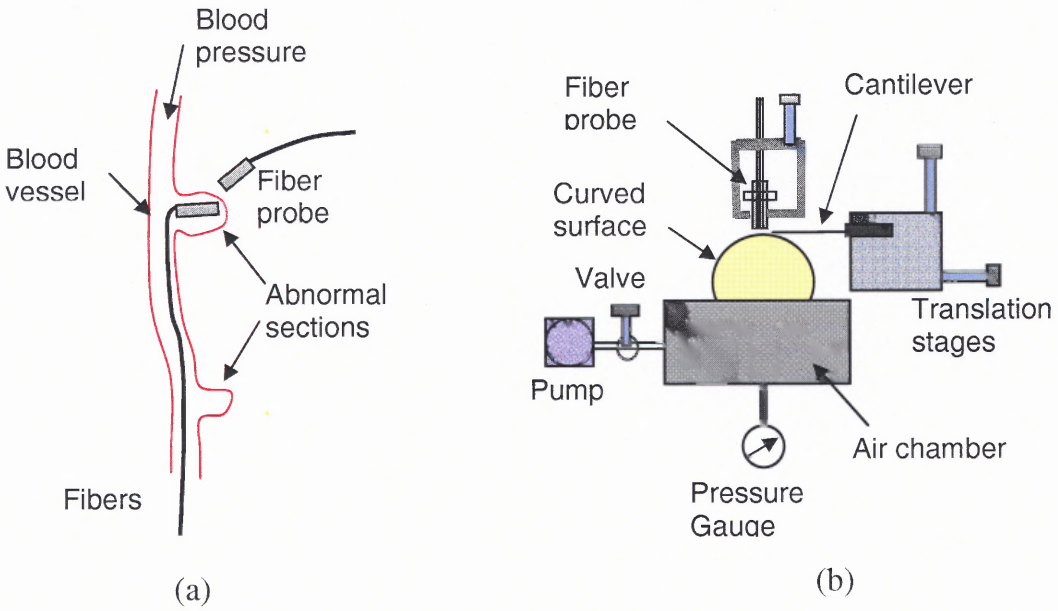

Figure 3.12 Curved surface cases: (a) schematic of application, (b) experimental setup

Two points are addressed here: First, since the opening of the air chamber is circular, the sample surface would become a sphere if air pressure is applied in the chamber. As the surface swells, the curvature of the surface continually changes. Second, because the stretching of the surface is isotropic in this experiment design, the strain in the sample is no longer in only one direction, the surface ripple vector in orthogonal

directions may introduce more dramatic roughness change of the sample compared with the flat surface case.

Due to above considerations, the relationship between the normalized reflectivity and strain in this experiment setup will be modified by the changing curvature of the surface. However, if the rough surface (especially human tissues) has patterned roughness instead of random one, or one of the surface ripple vector dominates the surface corrugation (which is true in the selection of the sample in the experiment), the strain in the orthogonal direction to the ripple vector would not introduce much reflectivity change during the stretch. At this condition, only the strain in one particular direction is considered, and the sphere surface under the illumination can be approximated by a cylinder surface which has a curvature radius equal to the radius of the sphere.

CHAPTER 4

DATA ANALYSIS AND SYSTEM OPTIMIZATION

The experimental results are collectively discussed in this chapter for each fiber probe configuration and probe to sample distance. The normalized reflectivity vs. strain plots are obtained, and the slopes of the linearity between the normalized reflectivity and the strain for different probe configurations are presented. As discussed in Chapter 1, the perpendicular component of the diffusively reflected light is treated as background noise, even though the perpendicular component could carry some useful information from deeper layers of the tissue sample. Thus the normalized reflectivity for the experiment is calculated as:

$$R_{Normalized}(S) = \frac{I_{Parallel}(S) - I_{Perpendicular}(S)}{I_{Parallel}(S=0) - I_{Perpendicular}(S=0)} \tag{4.1}$$

where I is the optical power, and S is the strain of the sample. Then linear regression line is employed to fit the $R_{Normalized}$ vs. S curve to obtain the slope.

4.1 Flat Surface Experimental and Simulation Results

The 0.2mm thick polyvinyl sample with initial length of 81mm (distance between two stretching stages) and width 28mm is used in the experiment. For the probe to sample distances ranging from 1mm to 6mm, the measured parallel, perpendicular, and normalized reflectivity are measured with a maximum strain of 23% using the four probes discussed in Chapter 3. The details of the obtained data are illustrated in the following paragraphs.

4.1.1 Experimental Data

Figure 4.1 shows the results obtained with Probe 2 (specifications are listed in Table 3.1) at 1mm fiber to sample distance. The two lower traces are plots for the reflectivity of parallel and perpendicular components as labeled respectively. The normalized reflectivity is calculated using Equation (4.1) and is shown with the top trace in the figure. A linear regression line is employed to fit the curve, indicating that the normalized reflectivity is linearly related to the strain in the sample with a slope 0.9 and a linear correlation coefficient 0.93. It is also shown that the parallel component of the reflected light is linearly related to the strain in the sample. However, the perpendicular component yields no appreciable change during the stretch.

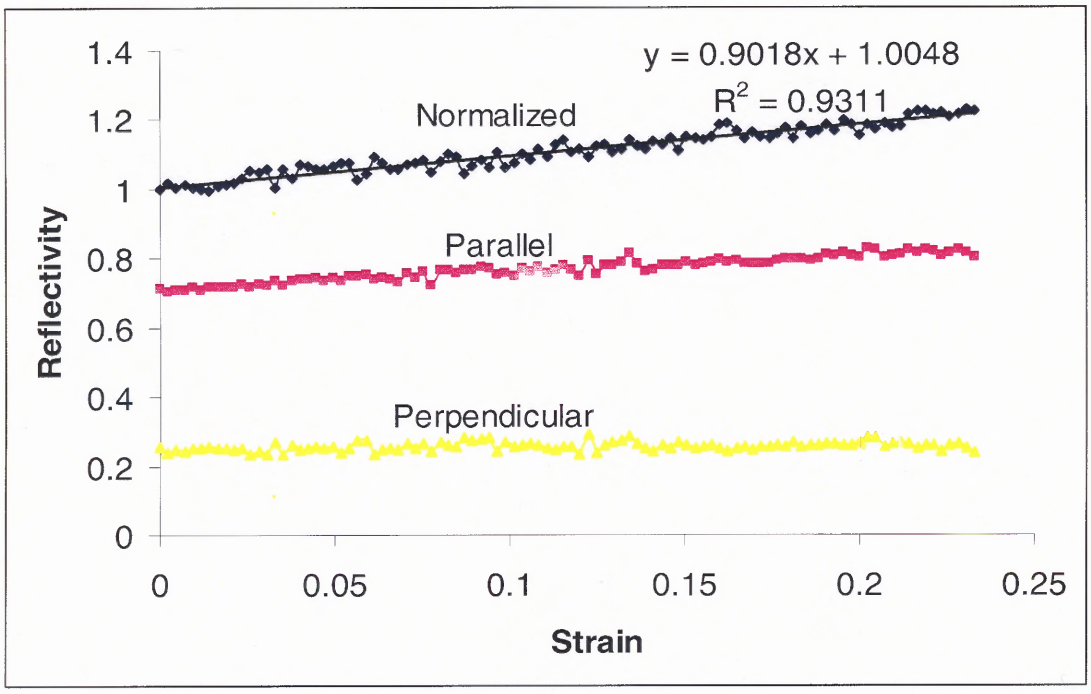

Figure 4.1 Reflectivity measured using Probe 2 at 1mm probe to sample distance.

Due to the geometric effects, as the probing distance changes, it is expected that the behavior of the measured reflectivity will change accordingly, however it may be

very small. With a 2mm probing distance, the same measurement is repeated on Probe 2, and the regression lines are drawn for the three plots in Figure 4.2. As expected, all the linear relationships still hold in this case. It is noticed that the slope of the normalized reflectivity is 0.97, which is slightly higher than 0.9 in the 1mm probing case. Another new phenomenon is that the perpendicular component of the reflected light slightly decreases with the increase of the strain. While these two effects are not prominent enough to be out of the error range of the experiment or plot fittings, one may suspect that a trend for the behavior of the measured reflectivity may exist as the probing distance changes. This conjecture is proved to be true by later experiments, in which more data is obtained by varying the probe to sample distance.

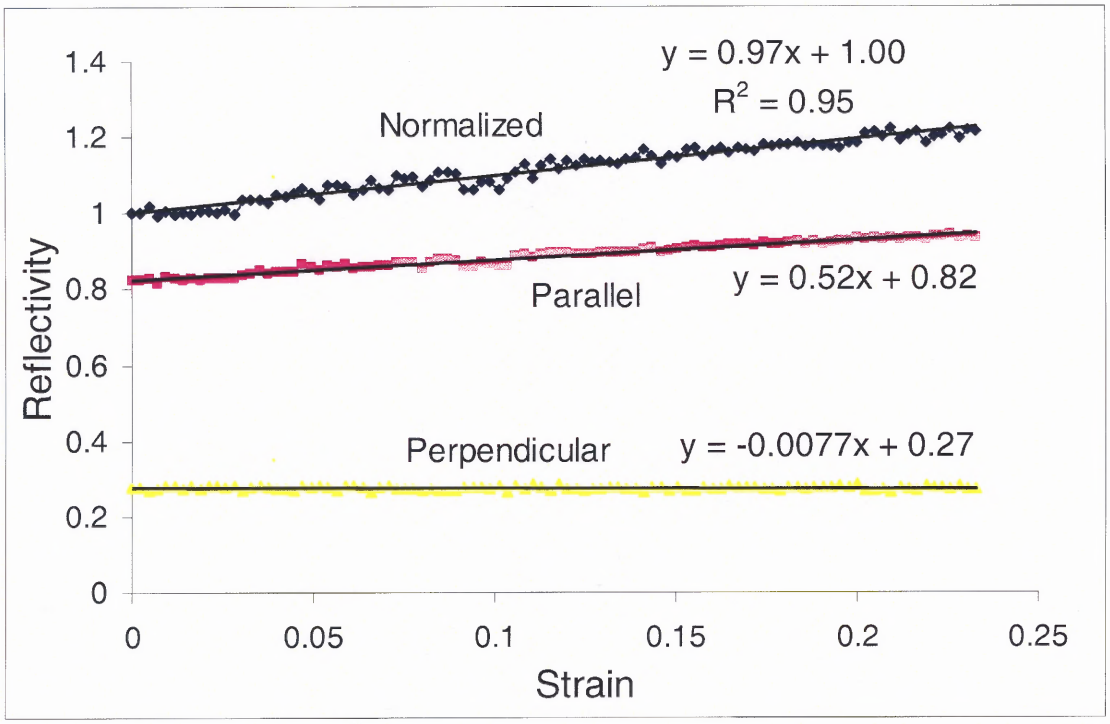

Figure 4.2 At 2mm probe to sample distance, results obtained with Probe 2.

With probing distance changing from 3mm to 6mm, more reflectivity vs. strain plots are obtained still using Probe 2. Figure 4.3 shows the results for the 3mm probing distance. Other plots (not shown) with distances of 4mm, 5mm, and 6mm exhibit common features. All of these plots show that the perpendicular component of the reflected light decreases slowly as the strain in the sample increases. However, analysis indicates that the slope of the normalized reflectivity does not increase monotonically with the probing distance. Instead, it first increases until at about 3mm reaching its maximum value 1.06, then the slope drops with the increase of probing distance.

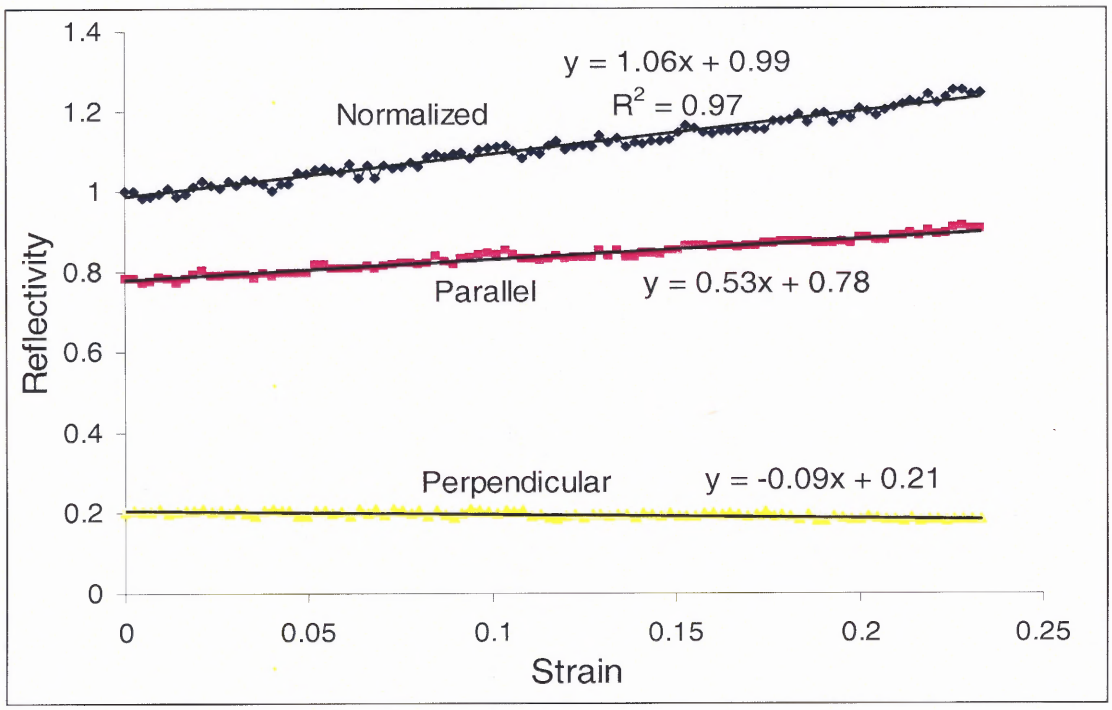

Figure 4.3 Reflectivity measured at probing distance 3mm with Probe 2.

It is also noticed that the linear correlation coefficient varies with the probing distance too, indicating that an optimum probing position may exist. To summarize the results obtained with Probe 2, Table 4.1 lists the key information of interest.

Table 4.1 Slopes and Linear Correlation Coefficients for Probe 2

Probing distance(mm)	1	2	3	4	5	6
Slope	0.90	0.97	1.06	0.95	0.85	0.81
Linear correlation coefficient (R^2)	0.93	0.95	0.97	0.93	0.93	0.83

To verify the above results obtained with Probe 2, other probe configurations (Table 3.1) are employed to repeat the experiment. By analysis of the data, similar results are obtained for these configurations. The normalized reflectivity vs. strain slopes and the linear correlation coefficients for all the fiber probes at different probing distances are listed in Table 4.2. The data is obtained from the same polyvinyl sample.

Table 4.2 Slopes and Linear Correlation Coefficients for All Probes at Different Probing Distances

Probe #	Probe to sample distance (mm)											
	1		2		3		4		5		6	
	Slope	(R^2)	Slope	(R^2)	Slope	(R^2)	Slope	(R^2)	Slope	(R^2)	Slope	(R^2)
1	0.91	0.95	0.98	0.91	1.07	0.98	0.98	0.95	0.87	0.92	0.81	0.80
2	0.90	0.93	0.97	0.95	1.06	0.97	0.95	0.93	0.85	0.93	0.81	0.83
3	0.89	0.93	0.94	0.94	1.08	0.94	1.00	0.98	0.91	0.96	0.80	0.92
4	0.67	0.92	0.88	0.92	0.94	0.96	1.04	0.97	0.96	0.96	0.89	0.92

4.1.2 Data Summation

The extracted data in Table 4.2 together with the plots obtained from the measured data with all fiber configurations indicate several common characteristics of the fiber probes:

1. The normalized reflectivity linearly increases with the strain of the sample; the measured reflectivity of parallel component is roughly proportional to the strain of the sample; the measured power of perpendicular component decreases as the strain increases.

2. Considering the intrinsic errors introduced by the fabrication of the probes (such as deviation from specular reflection direction of the receiving fiber due to physical presence of the fibers and necessary separations between them), for a fixed probing distance between 3 and 4mm, the slope of the linearity is not very sensitive to the probe configuration for fiber core diameters ranging from 100μm (Probe 1) to about 735μm (Probe 4) and numerical aperture ranging from 0.22 (Probe 2) to 0.51 (Probe 3, 4). For shorter (≤2mm) and longer (≥5mm) probing distances, there is significant deviation in the measured slope only for Probe 4, which has the largest fiber core diameter (735μm) and N.A. value (0.51).

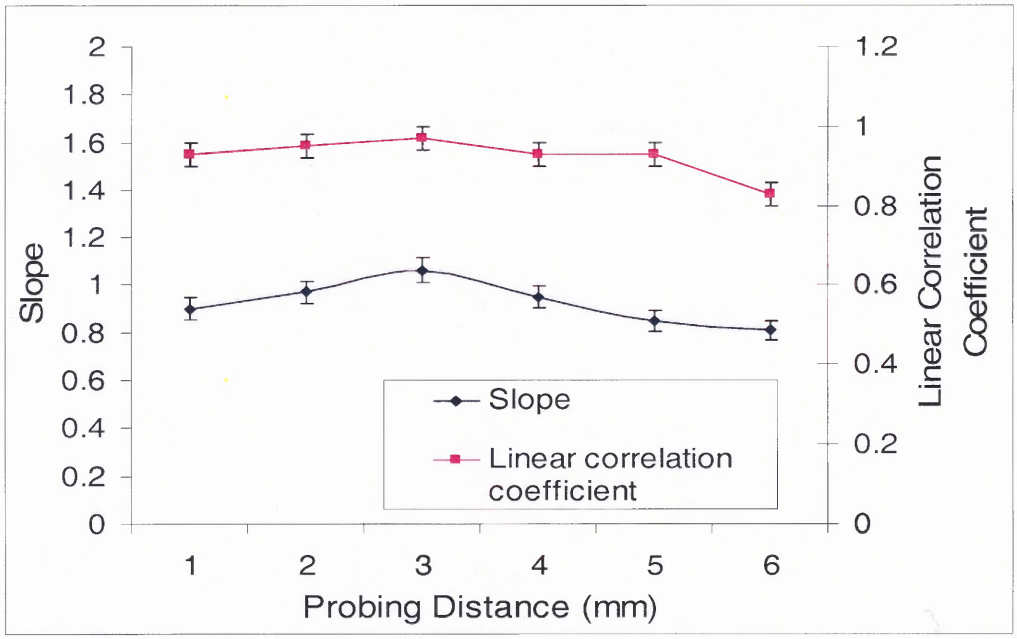

Figure 4.4 Slope and linear correlation coefficient extracted from the linear fitting between the normalized reflectivity and strain as a function of the probing distance.

3. The maximum slope and optimized linearity can be achieved by varying the probing distance. The maximum slope is slightly above 1.0 at optimum position for all the probes. At other probing distances, the slope is less than 1.0. From the data for Probe 2 in Table 4.1, the slope and R^2 vs. probing distance curves are readily obtained in Figure 4.4. The other probes show the similar pattern as expected from the data in Table 4.2.

4. Most of the data (Figure 4.1 through Figure 4.3) has higher noise level compared with data obtained with bulk optic configurations (Figure 3.2), and the perpendicular component of the reflected decreases slightly as the strain increases.

While the first and second characteristics are in good agreement with the prediction of the theoretical analysis, the third one greatly deviates from the theory developed in Chapter 2, which predicts that the slope should be not less than 1 for any surface with sinusoidal roughness pattern.

4.1.3 Simulation Comparison

To compare this fiber experimental result with the theoretical analysis, the numerical result of a sinusoidal flat surface with roughness 4.0 (this roughness value is estimated from the bulk optics experiments which show a slope of about 1.3 corresponding to a roughness parameter Ag=4 in the theoretical analysis.) using Probe 2 parameters at probing distance 3mm is shown in Figure 4.5. With the tracing of 50,000 rays uniformly distributed in the incident light cone, the rays that finally propagate out from the remote end of the receiving fiber are counted using a virtual screen for each stretch step. The counted ray numbers (proportional to the normalized reflectivity) are then plot against the strain of the sample. Fairly good linearity between the normalized reflectivity (due to the algorithm, perpendicular component is eliminated automatically) and the strain is obtained. As a comparison, the experimental data is also plotted in the same figure. The slope and the linear correlation coefficient (R^2) for different probing distance are shown in Table 4.3.

Table 4.3 Numerical Result of the Slope and Linear Correlation Coefficient of Probe 2 for Different Probing Distances

Probing distance					
1mm		3mm		5mm	
Slope	(R^2)	Slope	(R^2)	Slope	(R^2)
1.25	0.98	1.27	0.99	1.31	0.99

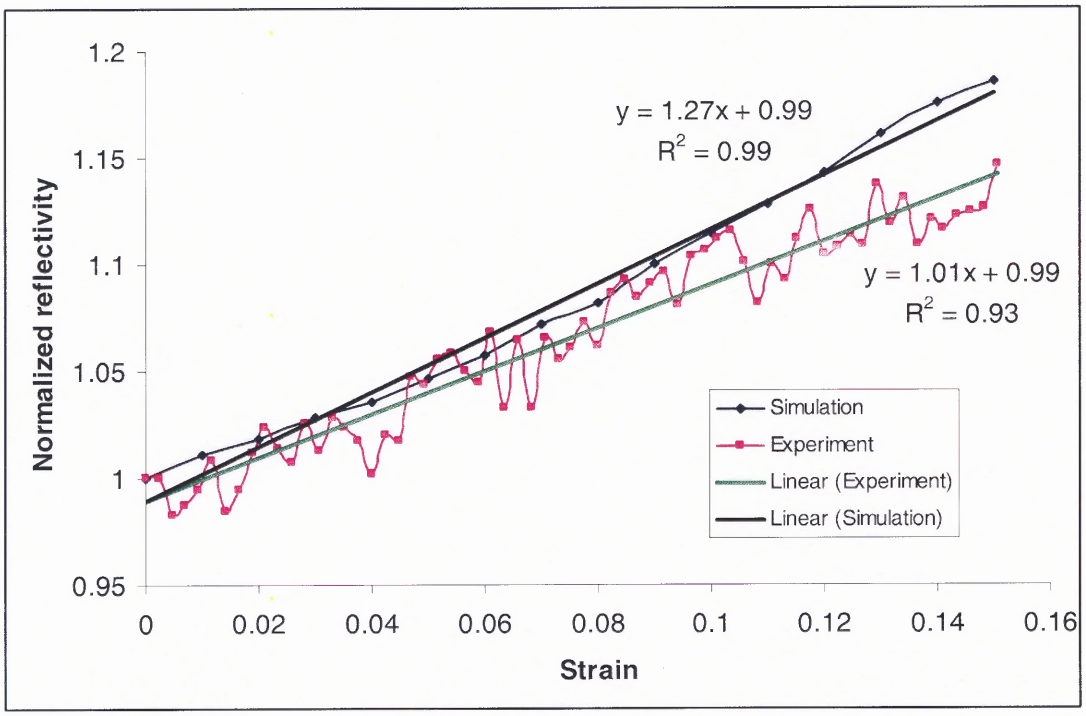

Figure 4.5 Simulation and experimental results of Probe 2 at 3mm probe-to-sample distance with maximum strain of 15%.

To summarize, the simulated and the experimental slopes of the four probes at 1mm, 3mm, and 5mm probing distances are listed in Table 4.4. The slopes extracted from the experimental data have the standard errors ranging from ± 0.03 to ± 0.06, and for simulation data, this value is only about ± 0.01.

Table 4.4 Comparison between Slopes Obtained from Simulations and Experiments

Probe #	Probe-to-sample distance (mm)					
	1		3		5	
	Sim Slope	Exp Slope	Sim Slope	Exp Slope	Sim Slope	Exp Slope
1	1.27	0.91	1.28	1.07	1.28	0.87
2	1.25	0.90	1.27	1.06	1.31	0.85
3	1.22	0.89	1.26	1.08	1.27	0.91
4	1.07	0.67	1.13	0.94	1.27	0.96

Clearly enough, in Table 4.4 most of the simulation results suggest a lope of about 1.28, and is higher than the experimental result, which is close to 1.0. The simulation and experimental results reveal the similar trend of the slope variation under different fiber configurations, although the absolute values of the slope are different. This trend can be more intuitively presented in Figure 4.6.

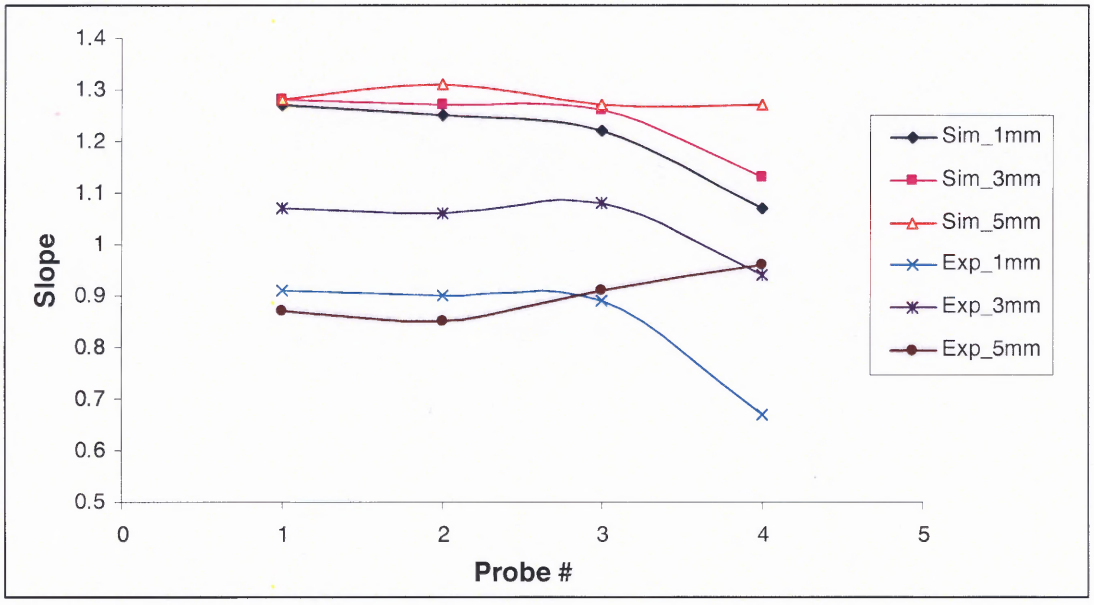

Figure 4.6 Simulation and experimental slopes vs. Probe # for different probing distances.

4.1.4 Discussion

Simulation results in Figure 4.5 and Table 4.3 show that linearity between the normalized reflectivity and the strain is still maintained with incident beam divergence of 0.22 (NA. of incident fiber) and strain less than 15 percent for different probing distances, which is in good agreement with theoretical estimation in Chapter 2. The experimental discrepancies (the third characteristic in Section 4.1.2, in which the slope is less than 1) compared with numerical results and the prediction of theory may come from the following factors:

- Surface modeling errors: The assumed sinusoidal surface roughness and non-stretchable surface path length may not be strictly true for the polyvinyl glove sample, which could be the major cause of the slope values smaller than 1.

- Design geometry errors: The incident beam divergence, the light spot size at sample surface, the position deviation of the receiving fiber from specular reflection direction due to design and fabrication limit all introduce some systematic errors, but trends of one probe versus another are still valid.

These factors will be further discussed later (Chapter 5). As for the fourth characteristic, the excess noise could not come from the laser power and polarization hopping (which is equally present in bulk optic system). The lower input optical power level compared with bulk optic configuration, the divergence of the incident light beam, and possibly intrinsic properties of multimode fibers (so called "Modal Noise") are suspected to have major influences on the signal-to-noise ratio[48-51]. The decrease of the detected reflection power of the perpendicular component during the increasing of the strain may come from following reason: As the stretch increases, the thickness of the sample decreases, which reduces the scattering events as the photons migrate within the sample. Thus more photons simply transmit through the sample, and less photons are reflected back as unpolarized light, resulting in the decreased power of the perpendicular component.

4.1.5 Summary

Despite the above imperfections, the fiber probe as a substitute of the bulk optic system for stress/strain sensor maintains the good linearity between the normalized reflectivity and the strain. The experimental result in Table 4.2 and the simulation comparison data in Table 4.4 reveal that with fiber N.A. up to 0.51 and fiber core size up to 486μm, the slope of the linearity is fairly insensitive to the fiber configuration. With larger core size and

N.A. fiber, the slope is more sensitive to the probing distance, which is mainly due to the geometry errors of the configuration of the fiber probe.

4.2 Curved Surface Results

4.2.1 Description on Several Experimental Parameters

The same material sample is cut and mounted on an air chamber opening of the setup as shown in Figure 3.11 (b) in Chapter 3.

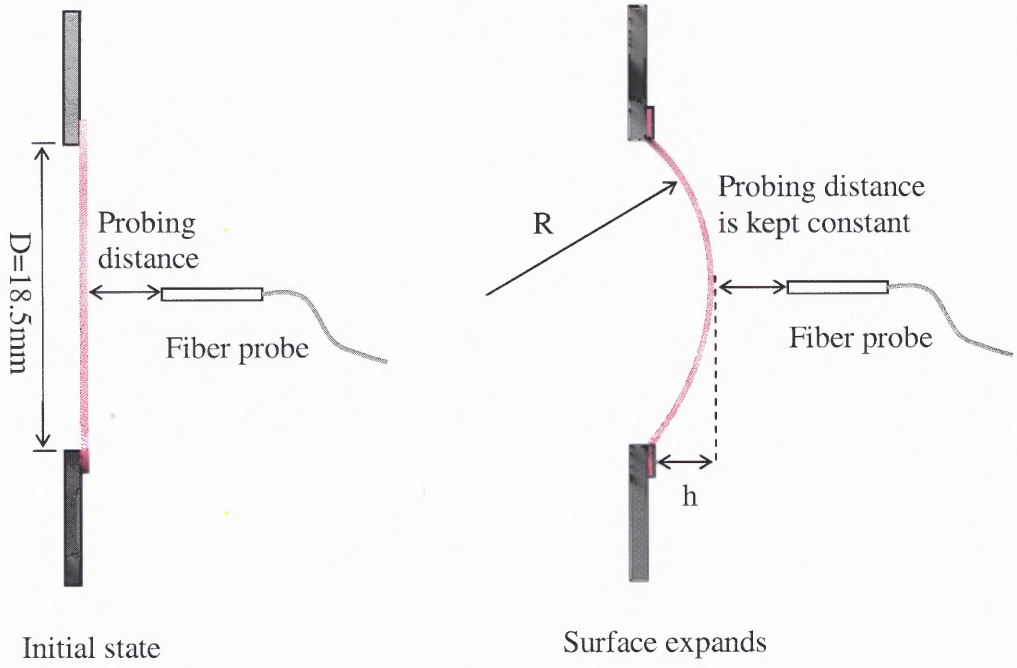

Figure 4.7 Surface swells after air pressure is applied, R is the radius of the sphere, D is the aperture of the opening, and h is the height of the partial sphere measured from the base of the mounting.

The sample is initially flat and its edge is sealed with glue on the chamber opening periphery. The diameter of the opening is measured to be 18.5mm. When air pressure is applied, the flat surface will swell out forming a partial sphere due to the flexibility of its nature, and the curvature of the surface increases. As discussed in the

previous chapter, under approximations, only the curvature and strain in one dimension is concerned. The sphere is effectively treated as a cylindrical surface, and the surface expanding direction is corresponding to the direction of the vector of sinusoidal ripples on the cylinder surface (see Figure 2.11). During the experiment, as the surface swells out (convex case), the probe adjusts its position to keep the probe to the surface vertex distance constant (see Figure 4.7). From the geometry, the radius of the sphere is readily obtained:

$$R = \frac{D^2 + 4h^2}{8h} \tag{4.2}$$

and the periphery length of the big arc after the expansion of the surface is:

$$L = 2R\arcsin(\frac{D}{2R}) \tag{4.3}$$

the one dimensional strain in concern is simply derived as:

$$S = \frac{L - L_0}{L_0} = \frac{L - D}{D} = \frac{2R\arcsin(\frac{D}{2R})}{D} - 1 \tag{4.4}$$

Substituting Equation (4.2) into Equation (4.4), one obtains:

$$S = \frac{\frac{D^2 + 4h^2}{4h}\arcsin(\frac{4Dh}{D^2 + 4h^2})}{D} - 1 \tag{4.5}$$

4.2.2 Material Elasticity Investigation

First, it is necessary to investigate the elasticity of the material used in this experiment, such that the relationship between the normalized reflectivity and the strain can be used to link the change of normalized reflectivity to the excess stress in the sample, and therefore extract the elastic properties of the sample.

From the Laplace's equation, the measured pressure P in the air chamber, the tension (N/m) T in the sample, and the curvature radius R are related by the simple equation:

$$\frac{2T}{R} = P \tag{4.6}$$

Since strain S is calculated through Equation (4.5), R is calculated through Equation (4.2), and pressure P is the direct measured quantity in the experiment. Thus a relationship between the strain S and the surface tension T (or PR) is established. Elasticity can be checked by plotting T (or PR) vs. S curve in Figure 4.8, which indicates that the linear relation is maintained for strain less than about 15%. It is straight forward to establish the relation between the normalized reflectivity and the applied surface tension with the help of the T vs. S curve for that particular material.

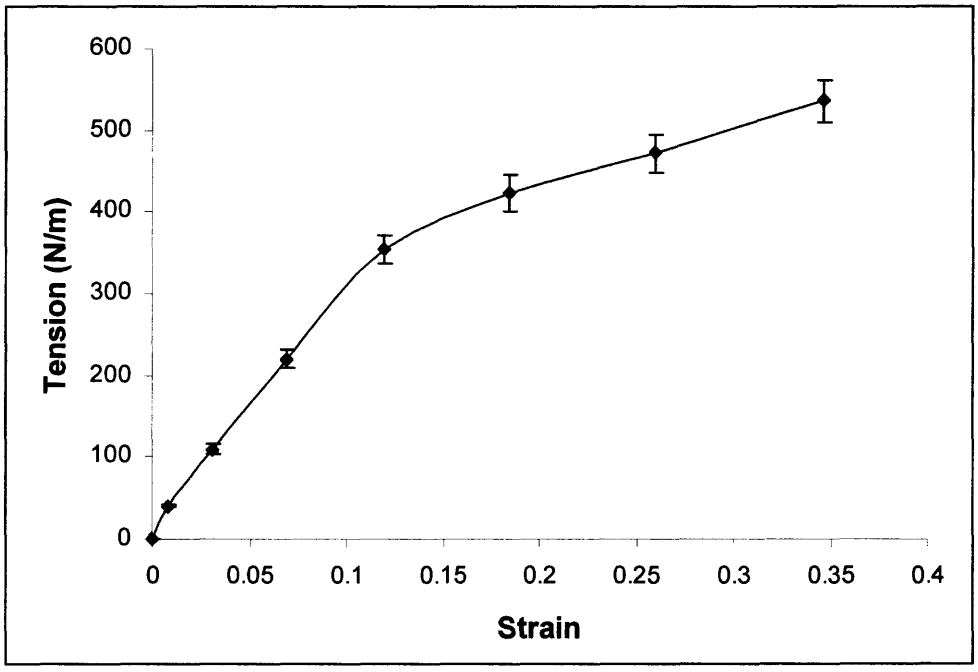

Figure 4.8 Elasticity of the sample material, the linear relation between the strain S and surface tension T (N/m) or PR is maintained for strain less than about 15%.

4.2.3 Experimental Results

The original data is measured according to different h values. With the help of Equation (4.5), the normalized reflectivity vs. strain curves can be plotted. For probing distances ranging from 1mm to 5mm, the normalized reflectivity vs. strain curves are obtained in the following figures.

Figure 4.9 shows the normalized reflectivity vs. strain plot for Probe 2 at 1mm probing distance. It is clear from the plot that the relationship between the normalized reflectivity and the strain is approximately linear for strain up to 35%, even though the curvature of the surface continuously changes during the expanding of the surface. Considering the linear range of the relation between the surface tension and the strain shown in Figure 4.8, the linear fit for the curve is plotted for strain below 15%, and the slope is about 3.4. This result is reasonable, since the fiber is very close to the surface, the light spot on the surface is very small, and the fiber probe can hardly sense the curvature of the surface. It is safe to treat the sphere as a flat surface if the curvature radius is much larger than the probing distance (of course, fiber diameter can not be too large). As the surface continues to expand, saturation effect appears after the strain reaches 15%, corresponding to the limit of the linear range obtained from Figure 4.8, therefore the slope becomes smaller.

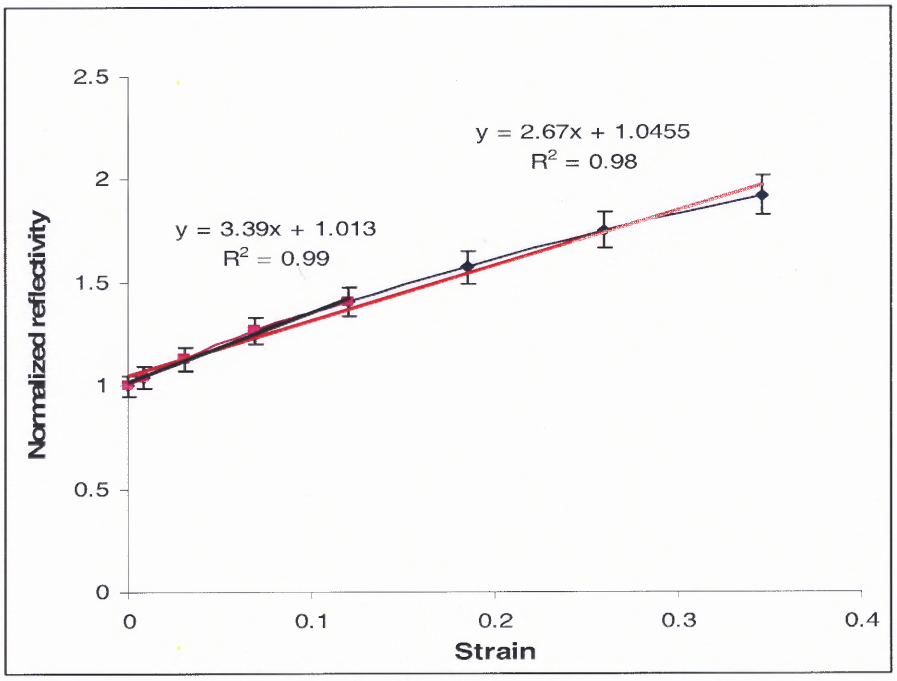

Figure 4.9 Normalized reflectivity vs. strain measured with Probe 2 (200/220μm fiber) at 1mm probing distance. Read line is the linear regression line for the experiment data. The over all data fitting shows a slope of 2.67. Within the linear range, the linear fitting gives a slope about 3.4.

The slope 3.4 is much larger than the value expected from flat surface experiments and the cylindrical surface simulation, which is about 1.3. Since the material of the sample is cut from the same polyvinyl material, they are assumed to have the same surface parameters. While it is possible that the surface parameter or even roughness pattern varies greatly within the same glove sample, which might cause dramatic slope change from one region to others, there are else error factors that should be considered, and will be discuss in the next chapter.

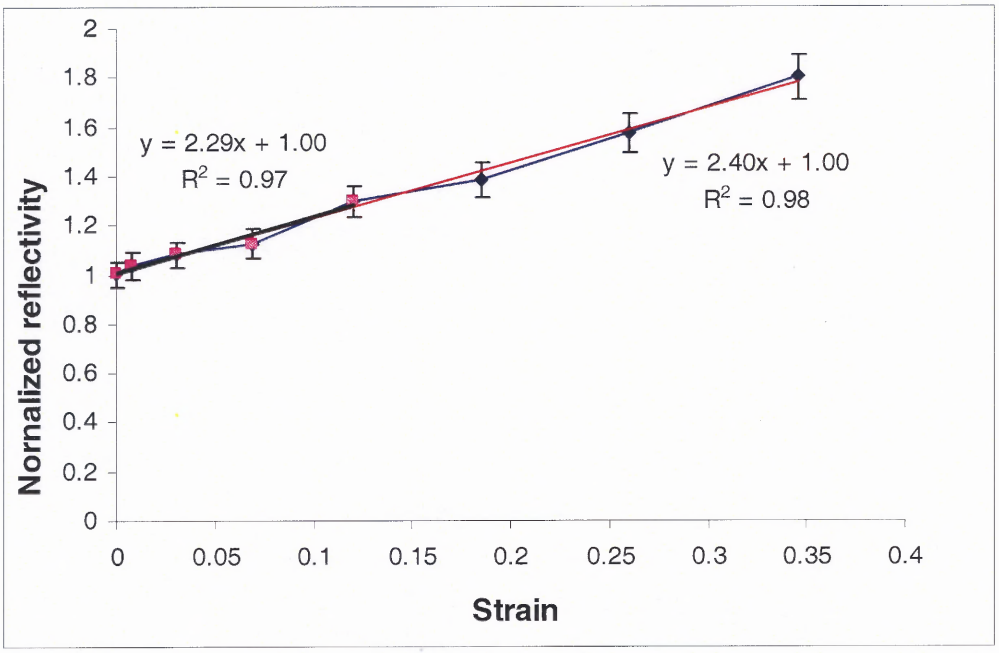

Figure 4.10 Result obtained with Probe 2 at 2mm probing distance, red line with slope of 2.40 is the linear fit of the entire measured data. The shorter line with slope 2.29 is the linear fit for strain less than 15%.

With 2mm probing distance, the similar result obtained by Probe 2 is shown in Figure 4.10. The slope reduces to about 2.3, but linearity is still maintained. However, when the probing distance is more than 3mm with the same probe, the behavior of the normalized reflectivity under the strain shows a different trend.

The corresponding plots for 3mm, 4mm, and 5mm probing distance are exclusively shown in Figure 4.11. At the beginning of the expansion, and for all the three different probing distances, normalized reflectivity decreases until the strain reaches about 7%, then it starts to increase as the strain continues to increase. Within the linear range of the elasticity (strain<15%), the linear relationship between the normalized reflectivity and the strain is not valid for these probing distances.

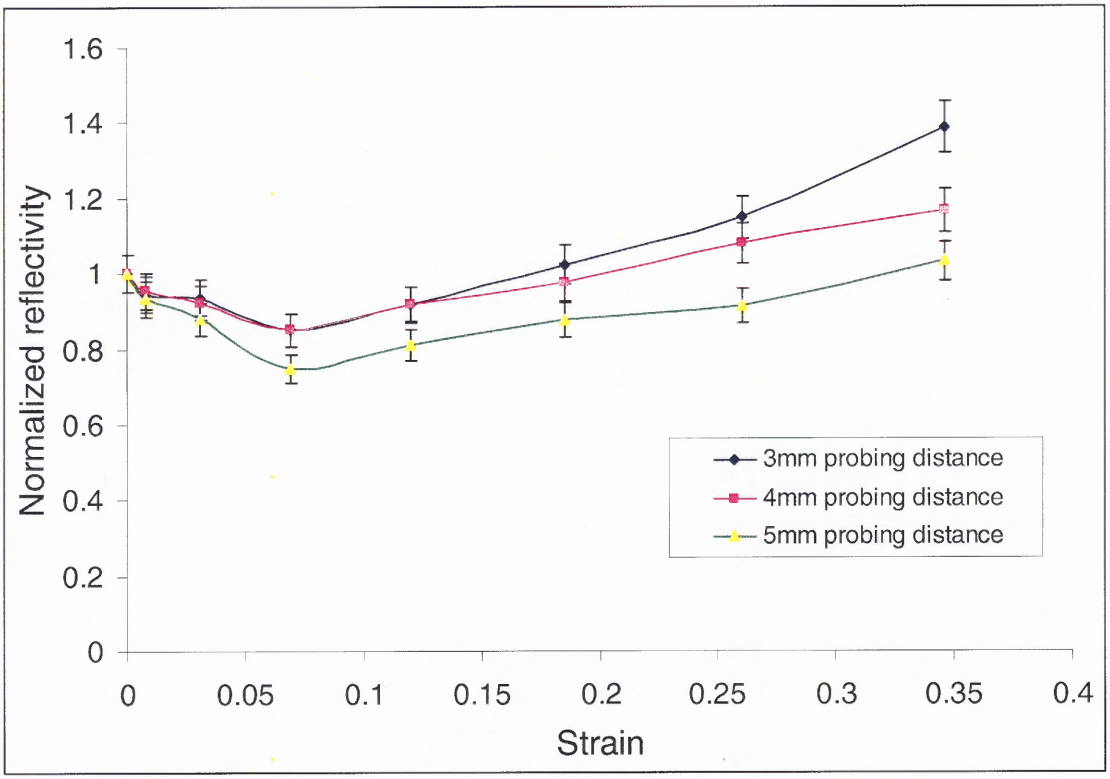

Figure 4.11 The behavior of normalized reflectivity under strain for 3mm, 4mm, and 5mm probing distance with Probe 2. The normalized reflectivity first decreases as the surface expands, after the surface strain exceeds about 7%, the normalized reflectivity starts to increase.

It is also noticed that the decreasing of the normalized reflectivity for 5mm probing distance is faster than those of the 3mm and 4mm probing distances, while the increasing of the normalized reflectivity for 5mm probing is slightly slower than that of 4mm case, which is in turn slower than that of 3mm case. This can be explained as following:

First, when the probing distance is comparable to the radius of curvature of the surface, the incident light spot size on the surface will be larger, and the increased curvature of the surface introduces more spreading of the light, thus the flat surface approximation is not valid for this case. Hence, one should not expect a linear relation

between the strain and the normalized reflectivity. This effect can be readily illustrated in the following geometrical sketch (Figure 4.12).

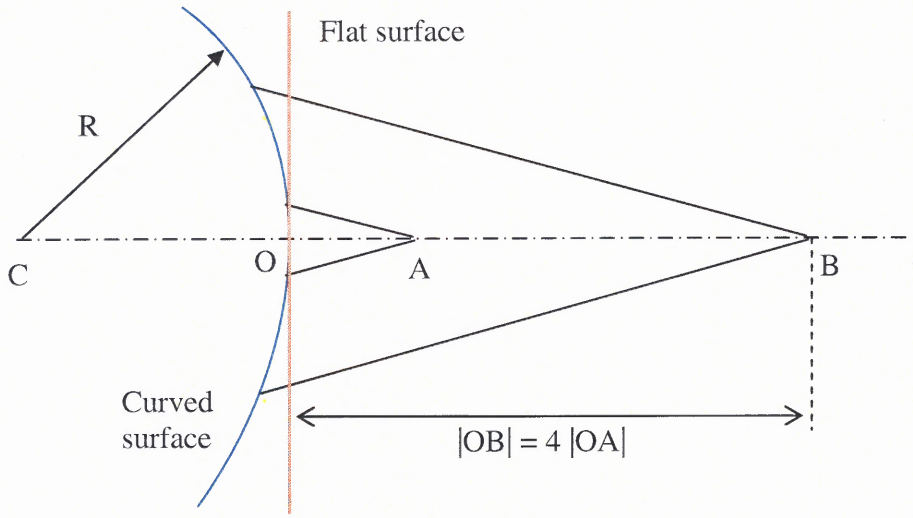

Figure 4.12 For small probing distance, the curved surface cab be treated as flat one with good approximation; for larger probing distance, the approximation is not valid.

Second, not only the curvature radius changes during the expansion of the surface, but also its rate of change differs. The initial expanding of the flat surface causes the curvature radius to decrease from infinity to a radius comparable to the probing distance very quickly, and the global curvature introduces extra light spreading, which tends to decrease the specular reflection. Meanwhile, the strain in the surface works in a contrary way, which reduces the surface roughness causing the specular reflection to increase. These two factors compete with each other. Initially the former factor dominates since the curvature radius increases very fast; after the turning point, the later factor dominates, since the curvature radius increases much slower. The longer the probing distance the stronger the former factor. The over all effect is that the normalized reflectivity decreases

first, it then increases after the strain reaches certain value. And for longer probing distance, it shows sharper decreasing and slower recovering of the normalized reflectivity.

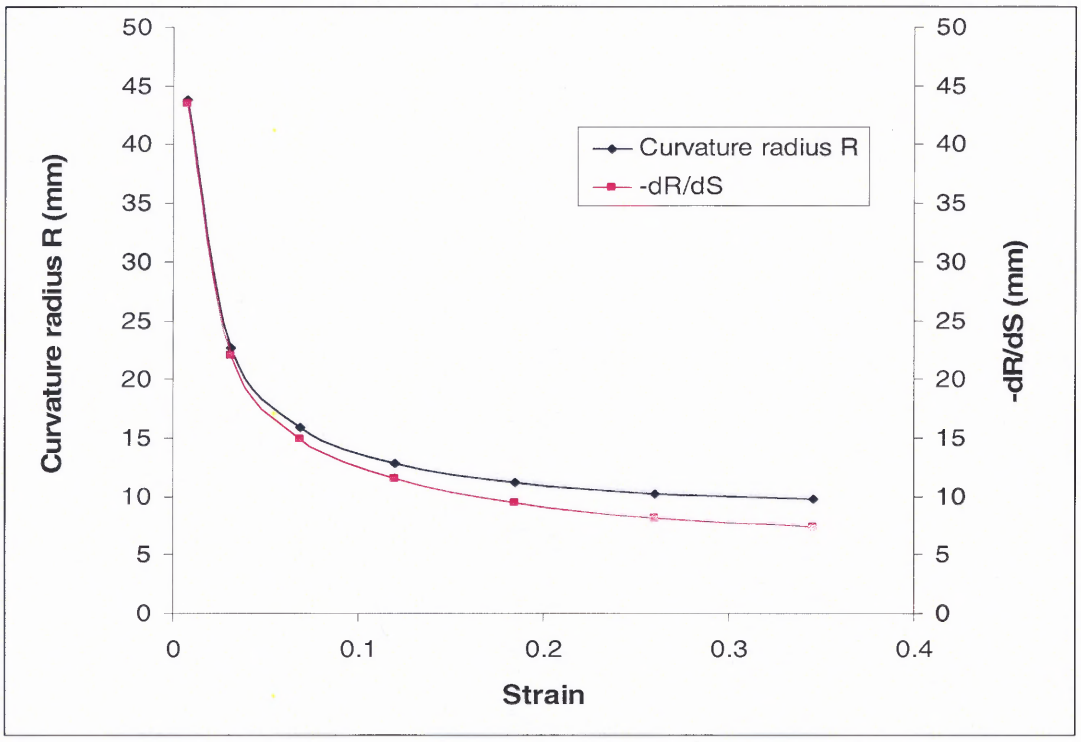

Figure 4.13 Curvature radius vs. strain and its derivative, -dR/dS is the absolute value of the curvature radius changing rate with respect to the strain. It is obvious that with small strain at the beginning of the surface expansion, the rate at which the radius changes is the largest.

To better understand this, the curvature radius vs. strain curve and its derivative curve were plotted with the help of Equation (4.2) and Equation (4.5). The plots are shown in Figure 4.13.

All of the probes under investigation exhibit the similar relationship between the normalized reflectivity and the strain in the sample. However, the position of the turning point varies and depends on the probe configuration. Figure 4.14 shows the results obtained with Probe 3 on the same sample.

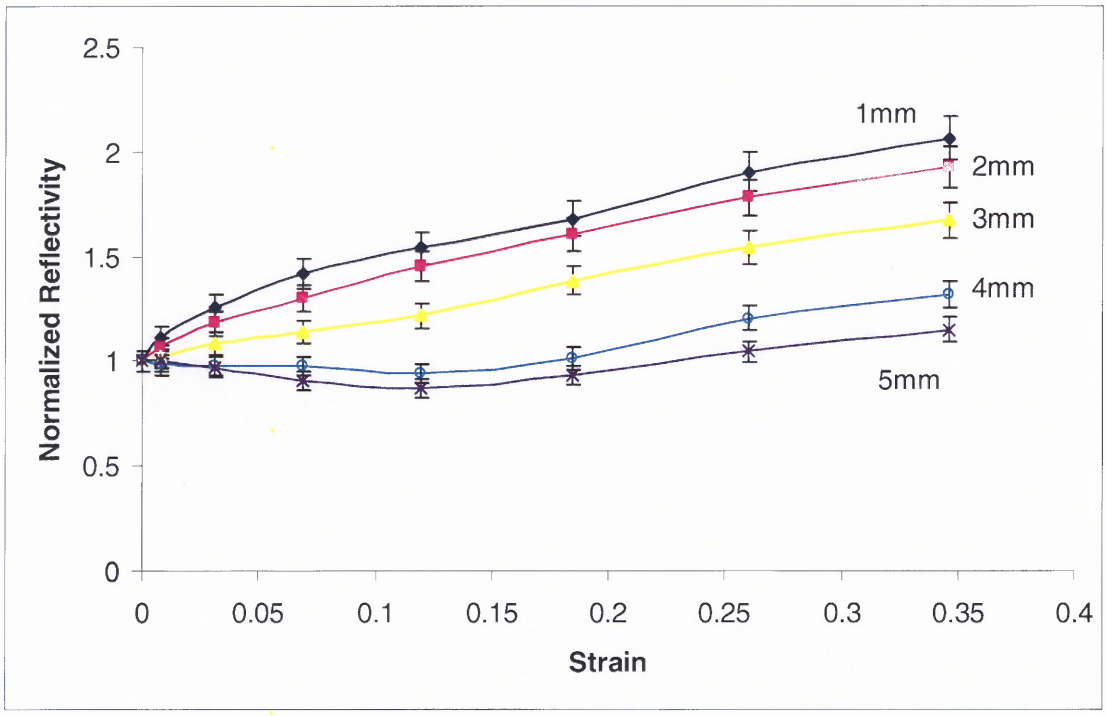

Figure 4.14 The behavior of the normalized reflectivity under strain with Probe 3 (485/500μm fibers) at 1mm~5mm probing distances.

4.2.4 Discussion

In most applications (i.e., blood vessels), some amount of curvature is already present before the surface is exposed to any external mechanical load. The curvature changes continuously as the strain builds due to the external load. Hence, it is possible that even with large probing distances, the decreasing of the normalized reflectivity does not appear, a fairly good linearity in the entire measurement may still be obtained (consider the cases with Probe 2 at 3mm, 4mm, 5mm, and if the surface initial curvature is more than $0.077mm^{-1}$(or radius less than 13mm). However, the slope would vary with different probing distance. It is also noticed that if the initial surface is already or more than a half sphere, the expansion of the surface would reduce the curvature, at this circumstance,

both of the factors discussed above have positive contributions to the normalized reflectivity, which introduces larger slope compare with flat surface cases.

Following the same argument, the corresponding analysis on the concave surface cases can be done. In applications, the surface curvature condition and how the curvature changes during the mechanical load vary differently, hence analysis should be aimed at a specific application. It is possible that with certain surface parameters and probing conditions, only one factor of the two dominates during the entire experiment, which results in monotonic decreasing or increasing of the normalized reflectivity even the probing distance is large. No doubt that if the probe size is small compared with the curvature radius and the probe is put very close to the curved surfaces, the case would be reduced to the flat surface condition as demonstrated here for 1mm and 2mm probing distances with Probe 2.

In order to isolate and better understand the effects of the changing curvature on the behavior of the normalized reflectivity, simulations on the cases where the curvature of the surface does not change with the strain are helpful. The ray tracing of the reflection on a cylindrical surface with radius 30mm, and roughness Ag=4 is performed. Using the parameters of Probe 2 and 3mm probing distance, the normalized reflectivity vs. strain plot is shown in Figure 4.15. It is clear that the linearity and the slope are both maintained from a flat surface case, indicating that even if the surface is curved, as long as the curvature does not change with strain, the linear relationship between the normalized reflectivity and strain would still hold.

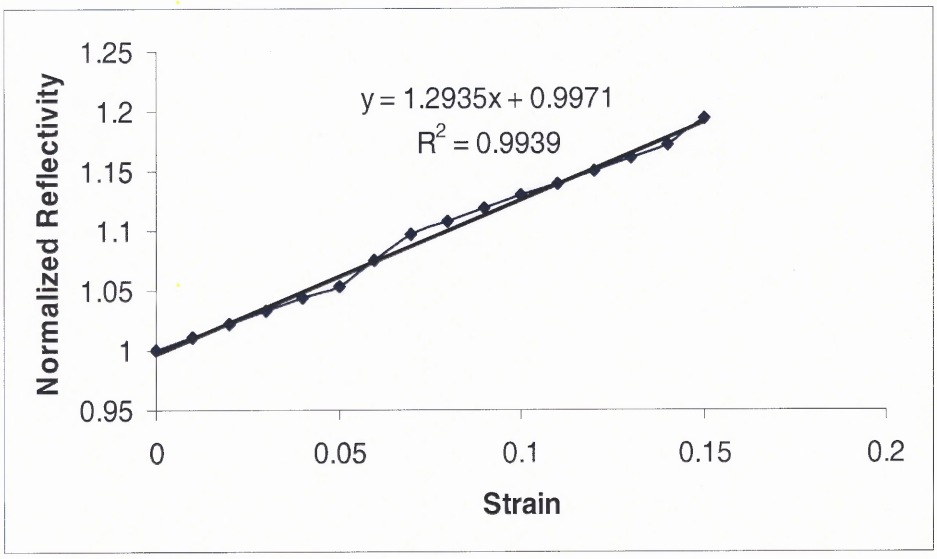

Figure 4.15 Simulation result with fixed 30mm radius cylinder surface using probe 2 at 3mm probing distance.

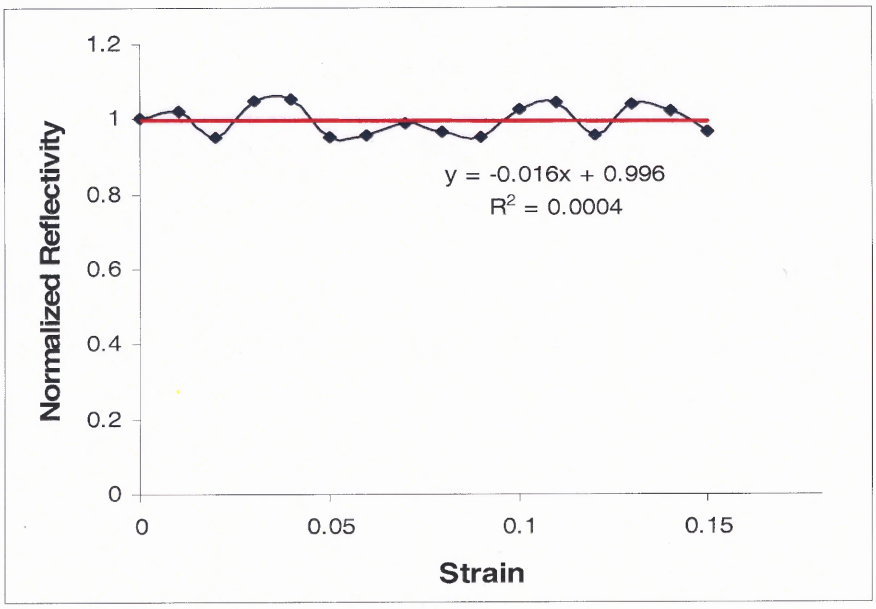

Figure 4.16 When the probing distance (1mm) is comparable to the curvature radius (1mm) of the surface, for Probe 2 there is no evidence showing that linear relationship between the normalized reflectivity and the strain maintains for a cylindrical surface.

However, this is only true for large radius surfaces. When the curvature radius is comparable to the probing distance, the above result is not correct. The simulation with

an extreme case, in which the radius of the cylinder is only 1mm, and the probing distance is also kept at 1mm with fiber parameters of Probe 2, and the tracing of 10,000 rays (Figure 4.16), reveals that the normalized reflectivity shows no trend to increase with the strain.

4.2.5 Summary

From above discussion, one can summarize the results for curved surface cases into following points:

1) For cases that the curvature of the curved surface does not change during the expansion of the surface, the linear relationship between normalized reflectivity and strain is still valid, except for those that the curvature radius is small enough to be comparable to the probing distance.

2) For convex cases where the curvature increases during the surface expansion, the behavior of the normalized reflectivity under the strain depends on the probing conditions. For small probing distance, the linear relationship is valid; for larger probing distance, the normalized reflectivity decreases with the strain first, then after the turning point, it starts to increases; both the decreasing rate and the increasing rate depend on the probing distance.

3) Concave cases and the decreasing curvature cases can be treated accordingly with the same method. Generally, if the probing distance<< the radius of curvature, the effects of the changing curvature can be neglected, and the change of surface roughness will dominate the behavior of the measured surface reflectivity.

It has been demonstrated earlier that polarizing fiber probes without collimating lens for the incident fiber can offer acceptable results on flat rough surfaces. However, for curved rough surfaces, the performance of the fiber probes depends on the probing distance, which introduces complications in the application and is a significant drawback for the fiber system. Since the light spot generated by the collimated light beam on the sample surface would not change its size with the probing distance, thus the complications discussed above could be significantly reduced.

4.3 Optimization of the Fiber Probe Configuration

Because many factors are involved in the measurement of the normalized reflectivity and each application has its own conditions to determine which fiber configuration is the optimum one, it is impossible to give the optimum configurations for all the applications. However, the general design rules still can be summarized as following:

- Use small N.A. and small size fiber as incident fiber and put the probe close to the surface, if the signal is strong enough. However fiber size should be much larger than the local features of the stretchable surface.

- The receiving fiber diameter and N.A. can be relatively larger than the incident fiber, but keep the separation between fibers as small as possible. Larger diameter fibers usually introduce more geometrical errors, especially if the probing distance is very small.

- N.A. is not a major concern in the application of flat surface cases if the probing distance is much larger than the fiber diameter. However, in curved surface cases, the N.A. has significant influence on the performance of the fiber probe. Using small N.A. fibers would reduce the complications caused by different probing distances, and a collimating lens for incident fiber would completely eliminate those complications.

- The effects of the fiber size can be transformed to the effects of probing distance for flat surface conditions, providing flexibilities of the design in an application.

The first three points are straight forward, only the last point is to be discussed here. It suggests that if one can not find small enough fibers, one may simply increase the probing distance will larger diameter fibers to achieve the desired goals. In other words, only the fiber diameter to probing distance ratio matters. For example in a flat surface case, Probe 2 (200/220μm, N.A.=0.22) at 2mm probing distance is equivalent to a probe with fiber diameter 400/440μm N.A.=0.22 at 4mm probing distance, as long as the fiber separations are small enough to be neglected. However, if the surface is curved, one has to double the radius of curvature of the surface accordingly in this example if no collimating lens is used.

CHAPTER 5

DISCUSSION

5.1 Validity of the Surface Roughness Modeling

As already discussed in previous chapters, the success of the sinusoidal roughness model for skin tissue originates from the physiology of the skin and its topology measurements, which show quasi-periodic skin structure[6,7,44-46]. This model has been used to explain how the surface patterns of the skin change as a result of excess stress. Later, Schulkin[47] etc. proved mathematically that the linear relationship between the normalized reflectivity and the applied stretch is applicable to common stretchable rough surfaces. In this theory, the author used Fourier analysis to introduce the effective roughness of the surface such that the treatment for sinusoidal roughness model can be directly transplanted to common surface roughness patterns[47].

This theory was supported by experiments in prior works[6,7,47] as well as results obtained on polyvinyl samples in the present work. However, this theory assumes that each sinusoidal component of the roughness does not change its pattern under stress, such that the partial contribution to the reflectivity from particular sinusoidal component would not change either. More over, the two dimensional treatment appears not enough for general surface roughness pattern, since most materials show nonzero Poisson ratio, which introduces morphology change in directions perpendicular to the stress. If the actual surface path length is intrinsically stretchable, this theory would also introduce significant errors compared with experimental results.

Nevertheless, this theory is acceptable for its simplicity with reasonable imperfections, which may cause minor discrepancies with experiments for particular

samples. In flat surface cases in Chapter 4, It has been pointed out that the surface modeling error could be the reason for slopes less than 1. In the curved surface cases (1mm and 2mm probing cases), one obtains much higher slope (2.67 and 2.40 for 1mm and 2mm probing distance respectively). In addition to the factors (discussed in Chapter 4) which cause dramatic slope change from the predicted value by the theory, the factor originating from the three dimensional nature of the surface roughness should be considered. For flat surface case, the stress in one direction will introduce excess strain along the perpendicular directions, because the Poisson ratio is not zero for the material (typical Poisson ratio for rubber is 0.5). In the curved surface cases, strains in two directions decrease the surface roughness in both dimensions, causing much higher slope compared with that predicted by the theory for the one-direction roughness model.

5.2 Performance Compared With Bulk Optics System

Compared with the flat surface results obtained through bulk optic system on the same type of samples shown in Figure 1.3 and Figure 3.2, the results of fiber optic system shown in Figures 4.1, 4.2 and 4.3 exhibit higher noise level and smaller slope for the normalized reflectivity vs. strain curves. Figure 5.1 shows the plots of a comparison between a typical fiber optic result and a bulk optic result.

Before the discussion of the noise, several possible noise sources can be excluded first: As discussed in Chapter 4, the fluctuations of laser source power and polarization, which are equally present in bulk optic system, can not be major sources that introduce excess noise level in fiber optic system. The background room light should not cause the problem either, since a lock-in amplifier was employed in the experiments, and this

background room light is also equally present in the bulk optic system. The electronics employed in the fiber optic system is the same as in the bulk optic system, which could not be responsible for the higher noise level in the fiber optic system. It is reasonable to assume that the levels of these noises discussed above are essentially not changed in the transition from the bulk optic system to the fiber optic configuration. It is the decrease of the optical signal level that causes the signal-to-noise ratio smaller in fiber optic system, consequently gives rise to the relative noise level in the normalized reflectivity vs strain plots.

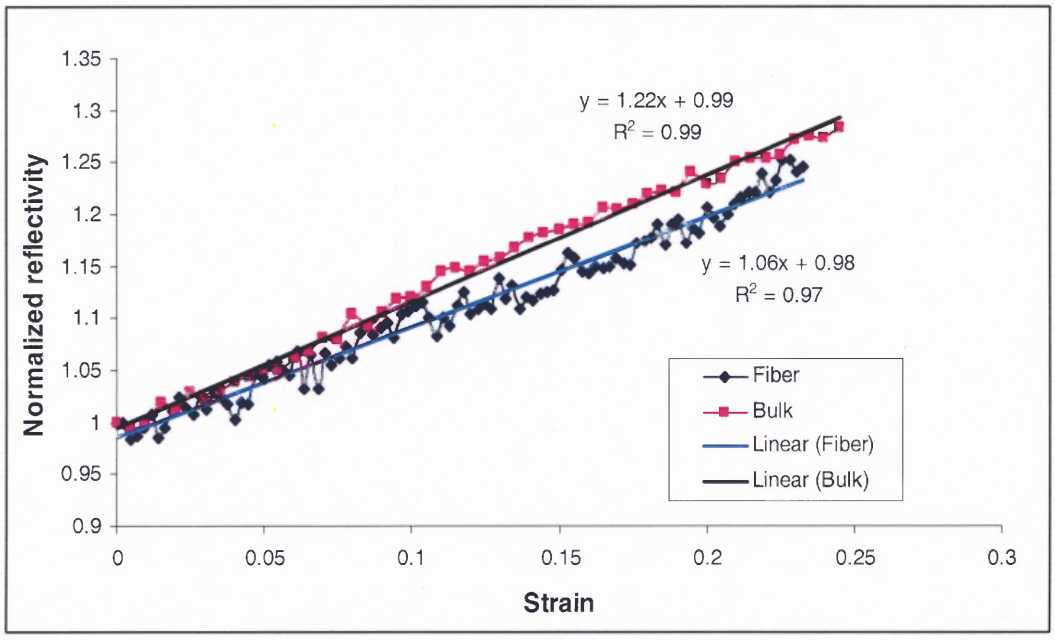

Figure 5.1 A fiber optic result obtained with Probe 2 at 3mm probing distance compared with result obtained from bulk optic system.

The incident light power of the bulk optic system is about 5 times higher than that of the fiber optic system (Probe 2), while the receiving fiber has an acceptance angle comparable to the lens acceptance angle in the bulk optic system. Moreover, the incident beam of the fiber optic system is more divergent, although this divergence does not

jeopardize the linear relationship between normalized reflectivity and the strain, it does significantly reduce the effective incident power, because only light from the central region of the light cone is contributive. Thus compared with fiber system, the bulk optic system has higher signal to noise ratio.

The noise induced by the perpendicular incident angle in the fiber system rather than Brewster angle in the bulk optic system is also noticed. The benefits of Brewster angle incidence have not been systematically studied in the conditions where the incident light is linearly polarized. Research on the light reflection from soft tissues observed that at the vicinity of the Brewster angle incidence, the detected optical signal has much lower noise level compared with other incident angles (H. C. Lim, Pers. Comm.).

Another possible noise source unique to the fiber system is the modal noise from the incident multimode fiber[60-63]. As much as 10dB increase in noise power due to modal interference between different propagation modes in multimode fiber was reported decades ago, and the model noise level depends on the fiber specifications and the launching conditions[60]. Because the behavior of the modal noise is very similar to that of the laser speckles, using incoherent source (such as LED) would reduce the modal noise significantly[7] (H. C. Lim, Pers. Comm.). Another way is to use a single mode fiber as the incident fiber, such that no interference between modes appears.

The lower slopes of the fiber system compared with the bulk system may come from two reasons. One is the geometrical error of the probe discussed in Chapter 4. The geometrical error reduces the power detected from specular reflection, and more importantly, it reduces the detected specular reflection power more significantly at heavily strained surface than the lightly strained one. The other reason is that in the fiber

system, the light spot diameter on the sample is usually several times larger than that of the receiving fibers. In the theoretical analysis in Chapter 2, only the central part of the light spot is assumed to be significant to the normalized reflectivity, while this assumption is acceptable, it has obvious flaws. The ratio of the spot size to the probing distance is limited by the fiber parameters, indicating small diameter and small N.A. fibers are desired in the applications. It is also due to these reasons that a varying slope for different probing distance for each fiber probe is observed.

5.3 Blood Vessel Elasticity Measurement Application

As discussed in Chapter 1, based on the fiber optic reflectivity sensing technique, a blood vessel elasticity measurement device can be modeled. In this modeling, it is assumed that a section of normal blood vessel in human body with a cylindrical wall is under the investigation. The method can be readily used on the study of an aneurysm, where a cylindrical surface is replaced by a sphere. It has been demonstrate in this work that if the fiber probe is small and close to the object curved surface area, the linearity between the normalized reflectivity and the strain would be maintained. The scattering characteristics of light in the blood and the vessel wall, the vessel's structure and its non-readily access position in human body make the fiber polarization probing an ideal technique for biomechanical investigation of the wall tissue.

If the blood vessel diameter D is known, with the pressure P changing on the wall of the blood vessel due to the pulsating of the heart, the normalized reflectivity R of the inner surface of the wall would change accordingly, and the reflectivity behavior could be predicted by the theory. Analyzing the relationship between the behavior of P and R may

lead to the knowledge of the bio properties of the wall tissue such as its elasticity. Since the heart pulsates at a frequency about 1.25Hz, a phase sensitive detection still can be employed with modulated optical frequency above several thousand Hz and time constant less than a millisecond.

Let the maximum and the minimum of the pressure in one heart cycle be P_M and P_m respectively. According to Laplace's equation, and the cylindrical structure of the blood vessel, the following relations hold:

$$\frac{\alpha_M}{D_M/2} - \frac{\alpha_m}{D_m/2} = P_M - P_m \tag{5.1}$$

$$\alpha_M = YtS_M, \quad \alpha_m = YtS_m \tag{5.2}$$

where α is the circumferential tension (N/m) in the vessel wall, M and m denote the maximum and minimum values respectively in one heart cycle, Y is the Young's modulus (for simplicity, assumed isotropic), and t is the thickness of the wall (although the actual wall consists of several layers with specific thickness and properties, an effective thickness with uniform mechanical property can be estimated), S is the strain of vessel in circumferential direction.

It should be pointed out that typically Young's modulus of the blood vessel wall varies with mechanical load, and it is characterized by a series of values measured under a set of stresses[64,65]. For simplicity, and small amount of strain (<20%) condition, the Young's modulus can be treated as a constant in one heart cycle. For major arteries, $D_M \approx D_m = D$, small stretch condition applies.

Applying the linear relationship:

$$R_M = 1 + kS_M, \text{ and } R_m = 1 + kS_m$$

where R_M and R_m are the maximum and minimum normalized reflectivity respectively in one heart cycle, k is to be determined from the surface roughness. Replacing S_M and S_m by R_M and R_m respectively yields:

$$Y = \frac{kD}{2t}\frac{P_M - P_m}{R_M - R_m} \tag{5.3}$$

The application schematic is shown in Figure 5.2.

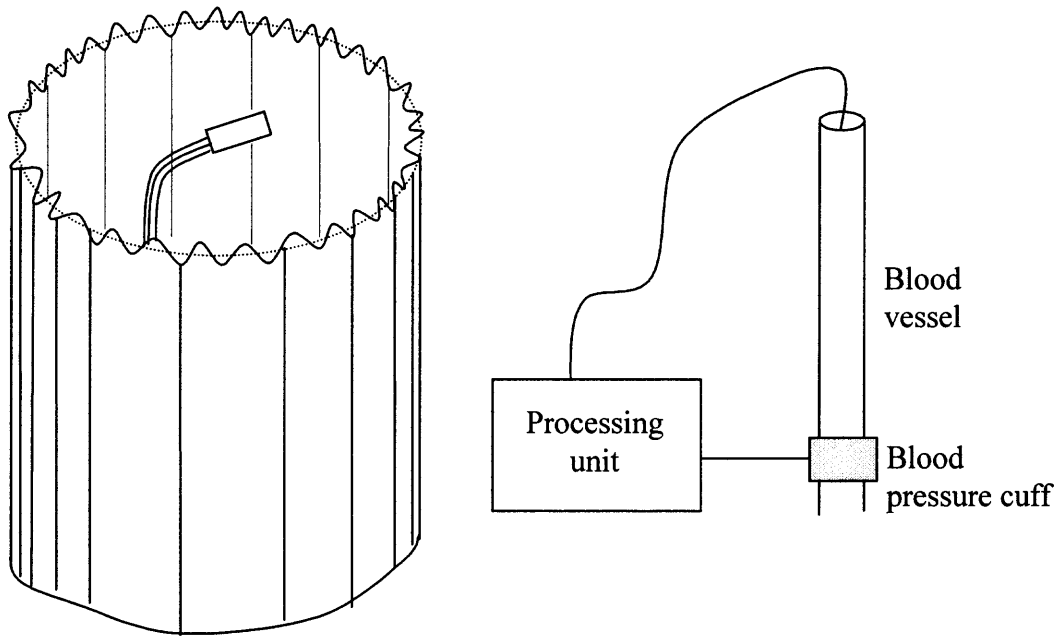

Figure 5.2 Fiber optic probing of the blood vessel wall for the estimation of the elasticity of the vessel tissue. A miniaturized pressure sensor can be attached to the fiber probe.

To evaluate whether this method is applicable in clinics, one needs to estimate how much reflectivity difference can be introduced due to the strain change in the vessel wall. Equation (5.3) can be rearranged as:

$$\Delta R = R_M - R_m = \frac{1}{2Yt} kD(P_M - P_m) \tag{5.4}$$

The parameters of a human abdominal aorta: the diameter D is about 30mm(largest), and the thickness t is about 2.5mm, the surface roughness Ag is about 1, hence k=5. The

Young's modulus for aorta arteries is in the order of $10^6 N/m^2$. For normal diastolic pressure 80mmHg and systolic pressure 120mmHg, the change in normalized reflectivity can be estimated by Equation (5.4) to be $\Delta R = 0.12$. If the reflectivity is normalized to the diabolic reflectivity, the change would be 9.1%, indicating that the increase of normalized reflectivity can be detected in presence of systolic pressure compared with that of diabolic pressure.

The risk of rupture of a brain aneurysm with the diameter less than 10mm is very low[66]. For giant brain aneurysms larger than 25mm in diameter, the risk of rupture for the first year is about 6%. Aneurysms that draw clinical attention usually have a diameter larger than 10mm. From the experimental result on the polyvinyl sample with an average sphere diameter about 30mm (Chapter 4), it is easy to extract the fiber probe configuration that would work on 10mm diameter aneurysms by comparison (Table 5.1):

Table 5.1 Comparison between Surface Diameter and Fiber Probe Configuration

Surface diameter	Fiber core diameter	Fiber N.A.	Probing distance
30mm	200μm	0.22	1~2mm
10mm	67μm	0.22	0.3~0.7mm

It is important to note that the data in Table 5.1 for 10mm surface diameter can be smaller than the listed values, which can provide better performance for the fiber probe. The probing distance can also be increased if a collimating lens is used for the incident fiber, such that the measurement would not be sensitive to the change of probing distances. The improved design of the fiber probe discussed in the next section is expected to increase the working range of the probing distance significantly.

5. 4 Improvements on the Design of the Fiber Probe

As discussed in previous sections that the fiber optic probes can work well on the flat surface cases and maintain the linearity between the normalized reflectivity and the strain. However, the fiber system suffers from lower signal-to-noise ratio and smaller slope compared with the bulk optic system. In the curved surface cases, when the curvature changes during the expansion of the surface, the linearity between the normalized reflectivity and the strain can only be achieved at short probing distances, for longer distances, the linearity does not appear. All of these problems are related to the same fact that the incident light beam is not collimated. A practical use of the fiber probe would require at least a collimating fiber lens in front of the incident fiber.

Two major improved configurations of the fiber probe are proposed here. A simplest design is to add a GRIN lens between the incident fiber and the polarizing plate as shown in Figure 5.3. This design would be comparable to a bulk optic system, because the two receiving fibers are equivalent to the aperture of the light collecting lens in the bulk optic system. However, due to a three-fiber configuration, the geometry error can not be removed.

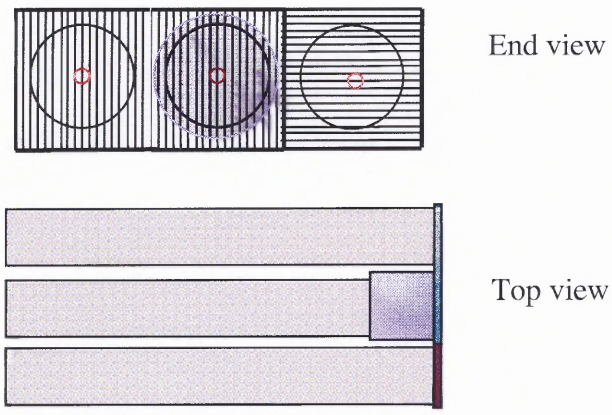

Figure 5.3 End view and top view of the proposed configuration of the fiber probe. A GRIN lens is sandwiched between the incident fiber end and the polarizing plate.

The geometry error can be removed if a single-fiber configuration is employed. In order to use the incidence of linearly polarized light and detection as well, polarization maintaining (PM) fibers must be employed. The system (Figure 5.4) essentially consists of a 3dB 2×2 coupler made from PM fibers, a beam splitter, and a GRIN lens, which is in front of the probe end. The fibers are oriented such that the polarization direction of the incident light is parallel to the fast axis of all the PM fibers. The beam splitter at the detector side separates the parallel component from the perpendicular component of the reflected light. Both the beam splitter and the GRIN lens can be directly glued to the end surface of the fiber.

Since the PM fibers are sensitive to the twisting and small bending, the handling of the sensor requires special attention. Because the two orthogonal polarization components of the reflected light have different attenuation rate in the PM fiber, the attenuation ratio between the two polarization modes should be calibrated before the measurements. As with common fiber system discussed previously, the back scattered or reflected optical power from the fiber or the GRIN lens is expected to be measured and removed by a void incidence on the sample.

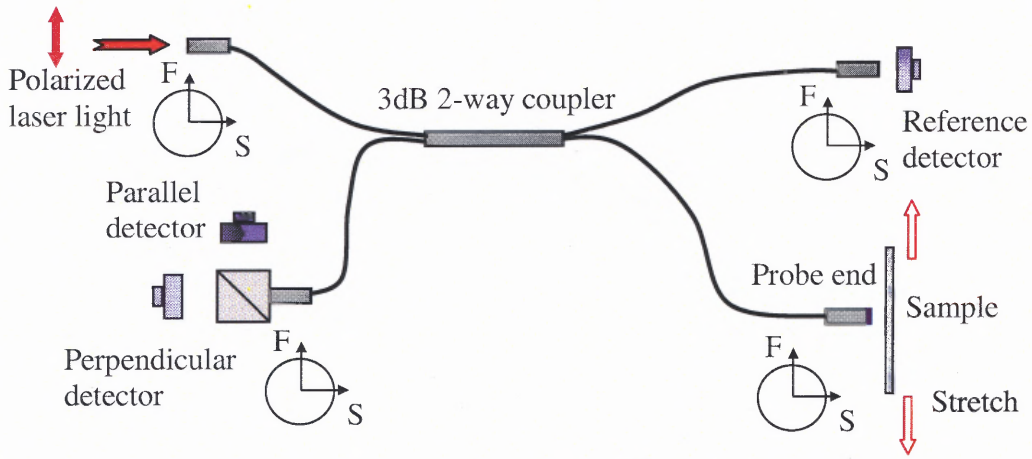

Figure 5.4 The configuration of the single-fiber probe using PM fibers.

With the implementation of the PM fiber system, it is expected that both the linearity and noise performance can be substantially improved. This part of work is intended to be done in the future efforts, which requires advanced fabrication tools. The experiment can start with 3dB 2-way couplers commercially made from standard single mode telecommunication fibers.

CHAPTER 6

CONCLUSION AND SUGGESTIONS

6.1 Conclusion

In this dissertation, a fiber optic system using polarization imaging technique was developed to investigate the potential applications of this technology on the strain/stress as well as surface roughness measurements of soft tissues. Inheriting the surface roughness model developed in the prior works, the original theory is improved such that it can predict the detailed behavior of the normalized reflectivity under the strain. The new theoretical analysis can treat not only very rough surfaces successfully, but also surfaces of moderate roughness with acceptable accuracy.

In the implementation of the fiber optic system, two kinds of application conditions were considered: 1) flat rough surface, 2) curved rough surface. A variety of fiber optic systems with different fiber configurations were fabricated for the experiments. These fiber optic systems did not employ the collimating lens for the incident fiber for cost effectiveness and simplicity of fabrication. Numerical simulations were used to compensate the short comings of analytical and experimental results. Experiments and simulation results suggested that the linear relationship between normalized reflectivity and strain in the flat sample can be maintained without critical restrictions. It is further shown by the experiments that the performance of the fiber optic system is insensitive to the fiber configurations under flat surface sensing conditions. However, for curved surface condition, the fiber system suffers from complications due to its dependence on

the probing distance. Expected solution for this problem is to use a collimating lens for the incident fiber.

The validity of the one dimensional surface roughness model was discussed, and possible error and noise sources in the experiments were explored. Finally, as an application example, a fiber optic system was proposed to measure the elasticity/stress/strain of tissues of the blood vessels.

6.1.1 Flat Surface Summary

Four fiber probes with different fiber configurations were employed in the experiments. All of them show that normalized reflectivity linearly increases with the strain in the sample. The normalized reflectivity of the flat surface is roughly proportional to the strain of the sample. The slope of the linearity is not very sensitive to the probe configurations for fiber core diameters ranging from 100μm (Probe 1) to about 735μm (Probe 4) and numerical aperture ranging from 0.22 (Probe 2) to 0.51 (Probe 3, 4). Considering the geometrical errors introduced by the fabrication of the probes (deviation from the direction of specular reflection for the receiving fiber), the experimental sensing accuracy can be optimized by varying the probing distance.

To optimize the system, smaller N.A. and diameter fibers are recommended for the incident fiber. Compared with the bulk optic system, the fiber optic system exhibits higher noise level and smaller slope of the linearity between the normalized reflectivity and the strain. Although the fiber probes without collimating lens provided good results in the experiments, a collimated incident light beam would enhance the performance of the fiber probe.

6.1.2 Curved Surface Summary

Simulation shows that for cases where the curvature of the curved surface does not change during the expansion of the surface, the linear relationship between normalized reflectivity and the strain is still valid, except for those that the curvature radius is smaller than or comparable to the probing distance. For curved surface where its curvature changes during the expansion, two factors that determine the behavior of the reflectivity under the strain should be considered: 1) the curvature change introduces extra convergence or divergence of the reflected light, which enhances or weakens the reflection in the specular direction. 2) the strain reduces the surface roughness, hence increases the specular reflection. For cases where the curvature increases during the surface expansion and the surface is convex to the fiber probe, the behavior of the normalized reflectivity under the strain depends on the probing conditions. For small probing distance, the linear relationship is valid; for larger probing distance, the normalized reflectivity first decreases with the strain, then after the turning point, it starts to increase; both the decreasing rate and the increasing rate depend on the probing distance. To remove these complications, a focusing or collimated incident light beam would be necessary. Hence, a fiber probe with incident collimating lens is recommended for the curved surface cases. The two dimensional expansion reality of the surface in applications presents new challenges for the modeling of surface tomography.

6.2 Future Research Suggestions

Although the critical part of the system is the fiber probe, to make the system portable, the launching optics of the experiment need to be replaced by fiber optic features. The light source can be replaced by a diode laser with a fiber pigtail and operating in pulse mode, such that a full fiber optic system with integrated phase sensitive detection could be established. A small sized and portable fiber system is desired in future studies.

As discussed in Chapter 5, the fabrication of the fiber probe may include the integration of a fiber lens and polarizers on the end of the fiber probe. A single-fiber system fabricated from a PM fiber coupler is expected to substantially improve the performance of the fiber sensor.

Since the probing conditions in real applications are so diverse, computer simulations are necessary before the design of the fiber probe for a specific application. Through the simulations, optimized fiber configuration can be obtained. A high efficient numerical method is critical in future work. Current method developed in the present work has very limited versatility and computing capability. The simulation may include the modeling of three dimensional random roughness surfaces if the computing resource is abundant.

In vivo experiments on blood vessels or other tissues are the ultimate goal of this work. However, due to the complexity and the risk of these experiments, it is not recommended at this stage. *In vitro* experiments on animal tissues with the collimating fiber probe are desired and feasible in the future work.

REFERENCES

1. S. G. Demos, R. R. Alfano, "Optical polarization imaging," *Appl. Opt.* **36**, 150-155 (1997).

2. Arthur F. Gimitro, David Aziz, "Confocal microscopy through a fiber-optic imaging bundle," *Opt. Lett.* **18**, 565-567 (1993).

3. Cheng Liang, Michael R. Descour, "Fiber confocal reflectance microscopy (FCRM) for *in-vivo* imaging," *Optics Express* **9**, No. 13, 821-830 (2001).

4. Jan S. Dam, Carsten B. Pedersen, Torben Dalgaard, Paul Erik Fabricius, Parkasa Aruna, and Stefan Andersson-Engels, "Fiber-optic probe for noninvasive real-time determination of tissue optical properties at multiple wavelengths," *Appl. Opt.* **40**, 1155-1164 (2001).

5. Cheng Liang, Kung-Bin Sung, Rebecca R. Richards-Kortum, and Michael R. Descour, "Design of a high-numerical-aperature miniature microscope objective for an endoscopic fiber confocal reflectance microscope," *Appl. Opt.* **41**, 4603-4610 (2002).

6. John F. Federici, Nejat Guzelsu, Hee C. Lim, Glen Jannuzzi, Tom Findley, Hans R. Chaundry, and Art B. Ritter, "Nonoinvasive light-reflection technique for measuring soft-tissue stretch," *Appl. Opt.* **38**, 6653-6660 (1999).

7. H. C. Lim, "Two-dimensional reflectivity polarization elastometry imaging techniques (PIET) of soft tissue," *NJIT Dissertation* in Applied Physics (2002).

8. A. J. Welch, M. J. C. van Gemert, "Optical Thermal Response of Laser Irradiated Tissue," Plenum, New York, (1995).

9. C. Cacou, J. M. Anderson, and I. F. Muir, "Measurement of closing force of surgical wounds and relation to the appearances of resulting scars," *Med. Bio. Eng. Comput.* **32**, 638-642 (1994).

10. T. Gibson, "Physical properties of skin," in *Plastic Surgery Volume 1: General Principles*, J. G. McCarthy, ed. (Saunders, Philadelphia, Pa., 1990), pp. 207-220.

11. C. Cacou and I. F. K. Muir, "Effects of plane mechanical forces in wound healing in humans," J. *R. Coll. Surg. Edinburgh* **40**, 38-41 (1995).

12. B. D. Bucalo and M. Iriondo, "Photoelastic models of wound closure stress," *Dermatol. Surg.* **21**, 210-212 (1995).

13. B. Sumpio, A. Banes, and L. Levin, "Mechanical stress stimulates aortic endothelial cells to proliferate," *J. Vasc. Surg.* **6,** 252-256 (1981).

14. B. Sumpio and M. Windmann, "Enhanced production of an endothelium derived contracting factor by endothelial cells subject to pulsative stretch," *Surgery* **108**, 277-282 (1990).

15. M. U. Nollert, E. R. Hall, S. G. Eskin, and L. V. McIntire, "Effect of flow on arachidonic acid metabolism in human endothelial cells," *Biochim. Biophys. Acta.* **1005**, 72-78 (1989).

16. W. F. Larabee, G. A. Holloway, and D. Sutton, "Wound tension and blood flow in skin flaps," *Ann. Otol. Rhinol. Laryngol.* **93**, 112-115 (1984).

17. A. Manios, J. Katsantonis, A. Tosca, C. N. Skulakis, and D. Tsiftsis, "The finite element method as a research and teaching tool in the analysis of local skin flaps", *Dermatological Surgery* **22**, 1029-1034, (1996).

18. S. B. Cantor, M. F. Mitchell, G. Tortolero-Luna, C. S. Bratka, D. C. Bodurka, and R. Richards-Kortum, "Cost-effectiveness analysis of disgnosis and management of cervical squamous intraepithelial lesions," *Obstet. Gynecol.* **91**, 270-277 (1998).

19. Kristen Carlson, Matthew Chidley, Kung-Bin Sung, Michael Descour, Ann Gillenwater, Michele Follen, and Rebecca Richards-Kortum, "*In vivo* fiber-optic confocal reflectance microscope with an injection-molded plastic miniature objective lens," *Appl. Opt.* **44**, 1792-1797 (2005).

20. T. Collier, A. Lacy, R. Richards-Kortum, A. Malpica, and M. Follen, "Near real-time confocal microscopy of amelanotic tissue: detection of dysplasia *in ex vivo* cervical tissue," *Acad. Radiol.* **9**, 504-512 (2002).

21. H. D. Cavanagh, J. V. Jester, J. Essepian, W. Shields, Webb, and M. A. Lemp, "Confocal microscopy of the living eye," *CLAO J.* **16**, 65-73 (1990).

22. Rajadhyaksha, M. Grossman, D. Esterowitz, R. H. Webb, and R. R. Anderson, "*In vivo* confocal scanning laser microscopy of human skin: melanin provides strong contrast," *J. Invest. Dermatol.* **104**, 946-952 (1995).

23. M. Rajadhyaksha, R. R. Anderson, and R. H. Webb, "Video-rate confocal scanning laser microscope for imaging human tissues in vivo," *Appl. Opt.* **38**, 2105-2115 (1999).

24. D. L. Dickensheets and G. S. Kino, "Silicon-micromachined scanning confocal optical microscope," *J. Microelectromech. Syst.* **7**, 38-47 (1996).

25. T. D. Wang, C. H. Contag, M. J. Mandella, N. Y. Chan, and G. S. Kino, "Dual-axes confocal microscopy with post-objective scanning and low-coherence heterodyne detection," *Opt. Lett.* **28**, 1915-1917 (2003).

26. G. J. Tearney, R. H. Webb, and B. E. Bouma, "Spectrally encoded confocal microscopy," *Opt. Lett.* **23**, 1152-1154 (1998).

27. K. B. Sung, C. Liang, M. Descour, T. Collier, M. Follen, and R. Richards-Kortum, "Fiber-optic confocal reflectance microscope with miniature objective for in vivo imaging of human tissues," *IEEE Trans. Biomed. Eng.* **49**, 1168-1172 (2002).

28. H. Bengtsson, B. Bengtsson, D. Bergqvist, "Incidence and prevalence of abdominal aortic aneurysms, estimated by necropsy studies and population screening by ultrasound," *Ann. N. Y. Acad. Sci.* **800**, 1-24 (1996).

29. K. Ouriel, RM. Green, C. Donayre, CK. Shortell, J. Elliot, JA. DeWeese, "An evaluation of new methods of expressing aortic aneurysm size: relationship to rupture," *J. Vasc. Surg.* **15**, 12-20 (1992).

30. MI. Patel, DT. Hardman, CM. Fisher, M. Appleberg, "Current views on the pathogenesis of abdominal aortic aneurysms," *J. Am. Coll. Surg.* **181**, 371-382 (1995).

31. H. J. Steiger, R. Aaslid, S. Keller, and H. J. Reulen, "strength, elasticity and viscoelastic properties of cerebral aneurysms," *Heart and Vessels* **5**, 41-46 (1989).

32. A. M. Brant, V. G. Rodgers, and H. S. Borovetz, "Measurement *in vitro* of pulsatile arterial diameter using a helium-neon laser," *J. Appl. Physiol.* **62**, 679-683 (1987).

33. L. Caputo, A. Tedgui, P. Poitevin, and B. I. Levy, "*In vitro* assessment of diameter-pressure relationship in carotid arteries from normotensive and spontaneously hypertensive rats," *J. Hypertens.* **10**, S27-S30 (1992).

34. W. C. P. M. Blondel, J. Didelon, G. Maurice, J. P. Carteaux, X, Wang, and J. F. Stoltz, "Investigation of 3-D mechanical properties of blood vessel using a new *in vitro* tests system: Results on sheep common carotid arteries," *IEEE Trans. Biomed. Eng.* **48**, 442-451 (2001).

35. K. Fronek, G. Schmid-Schoenbein, and Y. C. Fung, "A noncontact method for three-dimensional analysis of vascular elasticity *in vivo* and *in vitro*," *J. Appl. Physiol.* **40**, 634-737 (1976).

36. D. A. Vorp and J. P. Vande Geest, "Biomechanical determination of abdomonal aortic aneurysm rupture," *Arterioscler. Thromb. Vasc. Biol.* **25**, 1558-1566 (2005).

37. T. Länne, B. Sonesson, D. Bergqvist, H. Bengtsson, D. Gustafsson, "Diameter and compliance in the male human abdominal aorta: Influence of age and aortic aneurysm," *Eur. J. Vasc. Surg.* **6**, 178-184 (1992).

38. ST. MacSweeney, G. Young, RM. Greenhalgh, JT. Powell, "Mechanical properties of the aneurysmal aorta," *Br. J. Surg.* **79**, 1281-1284 (1992).

39. Da. Vorp, WA. Mandarino, MW. Webster, J 3rd. Gorcsan, "Potential influence of intraluminal thrombus on abdominal aortic aneurysm as Assessed by a New Non-invasive method," *Cardiovasc. Surg.* **4**, 732-739 (1996).

40. K. V. Ramnarine, T. Hartshorne, Y. Sensier, M. Naylor, J. Walker, A. R. Naylor, R. B. Panerail, and D. H. Evans, "Tissue doppler imaging of carotid plaque wall motion: A pilot study," *Cardiovascular Ultrasound* **I:17,** (2003).

41. A. Ishimaru, "Diffusion of light in turbid material," *Appl. Opt.* **28**, 2210-2215 (1989).

42. Brian C. Wilson and Steven L. Jacques, "Optical reflectance and transmittance of tissues: principles and application," *IEEE J. Quan. Elec.* **26**, 2186-2199 (1990).

43. B. C. Wilson and M. S. Patterson, "The physics of photodynamic therapy," *Phys. Med. Bio.* **31**, 327-360 (1986).

44. S. t. Flock, B. C. Wilson, and M. S. Paterson, "Total attenuation coefficient and scattering phase functions of tissues and phantom materials at 633nm," *Med. Phys.* **14**, 45-50 (1987).

45. R. Marchesini, A. Bertoni, S. Andreola, E. Milloni, and A. E. Sichirollo, "Extinction and absorption coefficients and scattering phase functions of human tissue *in vitro*," *Appl. Opt.* **28**, 2318-2324 (1989).

46. P. Parsa, S. L. Jacques, and N. S. Nishika, "Optical properties of rat liver between 350 and 2200nm," *Appl. Opt.* **28**, 2325-2330 (1989).

47. S. L. Jacques, C. A. Alter, and S. A. Prahl, "Angular dependence of HeNe laser light scattering by human dermis," *Laser Life Sci.* **1**, 309-333 (1987).

48. H. C. van de Hulst, *Multiple Light Scattering Tables, Formulas and Applications*, New York: Academic, (1980).

49. B. C. Wilson, W. P. Jeeves, and D. M. Lowe, "*In vivo* and postmortem measurements of the attenuation spectra of light in mammalian tissues," *Photchem. Photobiol.* **42**, 153-162 (1985).

50. F. P. Bolin, L. E. Preuss, and B. W. Cain, "A comparison of spectral transmittance for several mammalian tissues: Effects at PRT frequencies," in *Porphyrin Localization and Treatment of Tumors,* New York: Liss, 211-225 (1984).

51. A. Ishimaru, "Diffusion of light in turbid material," *Appl. Opt.* **28**, 2210-2215 (1989).

52. J. Lekner and M. C. Dorf, "Why some things are darker when wet," *Appl. Opt.* **27**, 1278-1280 (1988).

53. J. B. Dawson, D. J. Barker, D. J. Ellis, E. Grassman, J. A. Cotterill, G. W. Fisher, and J. W. Feather, "A theoretical and experimental study of light absorption and scattering by in vivo skin," *Phys. Med. Biol.* **25**, 695-709 (1980).

54. H. Zeng, C. MacAulay, B. Palcic, and D. I. McLean, "A computerized autofluorescence and diffuse reflectance spectro-analyser system for *in vivo* skin studies", *Phys. Med. Biol.* **38**, 231-240 (1993).

55. N. Guzelsu, J. F. Federici, H. C. Lim, H. R. Chauhdry, A. B. Ritter, and T. Findley, "Measurement of skin stretch via light reflection," *J. Biomed. Opt.* **8**, 81-86 (2003).

56. P. L. Williams and R. Warwick, eds., *Gray's Anatomy*, 36th ed. (Saunders Philidelphia, Pa., 1980), pp. 1216-1226.

57. J. Ferguson and J. C. Barbenel, "Skin surface patterns and the directional mechanical properties of the Dermis," in *Bioengineering and the Skin*, R. Marks and P. A. Payne, eds. (MTP, Lancaster, Pa., 1981), pp.83-92.

58. M. Assoul, M. Zahidi, P. Corcuff, and J. Mignot, "Three-dimensional measurements of skin surface topography by triangulation with a new laser profilometer," *J. Med. Eng. Technol.* **18**, 11-21 (1994).

59. B. Schulkin, H. C. Lim, N. Guzelsu, G. Jannuzzi, and J. F. Federici, "Polarized light reflection from strained sinusoidal surfaces," *Appl. Opt.* **42**, 5198-5208 (2003).

60. K. O. Hill, Y. Tremblay, and B. S. Kawasaki, "Model noise in multimode fiber links: theory and experiment," *Opt. Lett.* **5**, 270-272 (1980).

61. A. R. Michelson and A. Weierholt, "Modal noise-limited signal-to-noise ratios in multimode fibers," *Appl. Opt.* **22,** 3084-3089 (1983).

62. T. H. Wood, "Actual modal power distributions in multimode optical fibers and their effect on modal noise," *Opt. Lett.* **9,** 102-104 (1984).

63. R. J. S. Batess, D. M. Kuchta and K. Jackson, "Improved multimode fiber link BER calculations due to modal noise and non-self-pulsating lasers," *Optical and Quantum Electronics* **27**, 203-224 (1995).

64. P. G. Agache, C. Monneur, J. L. Leveque, and J. De Rigal, "Mechanical properties and Young's modulus of human skin *in vivo*," *Arch. Dermatol. Res.* **269**, 221-232 (1980).

65. É. É. Tseders and B. A. Purinya, "The mechanical properties of human blood vessels relative to their location," *Mechanics of Composite Materials* **11**, 271-275 (1975).

66. Doctor's Guide, "Size, location best predictors of future rupture for brain aneurysms," *http://www.pslgroup.com/dg/d05a6.htm* (accessed April 18, 2007).